REMODELING OF THE OPTIC NERVE DURING METAMORPHOSIS IN *XENOPUS LAEVIS*

by
Elizabeth Mills

A dissertation submitted to Johns Hopkins University in conformity with the requirements for the degree of Doctor of Philosophy

Baltimore, Maryland
March 2015

Abstract

The optic nerve of the amphibian *Xenopus laevis* shortens in length by approximately one-half during its metamorphosis from tadpole to frog. This dramatic shortening event takes place over the course of only a few days at metamorphic climax, when levels of thyroid hormone, the master transcriptional regulator of amphibian metamorphosis, peaks. The shortening of the optic nerve is associated with the remodeling of the retinal ganglion cell axons which make up the nerve. My thesis work focused on how the myelinated axons remodel during optic nerve shortening using primarily electron microscopy based quantitative analyses and reconstructions. Through cell type specific transgenic overexpression of a dominant negative thyroid hormone receptor α construct, the remodeling process was found to involve the distinct but coordinated activities of retinal ganglion cells, oligodendrocytes and astrocytes. Myelin remodeling, in contrast to demyelination, does not involve an immune response. Myelin segments decrease in length proportionally with the optic nerve itself and this shortening involves the production of focal myelin-axon detachments and myelin protrusions from otherwise intact myelin segments. Astrocyte processes selectively remove these local myelin dystrophies from the remodeling segments. This process uses known phagocytic machinery, including the opsonin Mfge8 and the downstream effector involved in cytoskeletal rearrangement, Rac1, as determined by transgenic overexpression of dominant negative constructs in astrocytes. By the end of shortening, one quarter of all myelin in the optic nerve is associated with astrocytes. However, the astrocytes are able to efficiently clear the myelin they internalize within approximately one month after the completion of metamorphosis. These results provide evidence for a new role for astrocytes in the developmental remodeling of myelin segments.

Advisor: Nicholas Marsh-Armstrong, Ph.D.

Acknowledgements

Foremost, I thank my advisor, Dr. Nicholas Marsh-Armstrong for his boundless patience, guidance, support, advice, and enthusiasm for science. He has been an amazing role model as a scientist and as a person. I am extremely grateful for having had the opportunity to experience his mentorship.

I thank my thesis committee members, Dr. Dwight Bergles, Dr. Samer Hattar, and Dr. Mollie Meffert for their insight and guidance.

I thank all the members of the Marsh-Armstrong lab for their help and camaraderie, especially Shannon Emmel for spectacular frog care and Chung-ha Davis for his help with electron microscopy and enthusiasm for science.

I also thank my family and friends for their love and support.

Finally, I thank all of the frogs and tadpoles involved in this study.

Table of Contents

List of Figures

Chapter 1: Introduction

Metamorphosis is the developmental period during which an animal transitions from a larval to an adult body plan. Many animals undergo a metamorphic transition during development, although these transitions are more commonly found in invertebrates. Within vertebrates, metamorphosis occurs in amphibians and teleost fish, a classification which includes approximately half of the living species of vertebrates on Earth (Paris and Laudet, 2008). This transition typically has both ecological and morphological components, such as the change from aquatic filter feeding herbivorous larval tadpoles to terrestrial carnivorous adult frogs. These changes in the ecological niche of the animal can only occur following the appropriate physiological transformations of the respiratory and digestive systems (Burggren and West, 1982; Ishizuya-Oka et al., 1996). The degree of morphological change varies widely by species, anuran frogs, such as *Xenopus laevis*, undergo some of the most radical physical transformations of any metamorphic species. Furthermore, unlike the metamorphic transitions of invertebrates, such as insects, which also undergo extensive physical changes, the larval tadpoles do not experience a period of dormancy, but rather remain active throughout the transition (Gilbert et al., 1996).

Role of thyroid hormone in metamorphosis

In vertebrates, the period of metamorphosis is defined and controlled by thyroid hormones (Etkin, 1963). Thyroid hormones are produced in the thyroid gland and involves the iodination of the amino acid tyrosine (Boron, 2003). The major form of thyroid hormone secreted from the thyroid gland into the bloodstream is thyroxin, which is the compound formed by the coupling of two di-iodotyrosine molecules, 3, 5, 3', 5'-tetraiodothyronine (T4). Although metamorphosis is characterized by a surge in circulating levels of thyroid hormone, thyroxin is not the potent activator of metamorphic changes. Instead, metamorphosis is primarily driven by 3, 5, 3'- triiodothyroacetic acid (T3), which is produced by the removal of the 5' iodotyrosine

molecule from T4 by the type II deiodinase (D2) (Huang et al., 2001). The dependence of metamorphosis in *X. laevis* on thyroid hormone has been demonstrated through the precocious induction of metamorphic changes in pre-metamorphic tadpoles following exposure to exogenous T3 (Tata, 1968).

The biological activity of T3 comes primarily through its effect on gene expression as a nuclear transcription factor through association with thyroid hormone receptors (Lazar, 1993). There are two major types of thyroid hormone receptors, classified as alpha and beta. The alpha receptor is generally constitutively expressed in *X. laevis* and is present early in development, before thyroid hormone, likely derived from maternal mRNA, although, unlike in mammals, it does not appear to play a critical role in early embryogenesis (Kawahara et al., 1991). The expression of the receptor does increase throughout development and may allow the tadpoles to initiate different response programs as the levels of thyroid hormone increase throughout the pre-metamorphic period, such that the animals undergo a stereotyped developmental program that is synchronized with thyroid hormone levels. The beta receptor, on the other hand, is found at much lower levels than the alpha receptor, is primarily localized to head region, and is regulated by the alpha receptor such that it is potently induced by thyroid hormone (Machuca et al., 1995). Both types of receptors, however, are induced by thyroid hormone such that increased levels of thyroid hormone elevate the production of the receptors which mediate the activity of the hormone. Elevations in the titer of thyroid hormone in *X. laevis* lead to a two fold increase in levels of thyroid hormone receptor alpha and a twenty fold increase in levels of the beta receptor during metamorphosis (Yaoita et al., 1990).

Thyroid hormone mechanism of action

The receptor is a nuclear hormone transcription factor which binds to DNA at thyroid or T3 response elements (TREs) in the promoter regions of genes. The receptors can bind to the TREs in their monomeric form, but it is a very low affinity interaction (Kliewer et al., 1992; Leid

et al., 1992). The thyroid hormone receptors are typically found as heterodimers complexed with retinoid X receptors which increases the stability of the interaction with the DNA, and in the absence of thyroid hormone these complexes act to repress gene transcription since in the unbound state the complex associates with co-repressors (Fondell et al., 1993; Hörlein et al., 1995). In genes that are negatively regulated by thyroid hormone the binding of un-liganded thyroid hormone receptor homodimers to the TRE facilitates transcription, whereas the presence of the hormone leads to repression, and may involve the recruitment of histone modifying complexes (Fondell et al., 1993; Piedrafita et al., 1995). Following the direct import of T3 or conversion from T4 to T3 in the cytoplasm, T3 diffuses or is transported into the nucleus where it binds to receptor complexes bound the TREs in order to influence gene expression (Halpern and Hinkle, 1982). The binding of T3 leads to a conformational change in the thyroid hormone receptor which results in the release of the co-repressor molecules (Bendik and Pfahl, 1995). One of the genes regulated by thyroid hormone is the type III deiodinase (D3) which removes the 5 iodotyrosine molecule from T3 to create the inactive metabolite 3, 3'-diiodothyronine (T2), thereby completing the regulatory feedback loop (Wang and Brown, 1993).

Thyroid hormone can also mediate cellular activity through non-genomic actions. These actions are thought to be mediated through various signaling cascades at the plasma membrane or in the cytoplasm, including free calcium, cyclic-AMP, and protein kinase signaling (Davis et al., 2008). These cascades are generally important for influencing cell proliferation and motility. Activation of cell surface integrin receptors, particularly αVβ3, can initiate protein kinase signaling cascades which can regulate the activity of various plasma membrane transporters, such as the Na/H exchanger and Na, K ATPase (Cheng et al., 2010). As a result of this role in modulating ion currents, these non-genomic actions appear to be most relevant in areas dependent on ionic conductions, such as the heart and nervous system (Davis and Davis, 2002; Leonard, 2008). Furthermore, thyroid hormone mediated integrin activity can enhance the genomic actions of thyroid hormone by promoting the translocation of thyroid hormone receptors into the nucleus

(Cao et al., 2009). Although these non-genomic actions have important physiological effects on an organism, they are unlikely to be able to induce the sweeping changes seen during amphibian metamorphosis. Indeed, work utilizing transgenic overexpression of dominant negative receptors revealed that interference with the genomic action of thyroid hormone, through its receptor can prevent both spontaneous and T3 induced metamorphosis in *X. laevis* (Buchholz et al., 2004). Therefore, amphibian metamorphosis is primarily driven by changes in gene expression mediated by the transcriptional regulation of TRE containing genes via the thyroid hormone bound receptor complex.

Nervous system remodeling during *X. laevis* metamorphosis

During metamorphosis, morphological changes affect every major organ system in *X. laevis*, including the nervous system, which must rewire in order for the animal to properly control its altered body (Gilbert, 2000). The animal must innervate its newly formed structures, such as the limbs, while de-innervating larval features. Since the metamorphic tadpoles remain active throughout this period, it is critical that the nervous system rewires appropriately, as a loss of mobility would make them vulnerable to predation. Additionally, the metamorphic animal needs to modify existing connections.

One of the most dramatic remodeling events in *X. laevis* involves the change in the shape of the head from wide and round in the larval tadpole to narrow and triangular in the post-metamorphic frog. This morphological change in head shape is associated with the modification of several cranial nerves, most notably the olfactory and optic nerves (cranial nerves I and II) which emerge from the forebrain, rather than the brainstem (Wiechmann and Wirsig-Wiechmann, 2003). Since these nerves are attached to organs located along the peripheral boundary of the head, with the olfactory nerve connecting the olfactory organ, which consists of the principle cavity epithelium and the rostral vomeronasal organ, to the olfactory bulb and the optic nerve connecting the laterally oriented eyes to the optic tectum in the brain, changes in the size and

shape of the head have profound effects on the length of these nerves (Burd, 1991; Cullen and Webster, 1979). Throughout the early part of development, as the head, along with the rest of the animal grows in size, these nerves grow longer to accommodate the increasing distance between the outer boundary of the head and the brain. The growth occurs slowly over the period of several weeks until the head reaches maximal size at the developmental stage described by Nieuwkoop and Faber (Nieuwkoop and Faber, 1956) (NF) Stage 60. In contrast, the metamorphic remodeling of the head occurs extremely rapidly over the course of several days between NF Stages 60 and 66. As a result, both the olfactory and optic nerves shorten dramatically over this period (Burd, 1991; Cullen and Webster, 1979). Although the decrease in length experienced by the olfactory nerve is the most severe, it is designed to cope with turnover and the generation of cellular debris (Higgs and Burd, 2001). The olfactory system undergoes continuous turnover of olfactory receptor neurons and in mammals it has been shown that the glial cells of the olfactory nerve, olfactory ensheathing cells, can engulf apoptotic neurons (Su et al., 2013), and thus it is likely that they serve a similar function with debris generated by shortening axons during metamorphosis.

The optic nerve also dramatically shortens to over one-half its length during metamorphic climax (Cullen and Webster, 1979), however, it does not undergo continuous turnover and approximately ten percent of its axons are ensheathed in myelin (Gaze and Peters, 1961). The optic nerve is comprised of the axons of retinal ganglion cells (RGCs) whose cell bodies are located in the retina of the eye. The axons exit the eye at the optic disk and course along the length of the optic nerve until they ultimately terminate in the brain, primarily in the thalamus and optic tectum (Hoskins and Grobstein, 1985; Wiechmann and Wirsig-Wiechmann, 2003). The optic nerve also contains two major classes of glial cells, astrocytes and oligodendrocytes (Cima and Grant, 1982b). In *Xenopus*, the RGC axons are unmyelinated in the eye and a small subset become myelinated shortly after exiting the optic disk.

Myelin structure and composition in *X. laevis*

Myelin exists in the form of regularly spaced segments, which enable fast and efficient transfer of information over long distances though the salutatory propagation of action potentials from one Node of Ranvier to the next (Huxley and Stampfli, 1949). The myelin segments themselves are lipid (70% by weight), particularly cholesterol (approximately 27%), rich cellular processes, produced by Schwann cells, in the peripheral nervous system, or oligodendrocytes, in the central nervous system, with highly specialized architecture that enables them to form the compact membranous wraps around axons that are key to their insulating function (Quarles et al., 2006). Although all myelin membranes are lipid rich, the exact composition of the membranes can vary by species and developmental stage (Cuzner et al., 1965; Horrocks, 1968). For example, in mammals, juveniles have a lower percentage of proteins in their myelin as well as a higher ratio of phospholipids to galactolipids than their adult counterparts (Morell et al., 1972; Svennerholm and Vanier, 1978). The myelin associated proteins and galactolipids are important for the stabilization of axo-glial interactions required for the proper formation of the Nodes of Ranvier and the maintenance of mature myelin (Dupree et al., 1998; Marcus et al., 2002). One notable aspect of species specificity is that *X. laevis* has much a higher percentage of monogalactyl diglyceride in their myelin, which is important for myelination and oligodendrocyte process formation, than mammals (Trapp et al., 1980). It may be some of these characteristic differences in *Xenopus* myelin which facilitate the vast transformations of its nervous system during metamorphosis. Although most of the differences in myelin composition between species do not follow a clear evolutionary trajectory (Kirschner et al., 1989), they may be relevant to differences in the plasticity of the nervous system between juvenile and aged animals and across taxa.

Mechanisms involved in axon myelination

Myelinating oligodendrocytes are produced by the differentiation of oligodendrocyte precursor cells (OPCs), which can be identified by the expression of the chondroitin sulfate NG2 and the platelet derived epidermal growth factor α receptor (PDGFRα) (Dawson et al., 2003; Hall et al., 1996). The presence of OPCs in the central region of the optic nerve of *X. laevis* can first be detected around NF Stage 48 (Cima and Grant, 1982b). Mature oligodendrocytes and the first myelin segments are found on axons in the center of the nerve at Stage 48/49. Myelination then proceeds in both directions along the axons over the course of development. In mammals, the differentiation of OPCs occurs in response to various signaling molecules, including thyroid hormone through the alpha receptors, and decreases in Wnt/β-catenin signaling cascades (Emery, 2010). OPCs also receive synaptic input from axons, and the differentiation of OPCs may be modulated by the postsynaptic response of axonal neurotransmitter release, such as the activation of glutamatergic NMDA receptors (Li et al., 2013). Mature oligodendrocytes lose these synaptic connections and express myelin associated genes such as myelin basic protein (Mbp) and proteolipid protein (Plp) (Baumann and Pham-Dinh, 2001; Kukley et al., 2010). The expression of these genes in mammals is also induced by thyroid hormone (Barradas et al., 2001; Farsetti et al., 1991).

The decision by an oligodendrocyte to produce a myelin segment along a particular axon involves the integration of a variety of signals derived from axons, largely in the form of adhesive signaling molecules such as neural cell adhesion molecule, neuregulin, contactin, and laminin, or activity derived signals like glutamate (Lundgaard et al., 2013; Piaton et al., 2010). The signaling responses are mediated through ErbB, integrin, and NMDA receptors on oligodendrocytes. Astrocytes can also promote myelination in response to ATP derived from electrical activity in axons. P2 purinergic receptor activation on astrocytes leads to the release of the pro-myelination cytokine leukemia inhibitory factor (Ishibashi et al., 2006). Juvenile myelin, including that found in *X. laevis* tadpoles is also enriched in the enzyme 2',3'-cyclic nucleotide 3'-phosphodiesterase (Trapp et al., 1980), which is important for oligodendrocyte process initiation, and thus is found

at highest levels during periods of active myelination (Lee et al., 2005). These diverse signals are integrated by the oligodendrocyte largely through the signaling cascades of the non-receptor tyrosine kinase, Fyn, and translated into changes in the cytoskeleton of oligodendrocyte processes as well as the synthesis and trafficking of myelin proteins (Kramer-Albers and White, 2011). Additionally, myelination is largely dependent on axon size, as the axons must exceed a particular diameter for the oligodendrocyte derived myelin membranes to initiate wrapping of the axon (Matthews, 1968).

The myelin membranes form concentric wraps around the axon. This occurs by the consecutive wrapping of the inner tongue of the oligodendrocyte myelin sheath layer. The inner tongue serves as the myelin growth zone where vesicles containing the newly synthesized components for the myelin membrane are trafficked via cytoplasmic channels (Snaidero et al., 2014). The extent of the network of these myelinic cytoplasmic channels is correlated with the myelination potential of the oligodendrocytes, such that these channels are most prevalent during periods of peak myelination and are primarily closed following the maturation of the organism. Adhesion between the wraps of myelin is largely mediated by myelin proteins, such as Mbp and Plp (Boison et al., 1995; Min et al., 2009). The compaction of the myelin is also dependent on lipid composition of the membrane, and is reflected in developmental changes in myelin as the nervous system matures (Coetzee et al., 1999; Saher et al., 2011). Additionally, the compaction is further orchestrated by electrostatic interactions between the lipid bilayers that are facilitated by the down regulation of the glycocalyx, whose abundance of negatively charged polysaccharides usually fosters membrane repulsion (Bakhti et al., 2013).

Interactions between axon and myelin membranes

Adhesive complexes also exist between the axonal plasma membrane and the innermost myelin membrane. Since a myelin sheath along an axon is composed of individual segments separated by unmyelinated regions (the Nodes of Ranvier), each segment must be tethered to a particular location of the axon. The myelin segment can be divided into three major regions, the

paranodes, which are the boundary regions of the segment, the juxtaparanodes, which are immediately adjacent to the paranodes, and the internodal region which makes up the majority of the segment (Zoupi et al., 2011). Although some adhesion between the axon and myelin membranes occurs in the internodal region, such as through myelin-associated glycoprotein (MAG) (Trapp et al., 1989), most of the adhesive complexes are localized to the juxtaparanodal and paranodal regions. The paranodal adhesive interactions are the strongest and are mediated by the interaction between contactin and contactin-associated-protein on axons and the Neurofascin 155kDa isoform on oligodendrocyte derived membranes (Nave, 2010). Since these adhesive complexes are important for stabilizing the myelin segments to the axon, the clustering of these components is also developmentally regulated by changes in myelin composition, particularly galactolipids (Dupree et al., 1998). In this way, adhesion between myelin and axons is weaker during early development, and likely provides for enhanced plasticity in the growing animal.

Mechanisms of myelin segment growth and plasticity

The ability to maintain efficient conduction over long distances in the nervous system requires the proper amount of myelin on an axon. Optimal conduction is achieved through the correct ratio of myelin to axon size, and this ratio can vary across species and regions of the nervous system based on the environment and function of the signal carried by a particular set of axons (Baumann and Pham-Dinh, 2001). In terms of myelin, the two major parameters that influence the speed of conduction are the length and thickness of the myelin segment. In general, larger caliber axons require thicker myelin sheaths and are associated with longer internodal distances, which enable the fastest conduction (Waxman, 1980). The proper width and length of myelin segments is likely established at least in part during the myelination process. Observational electron microscopy studies have reported that the initial establishment of myelin segments in the peripheral nervous system is itself a dynamic process, involving the elongation, shortening, and/or removal of individual segments. *In vivo* imaging in zebrafish has confirmed

that the initiation of myelination in the central nervous system is similarly dynamic (Liu et al., 2013).

Once established, the myelin segments must remain sufficiently plastic to accommodate developmental axonal growth. Developmental increases in axon diameter are coupled to the addition of membrane wraps to myelin segments ensheathing axons, thereby maintaining the near linear relationship between axon caliber and myelin thickness necessary for optimal conduction (Berthold et al., 1983; Friede and Miyagishi, 1972). In the peripheral nervous system, the length of segments has also been shown to be regulated, as Schwann cell derived myelin segments elongate in proportion to developmental increases in nerve length, increasing internodal distances by as much as a factor of four (Sherman and Brophy, 2005). The Schwann cell segments elongate in a cell autonomous manner due to passive stretching which requires the microtubule based transport of myelin protein components toward the growing ends of the segment, similar to the transport of myelin components along cytoplasmic channels during initial myelination (Court et al., 2004). Since each Schwann cell typically produces a single myelin segment, it can readily respond to growth related axon cues. In contrast, it is more complicated to tailor myelin to axon size in the central nervous system, since an individual oligodendrocyte can produce up to 40 myelin segments on axons of different calibers (Almeida et al., 2011). Although oligodendrocyte segments must also accommodate growth, the mechanisms governing these processes are less well understood.

Furthermore, myelin segments in the central nervous system have been shown to be modifiable in a learning or activity dependent manner, which may underlie some of the restructuring of connections in the brain upon the acquisition of a new skill (Fields, 2008; McKenzie et al., 2014). Imaging studies have revealed changes in white matter regions associated with learning a particular motor skill, which is likely due to learning related new myelination or increases in the thickness of existing myelin segments (Sampaio-Baptista et al., 2013). These changes in myelination likely alter conduction speeds and thereby affect the signaling dynamics

of selective neural circuits. De novo myelination in the mature nervous system of rodents appears to involve the differentiation of OPCs into new myelinating oligodendrocytes, rather than an increase in process initiation by existing cells (Young et al., 2013). However, it was recently shown that new myelination in the adult nervous system of humans involves an increase in myelin production by pre-existing oligodendrocytes (Yeung et al., 2014), suggesting that there may be a variety of mechanisms involved in myelin plasticity, and their relevance may be species and context dependent. Meanwhile, increases in myelin thickness are mediated largely by extracellular-related-kinase mediated signaling in oligodendrocytes (Ishii et al., 2012). Interestingly, another form of learning related plasticity may involve the selective removal of myelin segments. High resolution electron microscopy has allowed for the 3-dimensional reconstruction of axons from various regions in the mouse cerebral cortex and found widespread evidence for intermittent myelination of axons, in which axons had long unmyelinated stretches which contained both afferent and efferent synapses (Tomassy et al., 2014). Since the presence of myelin prevents the formation of these synapses, the selective addition or removal of segments could influence the location of these synapses, and thus affect intracellular signaling or conduction along the axon.

Importance of proper myelination

Disruption of any of the processes involved in regulating myelin composition, initiation, plasticity or maintenance will interfere with signal processing in the nervous system. Sustained hypo-myelination or hyper-myelination of axons can lead to the onset of neuropathy and other pathologies. The interplay between pro-myelin phosphatidylinositol 3,4,5-triphosphate (PIP3) and myelin inhibiting phosphatase and tensin homolog (Pten) regulates the level of myelin production (Goebbels et al., 2010). Although PIP3 can be used to reopen the cytoplasmic channels necessary for active myelination by oligodendrocytes (Snaidero et al., 2014), if it is not properly balanced with the correct level of Pten signaling, then axons will become hyper-

myelinated (Goebbels et al., 2010). Interestingly, small hyper-myelinations are present on newly myelinated axons during development, which may be due to a bias in pro-myelin signaling during this period (Snaidero et al., 2014). These hyper-myelinations, however, are resolved as the animal matures. Chronic hyper-myelination of axons, on the other hand, is often associated with the formation of myelin whorls, redundant loops, and tomaculas (Adlkofer et al., 1995; Sander et al., 2000). These myelin dystrophies can interfere with conduction by affecting the structural integrity of the myelin insulation. Hypo-myelination or dysmyelination can occur due to improper myelination during development (Di Rocco et al., 2004), or as a result of injury or disease related demyelination.

Demyelination, or the loss of myelin on axons, can occur due to problems in myelin structure, such as a genetic lack of adequate adhesive complexes or environmental toxins which disrupt membrane composition, or through autoimmune disorders in which healthy myelin is attacked and removed (Popescu and Lucchinetti, 2012). Demyelination is more common in the adult animal (Bartzokis et al., 2010; Newbould et al., 2014). During early development myelin membranes are likely more plastic since they are loosely associated with axons and one another in order to accommodate growth and can be more easily replaced by the large pool of newly differentiating oligodendrocytes. As the system matures, however, any disruptions to the integrity of the myelin or the axo-glial interactions can lead to the loss of the myelin segment (Carenini et al., 1996; Filbin et al., 1999; Marcus et al., 2002). The loss of myelin is not only detrimental to the axon which has lost its insulation and trophic support, but also to the health of the entire surrounding area as well.

Clearance of myelin from the nervous system

The presence of myelin debris prevents the onset of repair, such that in the context of injury or disease, the damage can continue in an unmitigated manner until the debris is cleared (Neumann et al., 2009). Inhibitory molecules in the myelin debris such as Nogo and

oligodendrocyte myelin glycoprotein prevent regenerative axon outgrowth and block the differentiation of OPCs into mature oligodendrocytes, thus inhibiting re-myelination (Filbin, 2003). As an extremely lipid rich structure, myelin is difficult for cells to breakdown and will persist at the site of damage unless contacted by a phagocytic cell capable of myelin internalization. The myelin debris is usually cleared by immune system derived professional phagocytic cells, namely macrophages and microglia (Griffin et al., 1992). Microglia are recruited to the site of myelin damage in response to the chemokine CXCL10, which is released by local astrocytes in response to myelin damage, through the chemokine receptor CXCR3 (Rappert et al., 2004; Skripuletz et al., 2013). These phagocytes not only remove the inhibitory myelin debris, but also release a variety of immuno-inflammatory cytokines. Although some of these cytokines may stimulate repair mechanisms by promoting OPC differentiation or neuronal growth and survival, other molecules can have cytotoxic effects and disrupt synaptic function (Stoll et al., 2000). Phagocytosis of myelin by microglia is primarily mediated through the complement-receptor-3, which also appears to have a role in regulating the level of myelin a cell will internalize (Rotshenker, 2003). Although it facilitates the internalization of myelin, activation of the receptor also down-regulates further intake of myelin through the activation of the tyrosine kinase, Syk, which ultimately controls the ability of the actin cytoskeleton to mediate process formation necessary for the phagocytic activities of the cell (Gitik et al., 2011; Hadas et al., 2012). Therefore, these phagocytes have a limit to the amount of myelin debris they will internalize, likely to avoid metabolically overloading the cell. Thus, the clearance of a large area of myelin debris would require a massive infiltration of monocytes.

Role of phagocytosis in nervous system development

Although myelin is always a difficult substance for cells to metabolize, the clearance rate, and thus regeneration rate in the context of injury, is greatly enhanced in juveniles (Kang and Lichtman, 2013) and in a subset of vertebrates, including *X. laevis* (Tanaka and Ferretti, 2009)

Large scale clearance of cellular debris is a major part of nervous system development in general. Apoptotic, or programmed cell death is an integral part of the developing nervous system, and occurs largely through early overproduction of neurons and glial cells in the context of limited trophic support (Oppenheim, 1991). Neurons that fail to innervate their target, and other cells initiating the programmed cell death pathway will begin to activate caspase-3 through cleavage, and be targeted for removal (Simon et al., 2012; Srinivasan et al., 1998). Phagocytes such as microglia, recognize these apoptotic cells through 'eat me' signals on the surface of the cell. The best characterized of these signals is the exposure of phosphatidylserine by the flipping of the phospholipid from the inner to the outer leaflet of the plasma membrane (Fadok et al., 1998). The exposed phosphatidylserine can be recognized directly or indirectly through the association with an opsonin by a variety of phagocytic receptors including the receptor tyrosine kinase MER (Mertk), phosphatidylserine receptor, and integrin receptors (namely $\alpha_V\beta_3$ and $\alpha_V\beta_5$) (Ravichandran, 2010). Apoptotic clearance can also be mediated through a set of cell death related genes originally described in *Caenorhabditis elegans* as the cell death abnormal (ced) genes, with cell corpse recognition occurring through the ced-1 receptor (Zhou et al., 2001). Axon and synaptic pruning, or the modification of existing connections are also important features of nervous system development which rely on the phagocytosis of cellular components (Bishop et al., 2004; Corty and Freeman, 2013; Stevens et al., 2007). It is the rapid and regulated clearance of cellular and axonal debris from the developing nervous system that facilitates the system to wire properly and not experience any lasting pathology.

A key aspect of phagocytosis mediated developmental nervous system remodeling is that unlike in mature animals, it does not rely primarily on the infiltration of professional phagocytes, such as macrophages and microglia. Instead, phagocytosis is mediated by local macroglial populations, most notably astrocytes (Mallat et al., 2005). Astrocytes, like oligodendrocytes, have generally been regarded as supportive cells in the central nervous system. However, these supportive roles are vital to the health and activity of neurons, and thus underlie key aspects of

the establishment, maintenance and modification of neuronal circuitry and communication. Just as conduction velocities and axon viability are compromised by the loss of insulation, signaling and trophic support provided by myelinating oligodendrocytes, the loss of astrocytic activities would severely diminish the capacity of the nervous system to function. Indeed, astrocytes are also important for maintaining the integrity of myelinated axons, as evidenced by the demyelinating pathology associated with Alexander's disease, which is caused by a genetic mutation in glial fibrillary acidic protein (GFAP), which encodes for an integral cytoskeletal structural element in astrocytes (Brenner et al., 2001).

Among the many vital functions carried out by astrocytes are: the regulation of ionic concentrations, communication with the vasculature, clearance of metabolites, metabolic support to neurons, removal of glutamate and maintenance of glutamatergic transmission by neurons, as well as the formation and stability of synapses (Clarke and Barres, 2013; Kimelberg and Nedergaard, 2010). In these, and many other ways, the astrocytes locally modulate the environment of the nervous system, which ultimately affects the functioning of the surrounding neural circuitry. By controlling the formation sites of synapses, the availability of the glucose rich blood supply and thus energy, and the availability of glutamate as well as its persistence at synaptic and extrasynaptic sites, the astrocytes shape and modify the activity level of neurons and the strength of their connections. Consequently, it has been found that astrocytes are involved in the orchestration of gamma oscillations, which are patterned waves of activity that have been implicated in some forms of memory, which are disrupted in various neurological disorders, such as Alzheimer's disease (Lee et al., 2014). Furthermore, astrocyte dysfunction is a common feature of a wide variety of neurodegenerative diseases, and the progressive loss or disruption of astrocyte activities may contribute to aging related cognitive decline (García-Matas et al., 2008; Lima et al., 2014; Simpson et al., 2011).

Properties of Astrocytes

Astrocytes can also modify their properties in response to nervous system damage, and become reactive. These astrocytes are typically identified by their hypertrophic morphology and up-regulation of GFAP (Ridet et al., 1997). Similar to a microglial infiltration, the presence of these reactive astrocytes can be a double edged sword. Their release of neuro-inflammatory molecules and formation of a glial scar can inhibit regeneration, however, they also play vital roles in ensuring the survival of the surrounding tissue (Sofroniew, 2005). The removal of potentially excitotoxic neurotransmitter, excess ions and cellular debris help to restore balance to the extracellular environment, which in turn leads to the restoration of neural function. While chronic reactive gliosis is deleterious, the activity of reactive astrocytes in response to acute injury facilitates repair and improves recovery outcomes. Consequently, the incomplete removal of neurotoxic debris by reactive astrocytes is believed to contribute to the progression of various neurodegenerative disorders (Sokolowski and Mandell, 2011).

Although all astrocytes contribute to the health and maintenance of the nervous system, they are a diverse cell population, such that astrocytes in different regions exhibit different characteristics and sub-specialties (Oberheim et al., 2012). Differences in astrocytes also account for variation in cognition, plasticity and other key aspects of the nervous system throughout one's ontogeny as well as through phylogeny. For instance, the astrocytes of primates have been found to be more diverse, larger and complex (Oberheim et al., 2009) than other mammals, and the incorporation of human derived astrocytes in rodent brains leads to an enhancement of memory and overall cognitive function based on behavioral testing (Windrem et al., 2014).

Astrocytes and regeneration

Some classes of animals, most notably amphibians and fish have an extensive capacity for regeneration in the central nervous system following injury, such as optic nerve transection. Recent evidence suggests that differences in gene expression, signal secretion, intercellular interactions, and thus the way the astrocytes regulate the microenvironment following injury in

these animals account for a large part of their regenerative advantage (Garcia and Koke, 2009). Another key aspect may be the ability of the optic nerve astrocytes in these species to contribute to the rapid clearance of cellular debris, including myelin. Indeed, large amounts of axon and myelin debris have been visualized within optic nerve astrocytes in goldfish following nerve transection (Colavincenzo and Levine, 2000). Therefore, it is likely that these species with higher levels of plasticity maintain more developmentally immature astrocytes and/or can reactivate the genetic programs necessary for phagocytosis and neural remodeling. In support of this idea, astrocytes in the optic nerve of fish and amphibians do not express the mature astrocyte marker GFAP, but instead their cytoskeleton is comprised of cytokeratin 8 (Koke et al., 2010; Rungger-Brändle et al., 1989). Additionally, astrocytes in these animals express brain lipid binding protein (Blbp, which is encoded by the *fabp7* gene) which is usually associated with newly differentiated immature astrocytes (Ge et al., 2012). Blbp has also been found to be up-regulated in a subset of astrocytes after demyelinating injuries in mammals and is associated with higher rates of re-myelination and recovery (Kipp et al., 2011b; White et al., 2010). The Blbp expressing astrocytes appear to promote the differentiation of OPCs and other repair mechanisms similar to what is seen in fish and amphibians.

Phagocytic astrocytes in development

During development, young astrocytes tend to be in a more reactive-like state, without being immunogenic, and thus have a greater capacity to shape the developing nervous system through their phagocytic activity. The phagocytic activity of these young astrocytes has been shown to be important for shaping developing neural circuitry, through the elimination of selective synapses (Chung et al., 2013). Furthermore, this activity has been shown to involve the same molecular machinery generally associated with phagocytosis by microglia, namely the receptors Mertk, and the ced-1 homolog, Megf10. Indeed, transcriptional profiling of forebrain astrocytes has revealed the expression of the entire ced pathway and various other known

phagocytosis related genes in these cells (Cahoy et al., 2008). The high expression of phagocytic machinery by astrocytes then may underlie the ability of the developing nervous system to so efficiently clear debris and the plasticity to modify neural circuitry.

Metamorphosis is an accelerated period of development which involves large amounts of cell death and requires enhanced plasticity to remodel tissue. This is particularly relevant for the nervous system which loses and modifies existing neural circuits in order to accommodate new ones. Although metamorphosis is clearly a developmental event, it occurs during the larval period well after embryogenesis and neural patterning, when the nervous system has already begun to mature. The metamorphic modification of neural circuitry in the fruit fly, *Drosophila*, has been shown to involve glial cell mediated neuronal pruning. Ensheathing glial cells as well as astrocytes activate the phagocytic receptor, the *Drosophila* ced-1 homolog Draper, in response to the steroid hormone which mediates metamorphosis in insects, ecdysone (Awasaki et al., 2006; Tasdemir-Yilmaz and Freeman, 2014). Interestingly, the particular phagocytic receptor signaling pathway activated by the glial cells was dependent on whether an entire cell corpse or selected neurites on otherwise intact neurons were to be internalized (Tasdemir-Yilmaz and Freeman, 2014). Ecdysone was also critical for the recruitment and mobilization of these phagocytic glial cells to the sites of remodeling (Awasaki et al., 2006). Therefore, it appears that metamorphosis related signaling, at least in insects, can induce glia into a phagocytically active state reminiscent of those involved in the clearance of apoptotic cellular debris and axon pruning during early neural development.

Potential role of astrocytes in *X. laevis* metamorphosis

As part of the highly regulated process of amphibian metamorphosis, the metamorphic shortening and remodeling of the optic nerve in *X. laevis* may be similar to ecdysone mediated neurite pruning in *Drosophila*, in the involvement of highly phagocytic local astrocytes. Blbp is involved in lipid metabolism and homeostasis and its expression in astrocytes also appears to

support neural remodeling. Interestingly, expression of Blbp is regulated by another set of nuclear hormone receptors Rev-erbα and retinoic acid receptor (Schnell et al., 2014), whereas the expression of some other members of the fatty acid binding protein family is directly regulated by thyroid hormone (Nakagawa et al., 1994; Shi and Hayes, 1994). Furthermore, similar to thyroid hormone, expression of Blbp in astrocytes has been linked to the promotion of cellular migration (Kipp et al., 2011a), which is conducive to phagocytosis.

Previous electron microscopy based descriptions of optic nerve shortening in *X. laevis* have noted the presence of myelin derived debris inside cells (Cima and Grant, 1982b), which were presumed to be astrocytes based on the low numbers of microglia found in the nerve at this time (Goodbrand and Gaze, 1991). As more developmentally immature cells, these Blbp expressing astrocytes may have a greater capacity to efficiently internalize myelin. That astrocytes may contribute to the clearance of myelin is suggested by the finding that a subset of astrocytes in the mouse optic nerve head express genes typically associated with the phagocytosis of myelin (Nguyen et al., 2011). Furthermore, the characteristic myelin composition of *X. laevis*, and moreover that of metamorphic tadpole myelin, may make any myelin debris generated at this time more amenable phagocytic substrates. Therefore, I examined the process of metamorphic optic nerve shortening and the role of thyroid hormone with respect to the changes that take place in myelinated RGC axons. Furthermore, I investigated the potential presence and role of phagocytically active astrocytes in the remodeling of myelin segments on shortening axons during metamorphic climax.

Chapter 2: Characterization of the optic nerve during metamorphic remodeling in *X. laevis*

One of the most dramatic morphological remodeling events that occur during metamorphosis in the amphibian *Xenopus laevis* is the change in structure of the head to become smaller in size and more triangular in shape (Figure 2.1). A major aspect of this change is a shift to more rostro-dorsally positioned eyes to allow for the onset of binocular vision in the frog, relative to the laterally oriented eyes of the pre-metamorphic tadpole (Grant et al., 1980). In order to achieve this head remodeling, there must be concomitant remodeling and shortening of various cranial nerves, including the optic nerve.

In order to determine the consequence of shortening on the overall structure as well as the individual components of the optic nerve, I selected four stages of animals, as determined by Nieuwkoop and Faber (NF) staging criteria (Nieuwkoop and Faber, 1956), for analysis. I used animals at the NF Stages 58, 62, 66, and 4 weeks after completing metamorphosis. At Stage 58 the animals are pre-metamorphic tadpoles in which the head has not yet reached maximal size and is still round with laterally oriented eyes, at Stage 62 the animals are in mid-metamorphic climax in which the head is significantly smaller and the eyes are still relatively laterally positioned, at Stage 66 the animals have reached the immediate conclusion of metamorphosis in which the head has decreased to its smallest size and remodeling is complete (Figure 2.1), and at 4 weeks after metamorphosis the animals are juvenile frogs in an active growth phase. This set of animals allowed for the comparison of optic nerves at two active stages of remodeling (Stages 62 and 66) with those prior to the onset and well after the completion of metamorphic head and nerve remodeling. Analyses of the optic nerve were carried out using electron and light level microscopy in order to obtain structural and expression data, respectively.

The optic nerve structurally remodels but maintains cellular organization during metamorphosis

First, I confirmed that the optic nerves do shorten to approximately one-half their length during the period of metamorphic head remodeling (Cullen and Webster, 1979). I found that the length of the optic nerve decreased from 4.83 ± 0.54 mm at Stage 58 to 2.17 ± 0.20 mm at Stage 66 (Figure 2.2A). The length of the nerve did not significantly change during the next 4 weeks following metamorphosis, which likely reflects that relative to body size the head did not grow much during this time, and this measure may vary in different cohorts of animals depending on their growth rate. In addition to length, I also examined the cross-sectional area of the optic nerves during these stages. The area of the nerve showed an inverse relationship to the length such that the cross-sectional area doubled from 810 ± 560 μm^2 at Stage 58 to 1,890 ± 195 μm^2 at Stage 66 (Figure 2.2B). This widening represented a transient hypertrophy specific to the period of metamorphic remodeling. This hypertrophy is resolved within one month, as the nerve area decreased to 1,250 ± 250 μm^2 in the juvenile frogs. Therefore, shortening leads to net loss of optic nerve volume.

To determine whether the overall composition of the nerve is affected by metamorphic remodeling, immunolabeling of cross-sectional cryo-sections of optic nerve was performed using markers for the major components of the nerve: axons, myelin and astrocytes. The retinal ganglion cell (RGC) axons were labeled by the pan-axonal marker acetylated alpha tubulin, myelin was labeled by myelin basic protein (Mbp), and astrocytes were labeled by brain lipid binding protein (Blbp) (Figure 2.2C). The conserved pattern of immunolabeling across all examined stages, with myelinated axons preferentially localized to the nerve core and astrocytes extending radially oriented processes toward the pial surface, indicates that there is no major reorganization of the individual cellular components. However, the transient hypertrophy of the nerve during shortening suggested a possible alteration of the sub-structure. I was particularly interested in exploring the relationship between axons and their associated myelin sheaths as the optic nerve shortens. The response of myelin segments to axon shortening in the developing nervous system has not been previously described. This type of analysis requires an examination

of myelinated axons at the ultrastructural level. Since light level microscopy cannot provide sufficient resolution to observe the detailed structure of the individual nerve components, I turned to electron microcopy.

Electron microscopy based quantification of optic nerve myelin

Transmission electron microscopy (TEM) was carried out in collaboration with Chung-ha Davis. Animals were ordered from a commercial supplier (Xenopus Express) and six wild-type *X. laevis* were used for each of the specified stages (NF Stage 58, 62, 66, and 4 weeks post-metamorphic). The optic nerves were dissected from the animals and processed for TEM using the protocol for Serial Block-face Scanning Electron Microscopy (SBEM) developed at the National Center for Microscopy and Imaging Research (Deerinck et al., 2010). The nerve lengths described in Figure 2.2A were obtained at the time of dissection. There can be variation in the thickness of the myelin sheath along the length of the nerve, as well as asymmetries in sheath thickness depending on the position of the axons within the nerve bundle (Fraher, 1992). Therefore, comparisons between the nerves of animals at different developmental stages need to be made at the same location along the length of the nerve and include an analysis of axons in all positions throughout the width of the nerve. The center region of the optic nerve has been previously reported to undergo the most dramatic remodeling during metamorphic optic nerve shortening in *X. laevis* (Cima and Grant, 1982b). Therefore, in order to perform an effective comparison across stages, the centermost region, relative to length, of all nerves was embedded in Durcupan resin in a cross-sectional orientation. Ten micrographs were captured along designated coordinates spanning all regions of the cross-sections for each optic nerve at 5000X magnification using a H7600 Hitachi transmission electron microscope. The sectioning and imaging were both performed at the Wilmer microscopy core by Chung-ha Davis. The TEM micrographs were coded and randomized so that manual tracing could be performed in a blinded manner.

In order to understand how myelin is affected by axon shortening in the metamorphic optic nerve, I performed myelin centered manual tracing of the TEM micrographs. I found that not all myelin was associated with axons, thus myelin was sub-classified into two categories: myelin associated with axons and myelin not associated with a contiguous sheath surrounding an axon, which I refer to as debris myelin. The outermost boundary of the axon associated myelin sheaths, axon plasma membrane, enlargements of the peri-axonal space between the myelin and axon plasma membranes, and debris myelin structures were manually traced as segments in IPLab software. Each component class was assigned a different segment color. An example of the tracing scheme is shown for each stage in Figure 2.2D, in which myelin sheaths are dark blue, axons are yellow, peri-axonal vacuoles are white, and debris myelin is light blue. Afterwards, the segmented areas on the traced images were quantified using custom scripts in IPLab written by my advisor. An independent measure of myelin was also obtained in which myelin was automatically segmented based on it being the most-electron dense structure in the micrographs, using the mean and standard deviation of the manually traced myelin segments to automatically tailor the segmentation cut-offs to different micrographs. The measured values from the ten micrographs for each nerve were combined and normalized to the area of nerve measured relative to the total area of the nerve cross-section. The values from the two nerves from each animal were averaged to obtain a single set of metrics representing each animal.

The myelinated axons of RGCs remodel rather than degenerate in accordance with metamorphic optic nerve shortening

The quantification of the traced TEM micrographs revealed that in conjunction with the nerve as a whole, the myelinated axons also experience a transient hypertrophy specifically during the period of optic nerve shortening. The mean cross-sectional area of myelinated axons increased from $0.68 \pm 0.02\ \mu m^2$ at Stage 58 to $1.12 \pm 0.10\ \mu m^2$ at Stage 66, and then subsequently returned to $0.57 \pm 0.11\ \mu m^2$ within one month following the completion of metamorphosis

(Figure 2.3A). The increased area of the myelinated axons alone, however, is not sufficient to account for the overall hypertrophy of the optic nerve area. An expansion of the extracellular space was visible in the optic nerve TEM micrographs during metamorphic stages, but was not amenable to quantification using contrast based segmentation. Similar increases in extracellular space have been noted during peak periods of myelination in other developing vertebrate systems (Williams et al., 1986). Therefore, an increase in the number of myelinated axons may contribute to the expansion of the optic nerve cross-sectional area during metamorphosis.

Previous studies have indicated that in *X. laevis*, the generation of RGCs in the retina and myelination of axons in the optic nerve is highest during early development, but continues at a low level throughout the lifespan of the animal (Gaze and Peters, 1961; Wilson, 1971). I found that this proliferative trend is not interrupted by optic nerve shortening, since the animals experience an increase in both RGCs and myelinated axon number during metamorphic climax. Using segmentation based quantification of RGCs expressing *rbpms* (also known as *hermes*) (Figure 2.3B), which has been shown to specifically label RGCs in frog the retina (Gerber et al., 1999a) and in mammals (Kwong et al., 2010), the number of RGCs in the retina was found to increase from 29,000 ± 4,640 at Stage 58 to 38,600 ± 5,730 at Stage 62 (Figure 2.3C), which is the period that the optic nerve undergoes the greatest decrease in length (Figure 2.2A). The retina quantification was performed in IPLab using a custom script written by my advisor (Soto et al., 2008). Similarly, the quantification of the traced TEM micrographs indicated that myelination also increased during this period. The number of myelinated axons in the optic nerve increased from 891 ± 101 at Stage 58 to 1,456 ± 302 at Stage 66. The greatest number of myelinated axons, though, was found in the optic nerves of the juvenile frogs, which is consistent with an increase in myelination throughout the lifespan of the animal. The rate of new myelination, however, is highest during metamorphic climax in which an average of 564 ± 320 new axons are myelinated over approximately 10 days for a rate of about 56 ± 31 axons per day. After metamorphosis the rate drops off such that an average of 624 ± 480 axons are myelinated over approximately 30

days leading to a rate of about 21 ± 16 axons per day. Therefore, metamorphic climax likely represents a period of peak myelination in the developing optic nerve of *X. laevis*.

Since new myelination is generally associated with the differentiation of OPCs to mature myelinating oligodendrocytes, I quantified the amount of OPCs, as defined by expression of *pdgfrα*, and mature oligodendrocytes, as defined by expression of *plp*, using *in situ* hybridization in longitudinal optic nerve cryo-sections over the course of metamorphic remodeling (Figure 2.3E). While the numbers of OPCs and oligodendrocytes per unit area were unchanged (Figure 2.3F-G), the total number of mature oligodendrocytes in the optic nerve actually increased during metamorphic climax (Figure 2.3H). This suggests that rate of oligodendrocyte differentiation occurs roughly in proportion to the increase in overall optic nerve area (Figure 2.2B), which would explain why the density of cells was unchanged.

The proliferation of RGCs and increased myelination during metamorphosis raises the possibility that myelinated axons are selectively lost as a result of nerve shortening and replaced with new axons. Therefore, I used immunohistochemistry to determine whether there was a selective loss of myelinated axons specifically at metamorphic climax. The neurofilament marker 3A10 (Brand et al., 1996) labels large caliber axons, which are also surrounded by an Mbp labeled myelin sheath in the optic nerve of *X. laevis* (Figure 2.4A-B). Degenerating axons lose their 3A10 labeling in exchange for the degenerating cell and axon marker, cleaved- caspase-3 (Schoenmann et al., 2010). Metamorphic optic nerve cross-sections were quantified using a segmentation based script in which the total amount of cleaved-caspase-3 signal that did and or did not overlap with Mbp was measured. Quantification of optic nerve cross-sections immunolabeled with Mbp, 3A10, and cleaved-caspase-3 (Figure 2.4C) revealed that there was no increase in cleaved-caspase-3 signal per unit area during metamorphosis (Figure 2.4D). Furthermore, there was no change in the proportion of degenerating myelinated axons during metamorphic climax relative to a time prior to the onset of optic nerve shortening (Figure 2.4E). These results indicate that the existing myelinated axons are not lost during nerve shortening.

Since the myelinated axons are maintained during shortening, it raises the question of how the myelin is affected by this transformation.

Increases in the thickness of the myelin sheath surrounding axons occur after the completion of metamorphosis

In most vertebrate systems, a near linear relationship is maintained between the growth of an axon and the thickness of its corresponding myelin sheath (Friede and Miyagishi, 1972; Friede and Samorajski, 1967), though the exact specifications of this relationship are dependent on axon type and species (Fraher and O'Sullivan, 2000). In some nerves, there can be a large discrepancy in the time between the onset of axon diameter growth and the increase in wraps of the myelin membrane around the axon (Schroder et al., 1978). Since the increase in axon diameter during metamorphosis was a transient effect of remodeling rather than a sustained byproduct of growth, I wanted to determine whether myelin thickness increased concomitantly with axon size, or if a change in myelin thickness was delayed until after the conclusion of optic nerve shortening.

Myelin thickness is generally measured in terms of a G-ratio, which is a measure of diameter of the inner myelin membrane relative to the diameter of the outer myelin membrane, such that an increase in myelin thickness is indicated by a decrease in the G-ratio (Rushton, 1951). The standard calculation of G-ratio relies on the assumption that axon cross-sections are perfectly circular. However, the non-uniformity of axons in the metamorphic optic nerve was evident from the TEM micrographs, which required the modification of the G-ratio calculation. The deviation of axons from perfect circles can also be seen in the developing nerves of other vertebrates (Williams et al., 1986), thus asymmetric growth may indicate a general aspect of development rather than a feature specific to amphibian metamorphosis. Instead of measuring myelin membrane diameters directly in the TEM micrographs, the diameters were extrapolated from the areas bound by the inner and outermost myelin membranes based on the quantification of the traced segments. To differentiate this calculation from a classically defined G-ratio, I refer

to this metric as the G'-ratio. The average values I obtained for G'-ratio, between 0.7 and 0.8, were highly consistent with the G-ratios calculated in the nerves of other species (Berthold et al., 1983; Chomiak and Hu, 2009; Wakakuwa et al., 1987). The distribution of G'-ratios was relatively unchanged over the course of optic nerve shortening (Figure 2.5A). A significant shift in the distribution toward lower G'-ratios, or increased myelin thickness, did not occur until well after the completion of metamorphosis and nerve remodeling. This suggests that oligodendrocytes do not respond to the sudden axon hypertrophy during metamorphic climax with a compensatory increase in myelin thickness, but rather wait until remodeling has been completed and the nerve has stabilized.

Axons have excess myelin relative to their size and also have focal enlargements of the peri-axonal space during metamorphic optic nerve remodeling

The G-ratio provides a metric of myelin thickness, but since it does not directly measure the size of the axon, it provides an incomplete description of the relationship between myelin and axons and how it may be affected by nerve shortening. The shortening of the axon might be expected to lead to a disassociation of myelin from the axon. A measure of the total area of myelin per optic nerve cross-section was highest at Stage 66, even though the total number of myelinated axons and the thickness of the myelin around each of those axons were greatest in the juvenile frog (Figure 2.5B). This suggests that there is an excess of myelin relative to the number of axons during metamorphosis, which could be indicative of an excess of myelin on each axon or the dissociation of myelin from axons. Therefore, I also examined the ratio of the total area of the myelin sheath relative to the total area of axoplasm, based on the quantification of the segments in the traced TEM micrographs. Although the ratio of myelin: axoplasm did not significantly increase until 4 weeks after metamorphosis, there was a trend toward an elevation in this ratio at the end of metamorphic climax (Figure 2.5C). Since this metamorphic elevation was

not due to an increase in myelin membrane wraps, or thickness, it suggested the presence of local regions of excess myelin.

Breakdown in the adhesion between an axon with the innermost membrane of the myelin sheath can lead to the presence of vacuoles in the peri-axonal space (Trapp et al., 1984), as well as the formation of myelin whorls or tomaculas (Cai et al., 2001; Runker et al., 2004). Indeed, the TEM micrograph cross-sections revealed the presence of focal enlargements of the peri-axonal space at all developmental time points, indicating it may be a general feature associated with the growth of myelinated axons (Figure 2.5D). The size of these focal enlargements of the periaxonal space, however, peaked at the end of metamorphic climax, as the area increased tenfold from 20.8 ± 6.9 μm^2 at Stage 58 to 217 ± 111 μm^2 at Stage 66. These focal peri-axonal space enlargements were not, however, accompanied by the focal splitting of the myelin lamellae. The adhesion between the myelin wraps appeared to remain intact, indicating that these focal detachments were not a byproduct of myelin unraveling or degeneration. This suggests that optic nerve shortening induces the production of focal axon-myelin detachments, perhaps through the local disruption of axo-glia adhesion.

Internodal distance decreases on myelinated axons during metamorphic optic nerve shortening

Myelin does not form a continuous structure along the entire length of an axon, but rather is composed of individual segments; consequently axo-glial adhesion is also not uniform along an axon. Adhesion complexes connecting myelin and axonal membranes are clustered at paranodes (Tait et al., 2000), which are the terminal boundaries of each myelin segment. Based on this non-uniform distribution of adhesive complexes, the internodal regions of myelin with the weakest attachments would be expected to preferentially separate from the axon as it changes shape. I wanted to determine whether the focal enlargements of the peri-axonal space observed in the TEM cross-sections from metamorphic optic nerves were a function of focal internodal myelin

detachments. In addition, the shortening of the axon might lead to disruptions of myelin structure not merely within a segment, but between segments as well. Since the size of the segments is generally optimized to the width and length of the axon, an abrupt decrease in axon size could lead to an overabundance of myelin segments relative to axon length. Depending on how the axon shortens relative to the position of the myelin segments, the intervening nodal regions between segments, which contain high densities of sodium channels necessary for maintain salutatory conduction, could be lost as segments run up against one another.

In an initial attempt to ascertain whether adhesion complexes remained intact at paranodes and whether myelin segment spacing or length was affected by nerve shortening, I used an immunohistochemistry based approach. Optic nerve longitudinal cryo-sections were immunolabeled with antibodies to the myelin marker Mbp, the axonal marker 3A10 and the paranodal marker Neurofascin (Tait et al., 2000). Three-dimensional projections of the nerves obtained through confocal imaging were used to trace the distance between Neurofascin labeled paranodes along individual myelinated axons. The basic structure of the paranode, as determined by Neurofascin immunolabeling was maintained throughout the period of optic nerve remodeling (Figure 2.6A). Since Neurofascin is an integral part of the paranodal adhesive complex, it is likely that the preservation of Neurofascin labeling indicates that the adhesive complexes themselves are also maintained. The resolution of the immunolabeling of myelin with Mbp, however, was not sufficient to clearly delineate individual segments. Consequently, nodal structure and the spacing between segments could not be examined. The tracing of segments along axons defined by Neurofascin labeled boundaries, did reveal a change in segment length during the period of optic nerve shortening. The distance between Neurofascin labeled paranodes (internodal distance) decreased by approximately one-half from 50.3 ± 11.6 μm at Stage 58 to 28.3 ± 6.9 μm at Stage 66, the immediate conclusion of nerve shortening (Figure 2.6B). Interestingly, the segment shortening appears to have been primarily accomplished between Stage 58 and Stage 62, as the segment length did not decrease further between Stages 62 and 66. Due to the high density of

axons, individual axons could not be traced reliably, thus this method was not suitable for obtaining myelin segment length from 4 week post-metamorphic animals.

Myelin segments on axons shorten during metamorphic optic nerve shortening

In order to determine how the structure of the myelin segments was affected during shortening, I performed three-dimensional reconstructions of myelinated axons from SBEM datasets obtained from the optic nerves from animals at Stages 58, 62, 66, and 4 weeks after metamorphosis. The optic nerves were dissected and processed for SBEM as previously described, and embedded in Durcupan resin in a longitudinal manner. After embedding, all further processing and imaging was performed by Eric Bushong and colleagues in the laboratory of Mark Ellisman at the National Center for Microscopy and Imaging Research. I manually traced the boundaries of the outer myelin membrane (blue), axon plasma membrane (yellow), and peri-axonal space enlargements (white) using Imod software (Kremer et al., 1996) of approximately ten axons per stage in order to create the reconstructions (Figure 2.7A). The axons were selected based on the criteria of containing nodes, the spaces between myelin segments, and preferentially multiple nodes. This selection criterion could not be used for the Stage 58 dataset, however, as the length of the myelin segments exceeded the dimensions of the volume such that the traced axons contained at most a single node. As a result, I was able to obtain the length of myelin segments for a majority of the axon reconstructions for optic nerves from animals at each stage except Stage 58.

In this way, I was able to confirm that myelin segments shorten to at least one-half of their original length during metamorphic climax (Figure 2.7B). There was a small discrepancy between the lengths of myelin segments measured using the immunohistochemistry and electron microscopy based methods, but due to the difficulty in unambiguously tracing the immunolabeled axons and the higher resolution afforded by the SBEM volumes, the values based on the reconstructions are likely to be more accurate. The reconstructions also revealed that myelin

segments were appropriately separated by intervening nodal regions and that segment lengths were not uniform. Since myelin segment length generally varies with axon size, a nerve containing axons of a wide variety of calibers, such as the optic nerve, would be expected to normally have a fair amount of segment length variation. The metamorphic nerves, however, also displayed intra-axonal myelin segment length variation. The presence of extremely short segments alongside longer ones such as on axons Stage 62 #7 and Stage 66 #3 in Figure 2.7A, suggest that at least some of the myelin segments are eliminated during optic nerve shortening, and that the intervening space is filled by the elongation of neighboring segments. This hypothesis is supported by the unexpected finding that myelin segments lengthen dramatically during the first 4 weeks after the completion of metamorphosis (Figure 2.7B), without a significant change in overall optic nerve length (Figure 2.2A). Since segment lengthening has been previously described in other developmental systems (Court et al., 2004; Fried et al., 1982; Friede et al., 1985), I chose to focus my efforts on determining the mechanism involved in the novel finding that myelin segments shorten during metamorphic climax.

Myelin segments structurally remodel to produce detachments, branches, and protrusions on shortening axons

The myelinated axon reconstructions indicate that myelin segments undergo significant structural changes during the period of optic nerve shortening, aside from changes in length. Small regions where the innermost myelin membrane has separated from the axon plasma membrane, accompanied by focal enlargements of the peri-axonal space occur frequently along the length of the metamorphic axons (Figure 2.7A). Additionally, there are protrusions of myelin extending from the myelin sheath at positions which continue to exhibit intact axo-glial attachments. Although some focal myelin detachments and myelin protrusions can be detected in axons from all developmental stages examined, the size and frequency of these myelin aberrations were found to be greatly increased specifically during the period of metamorphic

optic nerve remodeling (Figure 2.7C-D). The focal detachments often form in clusters, as clearly shown in axon Stage 62 #1 in Figure 2.7A, suggesting that the disruption of axo-glial adhesion in one region of the myelin segment may negatively affect the stability of the myelin in neighboring regions. Indeed the continued expansion of peri-axonal space vacuoles during remodeling (Figure 2.7D) suggests that the adhesive complexes between detached regions get disrupted leading to the expansion of the detached region. This would result in the production of fewer, but larger stretches of detached myelin, which would be less stable and prone to form whorled and folded structures, both of which are readily detectable in the electron microscopy micrographs primarily at Stage 66.

Several axons had out-branching of the axon itself, suggesting that part of the mechanism of axon shortening may involve axon branching, thus many of the myelin dystrophies may develop from the folding and cytoskeletal reorganization of the axon during remodeling. It is likely that this branching of axons and formation of the myelin detachments and out-foldings accounts for the decreased length of the myelin segments in metamorphic axons. Similarly, the branched and folded myelin would also account for the increase in the cross-sectional area of myelin (Figure 2.5C) that is independent of any change in myelin wrapping or thickness (Figure 2.5A) during the period of optic nerve remodeling.

Although the full length of the myelin segments in the pre-metamorphic (Stage 58) axons could not be quantified, due to the size of the dataset relative to the length of the segments, the similarity of appearance and many other metrics between the pre-metamorphic axons and those 4 weeks after metamorphosis (Figures 2.2D, 2.3A, 2.5D) meant that some metrics obtained for the post-metamorphic axons could be used as a reasonable approximation for pre-metamorphic axons. The segment lengths at 4 weeks are likely similar to pre-metamorphic lengths, based on lengths obtained through Neurofascin labeling (Figure 2.6B). Using this approximation, the surface area of myelin segments could be compared over the course of optic nerve remodeling. These approximations revealed that even though segment lengths at 4 weeks after metamorphosis

(or before metamorphic climax) were on average over twice as long as during metamorphic climax (Figure 2.7B), the surface area of myelin on the segments remained relatively constant at all examined stages (Figure 2.7E), further supporting that shortening involves the reorganization of existing myelin segments. Furthermore, in the myelinated axons from animals 4 weeks after metamorphosis, the myelin is relatively uniform and lacks axon branching or large dystrophies. This indicates that the branching and out-pocketing of axon and myelin material are likely remodeling intermediates that are eventually targeted for removal. Therefore, I wanted to determine how regions of out-branched and/or detached myelin could be selectively removed from axons without resulting in axon degeneration.

A population of myelin and axon material separated from myelinated axons increases in the optic nerve during metamorphic climax

If regions of axon branching and myelin protrusions are removed from axons, this would lead to the production of populations of axonal material and myelin that were fully separated from intact axons and located within the extracellular space or inside of a phagocytic cell. I first attempted to identify the populations of axonal material and myelin not associated with intact axons in the metamorphic optic nerve using immunohistochemistry. Thick longitudinal cryo-sections of optic nerve at Stages 58, 62 and 66 were immunolabeled with the myelin marker Mbp and axon marker 3A10, which preferentially labels large-caliber myelinated axons (Figure 2.9A). In addition, I used a second axonal marker, gamma synuclein (Sncg), which is highly enriched in RGCs (Soto et al., 2008) in order to identify membranes and other material derived specifically from axons (Figure 2.9B). I designed an antibody to the acidic C-terminus of *Xenopus* Sncg based on a similar antibody developed for Sncg in mouse (Soto et al., 2008) which has been shown to retain partial antigenicity in the optic nerve following treatment with proteases (Nguyen et al., 2011). Although expressed in all RGCs (Figure 2.8A), *sncg* is more highly expressed in RGCs that also express heavy neurofilament (Figure 2.8B), and consequently have large caliber

myelinated axons (Figure 2.8C-D). Additionally, the synucleins associate with membranes rather than neurofilaments and have been found on vesicles outside of axons (Auluck et al., 2010). Therefore, although Sncg and 3A10 label overlapping populations of axons (Figure 2.8E-F), Sncg to is better suited to label material that is derived from RGC axons but is no longer associated with them.

The 3A10 immunolabeled signal was used to create a mask using Imaris software (Bitplane) such that any Mbp (or Sncg) signal that overlapped with the 3A10 mask was filtered out. Using this paradigm, a population of Mbp immunolabeled myelin that was clearly not associated with 3A10 immunolabeled axons was evident in the nerves during the period of optic nerve remodeling (Figure 2.9A). This population peaked at 4.5 ± 1.9% of the total amount of myelin at Stage 62, during mid-metamorphic climax (Figure 2.9C). Similar results were obtained with the population of axonal material that was separated from intact axons, which peaked to 12.1 ± 6.6% of the total Sncg immunolabeled signal at Stage 62 (Figure 2.9D). Furthermore, there was a high degree of co-localization between the populations of axonal and myelin material that were not associated with intact axons (Figure 2.9E). The finding that the populations of separated material peaked at Stage 62 was unexpected given that myelin segments are still structurally abnormal at Stage 66, which suggests that a large percentage of the myelin dystrophies are not removed until after Stage 66, during the first few weeks after metamorphosis. This result may indicate that this method of immunohistochemistry and light level microscopy does not provide sufficient resolution to identify the entire population of myelinated axon derived material separated from axons, that some of the separated material has lost its antigenicity, or both.

Excess myelin on shortening axons is removed and accumulates inside neighboring cells in the optic nerve

In order to overcome the limited resolution of light microscopy and confirm the presence of a population of myelin that is separated from axons, I used electron microscopy. The tracing of

the TEM micrographs from optic nerve cross-sections, as shown in Figure 2.2D, involved the segmentation of a population of myelin not associated with a contiguous myelin sheath. This population was composed of myelin in a variety of states ranging from whorled excess myelin stemming from an intact segment to separated myelin fully internalized within another cell (Figure 2.10A). One class of the myelin intermediates (Figure 2.10A ii) shows myelin surrounded by the fine lamellar processes of a nearby cell, and likely represents one of the mechanisms by which myelin protrusions are removed from segments. The debris myelin was sub-classified based on appearance into the categories depicted in Figure 2.10A (Figure 2.10B). A large percentage (35-45%) of debris myelin consisted of transitional myelin intermediates that could not be readily classified into a single category and likely represented myelin in the process of being internalized.

Since the majority of the debris myelin at all stages is fully internalized, its source cannot be readily identified, and thus could be a byproduct of either active myelin removal from intact axons or myelin degeneration. The absence of an increased loss of myelinated axons (Figure 2.4E) along with the presence of debris intermediates would suggest that at least during metamorphosis, the majority of internalized myelin is not due to axon loss. The shift in the distribution of myelin intermediates showing an increase in whorled myelin extending from axons and being enwrapped by cellular processes from approximately 5% at Stage 58 to 25% at Stage 66 further supports the notion that metamorphic debris myelin is an indication of myelin remodeling rather than axon degeneration. The total area of this debris myelin increased from 6.8 ± 4.1μm^2 at Stage 58 to 492 ± 247 μm^2 at 66 (Figure 2.10C). As a result, the percentage of myelin not associated with axons also increased significantly during the period of metamorphic optic nerve remodeling (Figure 2.10D). In contrast to the Mbp immunolabeling results, the peak of debris myelin occurred at Stage 66, at which time approximately one-quarter (24.9 ± 8.8%) of all myelin in the optic nerve was found separated from axons. The discrepancy between the immunolabeling and electron microscopy metrics is likely explained by localization of the

majority of the debris myelin within cells since this internalization may have led to a corresponding loss of antigenicity of the myelin. This finding also explains why total myelin levels peaked at Stage 66 rather than 4 weeks after metamorphosis (Figure 2.5B), despite the increased number of myelinated axons at the later time point (Figure 2.3D). Altogether these results suggest that there is large scale removal of myelin from axons during metamorphosis, and that the majority of the removed myelin is associated with astrocytes.

Focal regions of detached and branched myelin are contacted and removed from otherwise intact segments on axons by the cellular processes of nearby cells in the optic nerve

In order to confirm that the debris myelin intermediates seen in the TEM micrographs represent the selective removal of focal myelin dystrophies on otherwise intact myelin segments, I looked for evidence of the active removal of myelin on the axon reconstructions from SBEM datasets. Cellular processes from neighboring cells were found to contact remodeling myelin segments, shown in red in Figure 2.11A. Furthermore, the contact sites occurred preferentially at regions with focal myelin detachments or protrusions, as highlighted by boxed regions in Figure 2.7A. The Stage 66 axon # 6 contains a long thin out-branch in which the myelin at the end is fully enclosed within a neighboring cell but remains attached to the main axon at its base. A similar, but likely, earlier, event is captured in Figure 2.11B, which appears to provide a snapshot of the mechanism of myelin removal. An out-branch of the Stage 62 axon is enwrapped by thin lamellar processes of a local cell, whose soma contains evidence of previously internalized axon and myelin material. The internalized myelin appears to be in various stages of degradation, suggesting that the internalized material localizes to degradative compartments within the cell.

Internalized myelin accumulates within cells in the optic nerve and is associated with a rise in lipid droplet production

The accumulation of internalized myelin within degradative cellular compartments would account for the finding that increases in the size of individual units of debris myelin coincide with increases in the total amount of debris myelin (Figure 2.12A). The size of debris myelin units increases from $0.5 \pm 0.2\ \mu m^2$ at Stage 58 to $1.9 \pm 0.2\ \mu m^2$ at Stage 66, over the same time course that total debris levels in the optic nerve elevate dramatically (Figure 2.10C-D). Similarly, both the size of debris myelin units and amount of total debris fall back to pre-metamorphic levels in the optic nerves from juvenile frogs. The accumulation of internalized debris myelin is also correlated with an increase in the number and size of lipid droplets in the myelin internalizing cells (Figure 2.12B-E). The accumulation of lipid droplets within phagocytes has long been associated with myelin internalization and degradation (Stoll et al., 1989). Therefore, the increased presence of the lipid droplets is a further indicator that myelin is removed from axons and internalized for degradation by neighboring cells during metamorphic optic nerve shortening.

Overall, my data shows that myelinated axons in the optic nerve of *X. laevis* remodel rather than degenerate during metamorphic optic nerve shortening. The RGC axons undergo a transient hypertrophy and out-branching as they shorten which is accompanied by the creation of focal axon-myelin detachments and myelin protrusions on otherwise intact myelin segments. The production of these myelin extensions and branches then results in the shortening of the myelin segments. Finally, these regions of dystrophic myelin are selectively removed and internalized for degradation by neighboring cells in the optic nerve.

Figure 2.1 Morphological changes in *X. laevis* head during metamorphosis

Nieuwkoop and Faber (NF) staged *X. laevis,* at pre-metamorphic Stage 58, metamorphic climax Stage 62 and immediately post-metamorphic Stage 66 illustrate head remodeling. Scale bar = 1 cm.

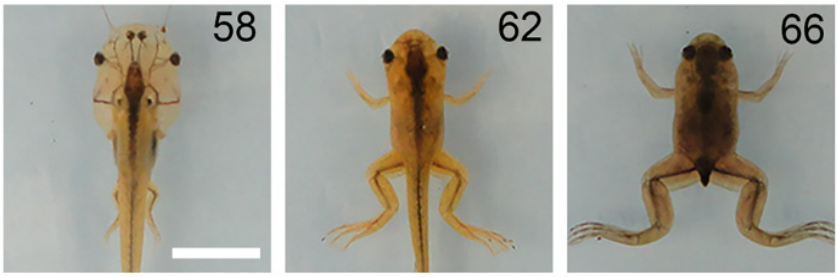

Figure 2.2 The optic nerve shortens and transiently widens but remains structurally intact during metamorphosis

(A) Optic nerve (ON) length during metamorphosis (n= 6). F= 4 weeks post-metamorphic froglets. **(B)** Optic nerve cross-sectional area (n= 6). **(C)** Optic nerve cross-sectional cryo-sections immunolabeled for acetylated tubulin (blue, axons), Blbp (green, astrocytes), and Mbp (red, oligodendrocyte myelin). Scale bar = 50 μm. **(D)** Representative traced transmission electron microscopy (TEM) micrographs of the optic nerve cross-sections at Stages 58, 62, 66, and 4 weeks post-metamorphosis (F). Myelin sheaths (blue), axoplasm (yellow), focal peri-axonal space enlargements (white), and non-axon-associated myelin (cyan). Scale bar = 2 μm. Measurements show mean ± SD with *P < 0.05, **P < 0.01, and ***P < 0.001 by Games-Howell test.

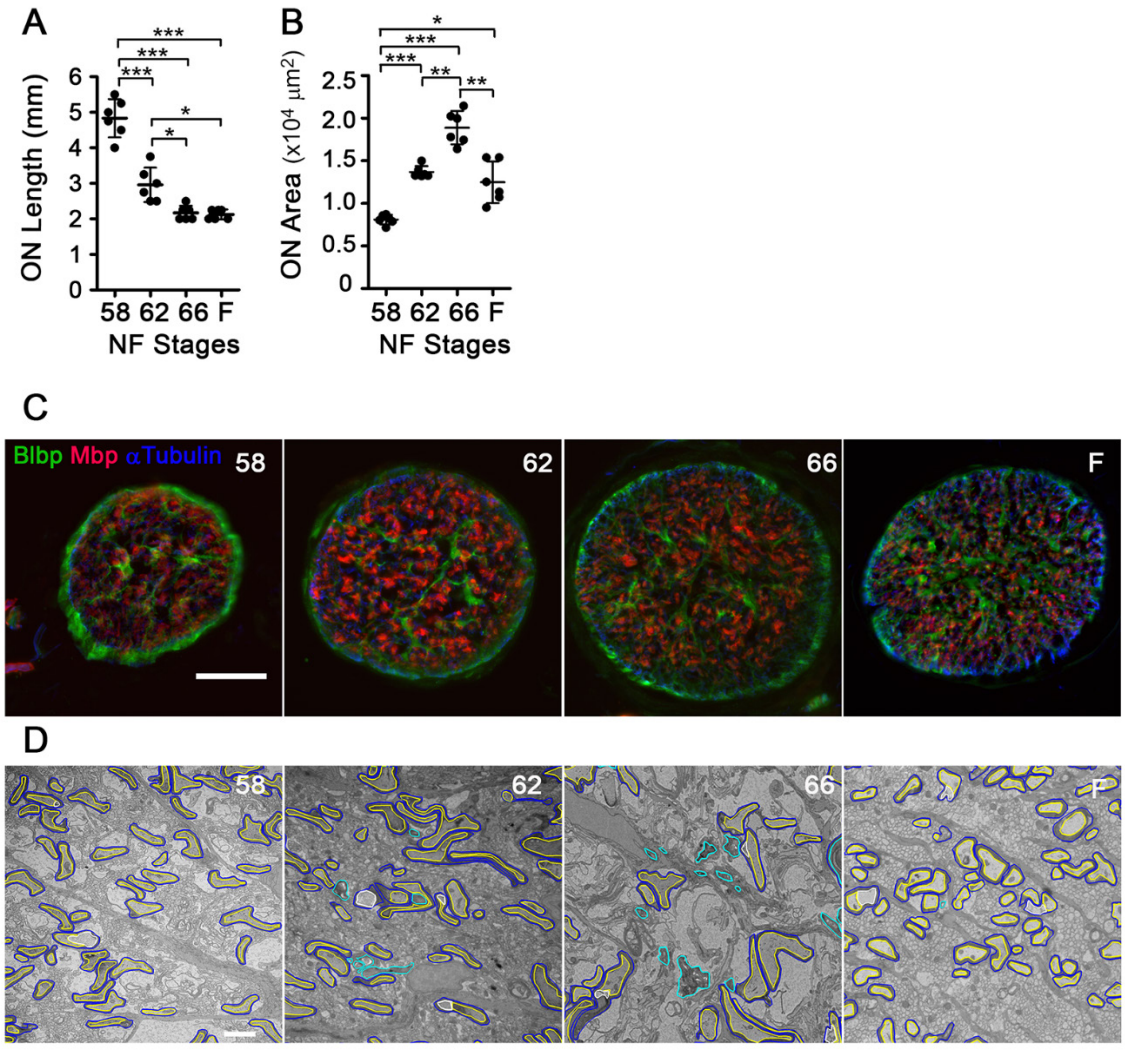
A
ON Length (mm)
0
1
2
3
4
5
6
***
***
***
*
*
58 62 66 F
NF Stages
B
ON Area (x10^4 µm^2)
0
0.5
1.0
1.5
2.0
2.5
*
***
***
**
**
58 62 66 F
NF Stages
C
Blbp Mbp αTubulin
58
62
66
F
D
58
62
66
F

Figure 2.3 Retinal ganglion cells proliferate and myelination increases in optic nerve during metamorphic climax

(A) Average axoplasm cross-sectional area in myelinated axons per optic nerve (n= 6) from traced TEM micrographs. Values derive from measurement of 6975, 5759, 5267, and 6076 axons at Stages 58, 62, 66, and F respectively. **(B)** Images of whole-mount retina mosaics expressing the retinal ganglion cell marker *rbpms*, at Stages 58 and 62. Scale bar 100 μm. **(C)** Counts of retina ganglion cells, as determined by *rbpms* expression, per retina at Stages 58 and 62. **(D)** Number of myelinated axons per optic nerve (n= 6), derived from traced TEM micrographs, at Stages 58, 62, 66, and F. **(E)** Optic nerve 10 μm thick longitudinal cryo-sections following *in situ* hybridization showing expression of *plp* (green, oligodendrocytes), *pdgfrα* (red, oligodendrocyte precursor cells), and Dapi (blue, nuclear marker) at Stages 58, 62 and 66. Scale bar = 50 μm. **(F)** Counts of *pdgfrα* expressing cells per optic nerve longitudinal cryo-section normalized to area at Stages 58, 62, and 66. **(G)** Counts of *plp* expressing cells per optic nerve longitudinal cryo-section normalized to area at Stages 58, 62, and 66. **(H)** Counts of *plp* expressing cells per optic nerve longitudinal cryo-section, at Stages 58, 62, and 66. Measurements show mean ± SD with *$P < 0.05$, **$P < 0.01$, and ***$P < 0.001$ by Games-Howell test (A) and (D), Tukey's test (F-H), or Student's t-test (C).

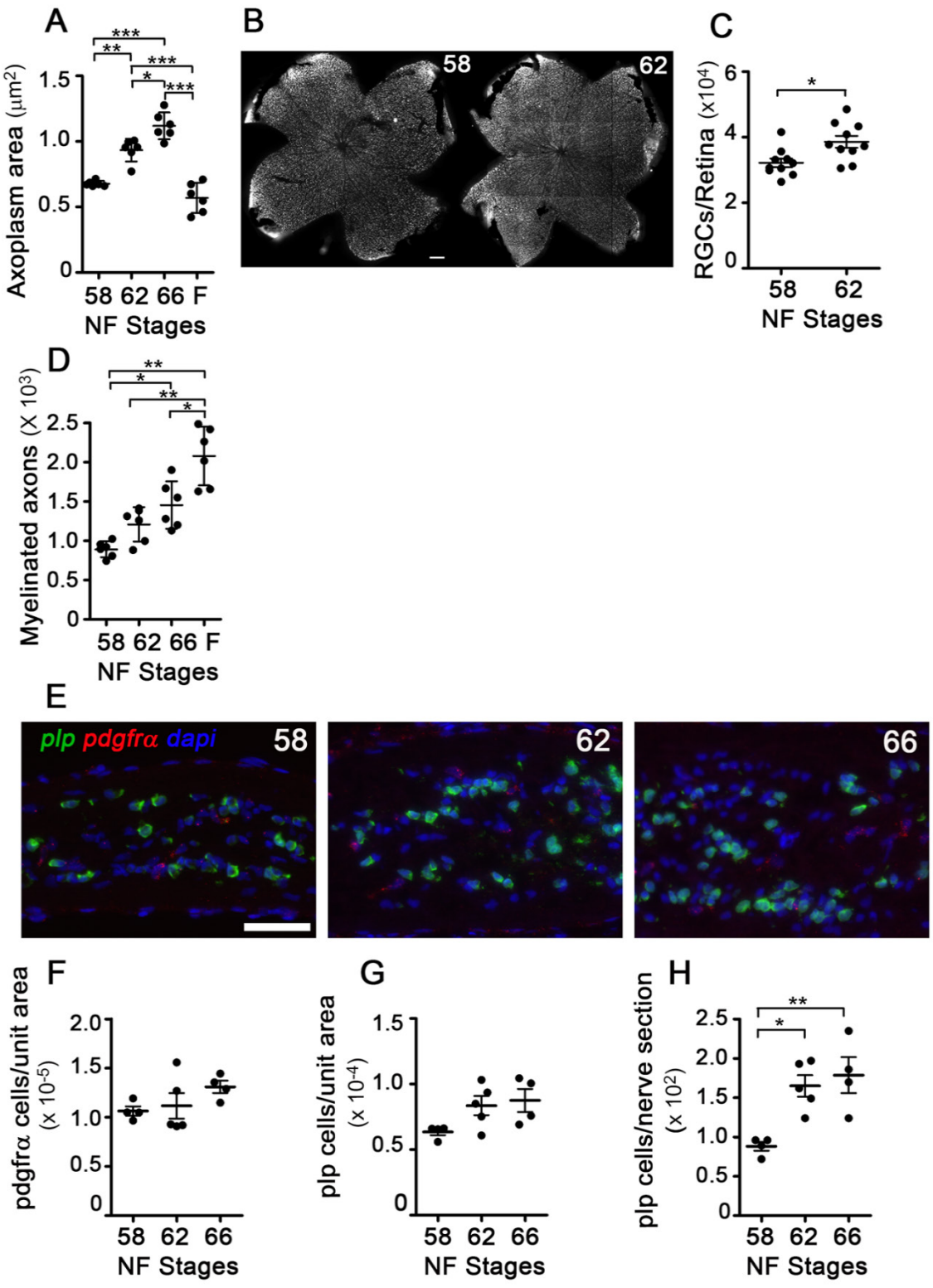
A
Axoplasm area (μm²)
1.5
1.0
0.5
0
58 62 66 F
NF Stages
B
58
62
C
RGCs/Retina (x10⁴)
6
4
2
0
58 62
NF Stages
D
Myelinated axons (X 10³)
2.5
2.0
1.5
1.0
0.5
0
58 62 66 F
NF Stages
E
plp pdgfrα dapi
58
62
66
F
pdgfrα cells/unit area (x 10⁻⁵)
2.0
1.5
1.0
0.5
0
58 62 66
NF Stages
G
plp cells/unit area (x 10⁻⁴)
1.5
1.0
0.5
0
58 62 66
NF Stages
H
plp cells/nerve section (x 10²)
2.5
2.0
1.5
1.0
0.5
0
58 62 66
NF Stages

Figure 2.4 Myelinated axons are maintained during metamorphic optic nerve shortening

(A) Confocal images of Stage 58 cross-sectional cryo-section showing that the 3A10 neurofilament marker (red) preferentially labels axons bound by Mbp (green) compared to pan axonal marker (acetylated tubulin, red). Scale bar = 20 μm. **(B)** Pearson's coefficient of co-localization between axon and myelin markers, derived from confocal images (n= 10 ONs). ***P < 0.001 by Student's t-test with Welch's correction. **(C)** Confocal images of Stages 58, 62 and 66 optic nerve immunolabeled cryo-sections. Immunolabeling of myelin sheath labeled by Mbp (blue), large caliber axons labeled by 3A10 (red), and degenerating axons labeled by cleaved-caspase 3 (green) show no increase in degenerating myelinated axons at metamorphosis. Scale bar = 20 μm. **(D)** Cleaved-caspase-3 signal in optic nerve measured from cross-sectional confocal images (n= 10 per stage) normalized to area does not change during metamorphosis. Significance assessed by the Games-Howell test. **(E)** Cleaved-caspase-3 signal in myelinated axons (MA) measured from confocal images (n= 10 per stage) normalized to area does not change over metamorphosis. Significance assessed by Tukey's test. All measurements show mean ± SD.

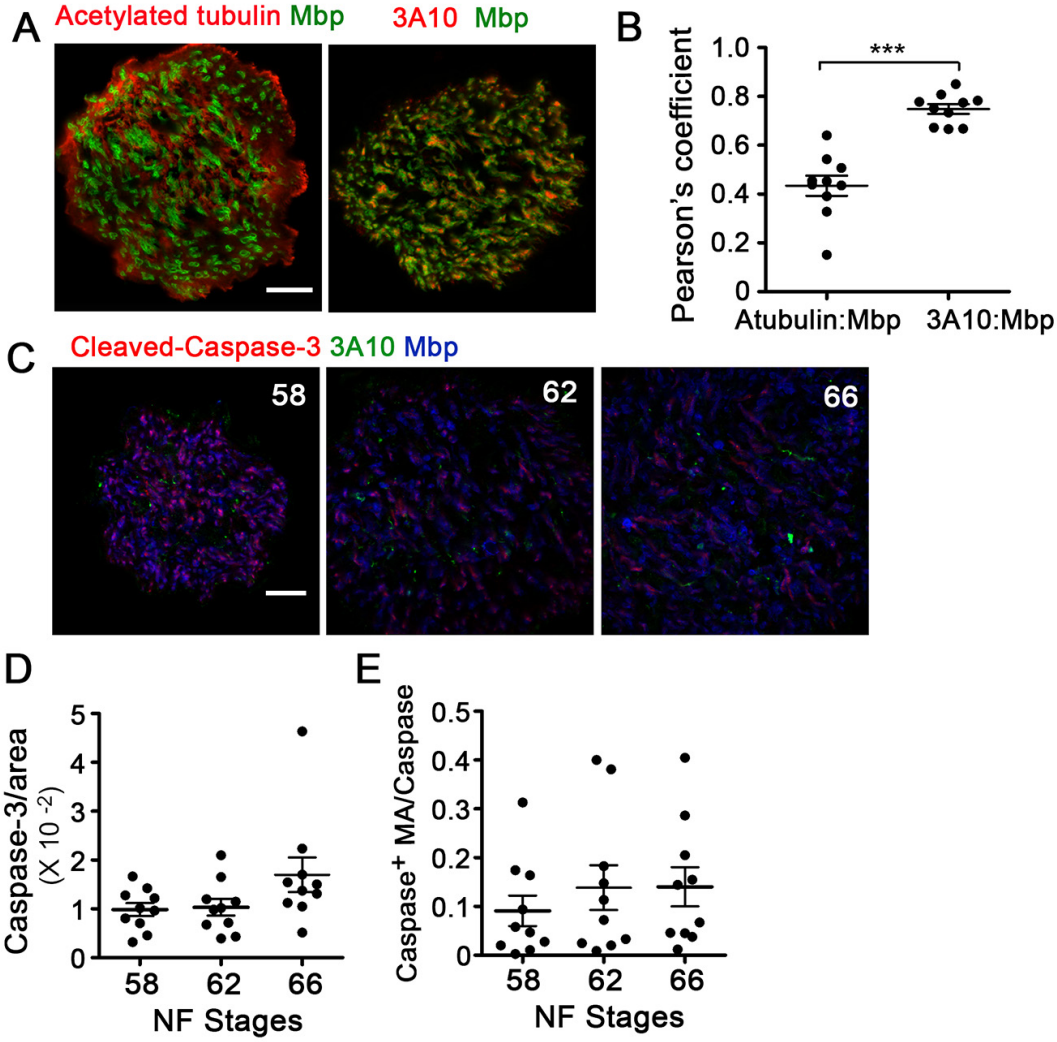
A
Acetylated tubulin Mbp
3A10 Mbp
B
Pearson's coefficient
1.0
0.8
0.6
0.4
0.2
0
***
Atubulin:Mbp
3A10:Mbp
C
Cleaved-Caspase-3 3A10 Mbp
58
62
66
D
Caspase-3/area
(X 10 -2)
5
4
3
2
1
0
58
62
66
NF Stages
E
Caspase+ MA/Caspase
0.5
0.4
0.3
0.2
0.1
0
58
62
66
NF Stages

Figure 2.5 Area of myelin surrounding axons increases during optic nerve shortening, but not through myelin thickening

(A) Frequency distributions of G' ratios (from 6975, 5759, 5267, and 6076 axons at Stages 58, 62, 66, and F, respectively). G' ratio calculated as the ratio of the area bound by inner myelin membrane to the area bound by the outer myelin membrane. **(B)** Total area of myelin per optic nerve cross-section (n= 6). **(C)** Mean ratio of myelin area over axoplasm area per axon. Individual axon ratios averaged per optic nerve (n= 6). **(D)** Total cross-sectional area of peri-axonal space under focal myelin detachments per optic nerve (n= 6). All measurements show mean ± SD and were derived from traced TEM micrographs. *P < 0.05, **P < 0.01, ***P < 0.001 by the Games-Howell test.

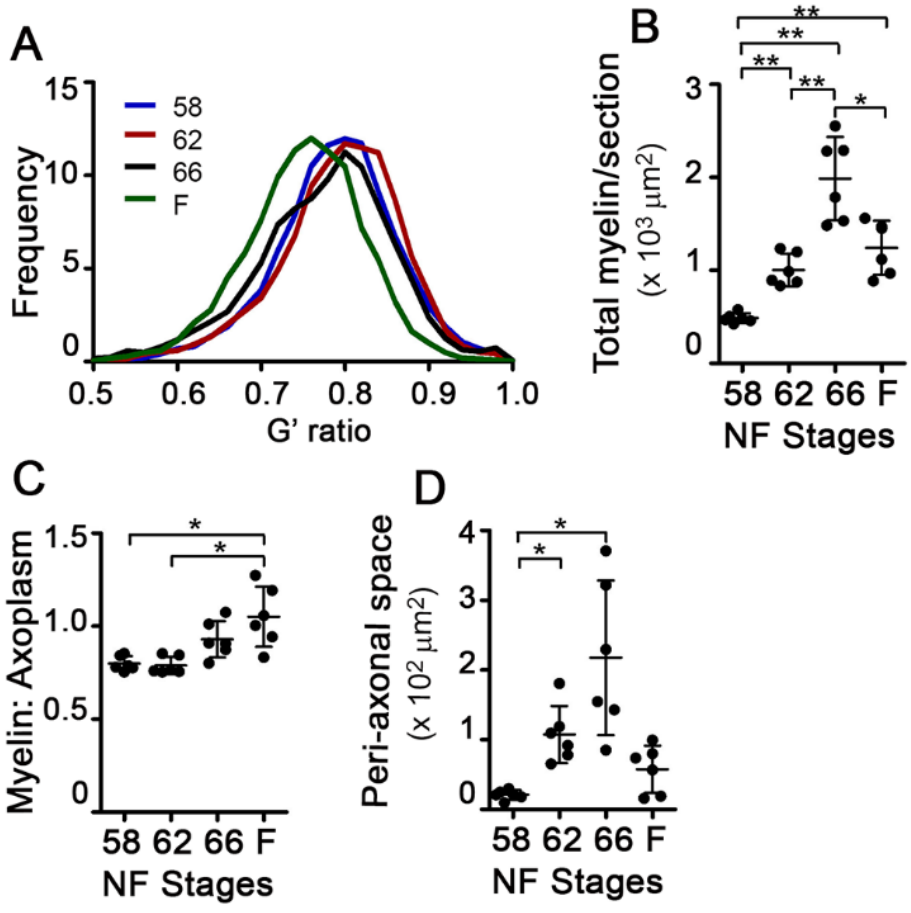

Figure 2.6 Internodal distance decreases during metamorphic optic nerve shortening

(A) z-stacks of confocal imaged optic nerve longitudinal cryo-sections immunolabeled for the large-caliber axon marker, 3A10 (green), and the paranodal marker, Neurofascin (red), show an increased density of paranodes at Stages 62 and 66 relative to Stage 58. Scale bar = 50 μm. **(B)** Internodal distances (n= 23, 28, 28 and 26 axons at Stages 58, 62, 66, and F derived from 3 optic nerves per stage) measured in 3A10 and Neurofascin-labeled optic nerve volumes. Measurement shows mean ± SD. ***P < 0.001 by Tukey's test.

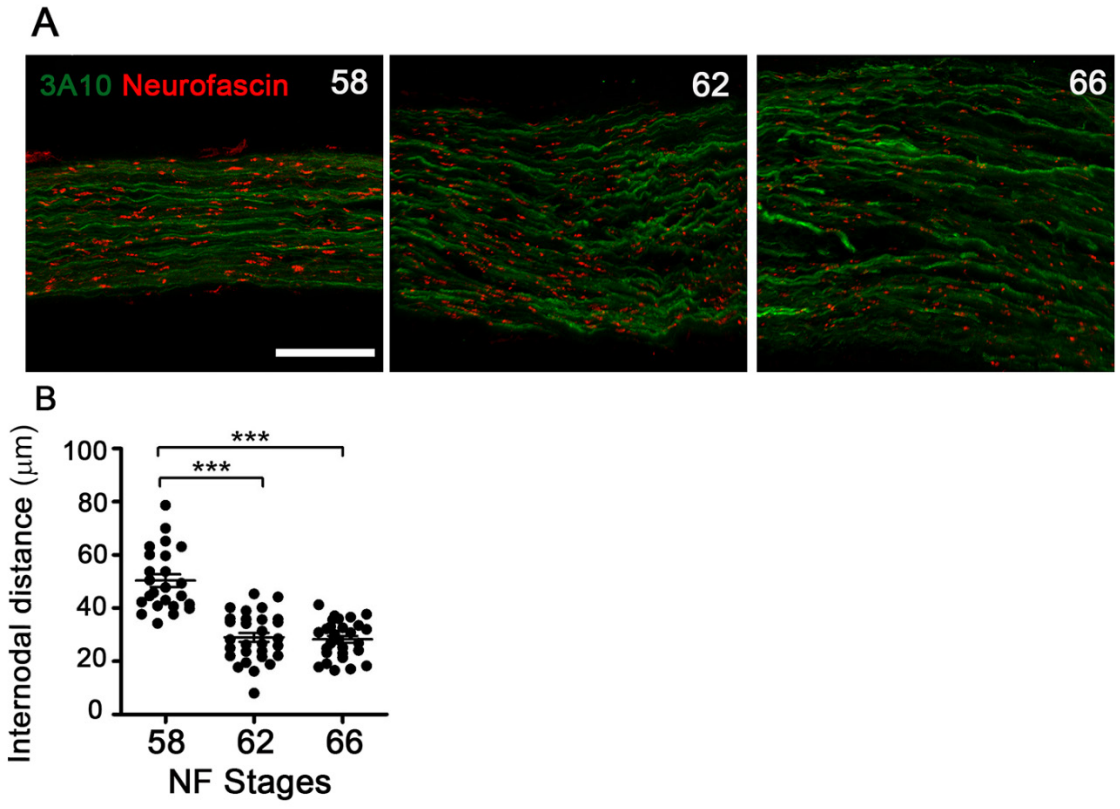

Figure 2.7 Myelin segments remodel and shorten during metamorphic optic nerve shortening

(A) Reconstructions of axons at Stages 58, 62, 66 and F based on SBEM datasets, with myelin (light and dark blue), axoplasm (yellow), focal peri-axonal space enlargements (white), and Nodes of Ranvier (arrows) show focal myelin protrusions and detachments during metamorphic stages. Scale bar = 5 μm. Boxed regions are also shown in Figure S3. **(B)** Myelin segment lengths measured from SBEM traced axons. Stage 58 values (gray) are minimum lengths since they generally exceeded the acquired volume dimensions. Values were derived from 10, 8, 6, and 8 segments at Stages 58, 62, 66 and F, respectively. **(C)** Surface area of myelin in focal detachments on axons normalized to length (n= 11 Stages 58 and 66, n= 9 Stage 62 and F). **(D)** Volume of peri-axonal space beneath focal myelin detachments on axons per axon normalized to length (n= 11 Stages 58 and 66, n= 9 Stage 62 and F). **(E)** Surface area of myelin per myelin segment (n= 7, 5, and 8 for Stages 62, 66, and F, respectively). All measurements show mean ± SD and were derived from SBEM axon reconstructions. *$P < 0.05$ and **$P < 0.01$ by the Kruskal- Wallis test (B), the Games-Howell test (C-D), or Tukey's test (E).

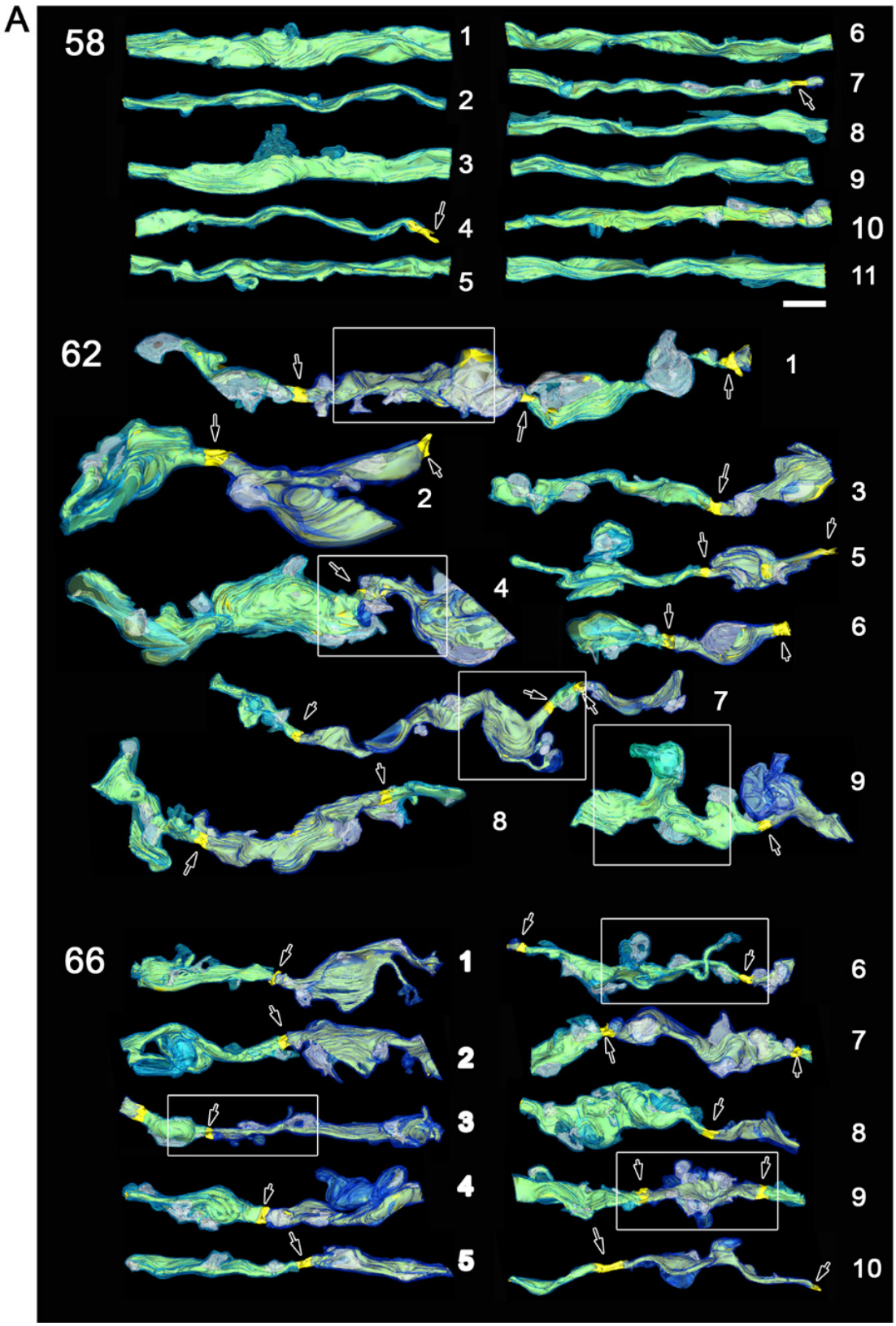
A
58
1
2
3
4
5
6
7
8
9
10
11
62
1
2
3
4
5
6
7
8
9
66
1
2
3
4
5
6
7
8
9
10

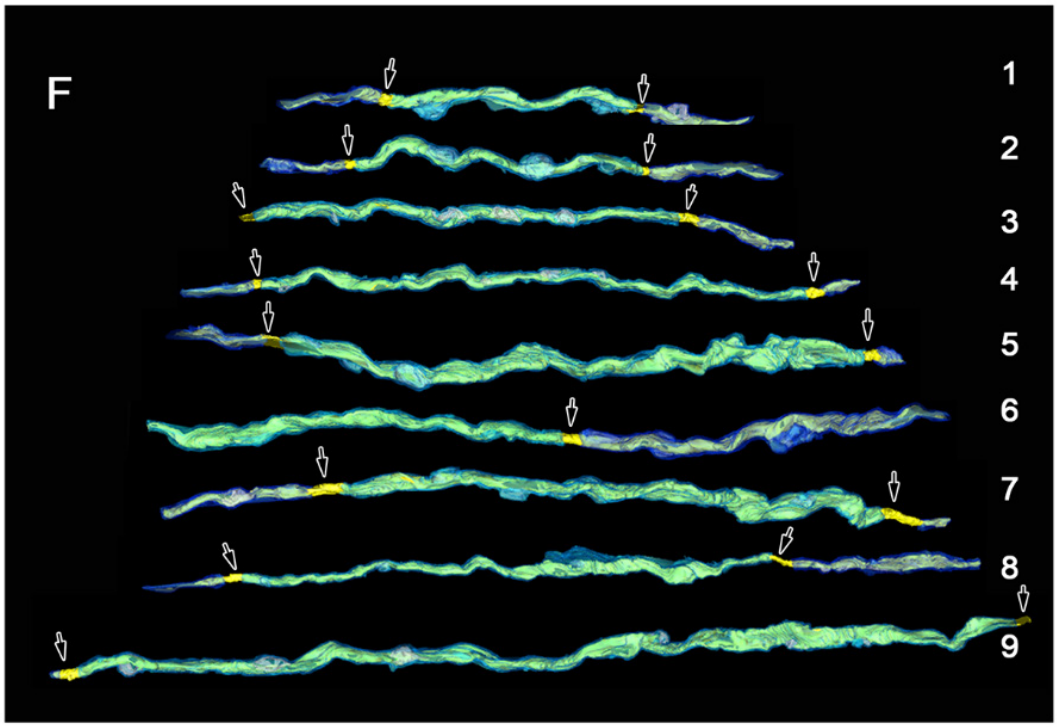
F
1
2
3
4
5
6
7
8
9

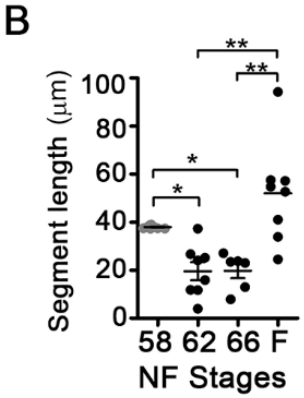
B
Segment length (μm)
100
80
60
40
20
0
58 62 66 F
NF Stages

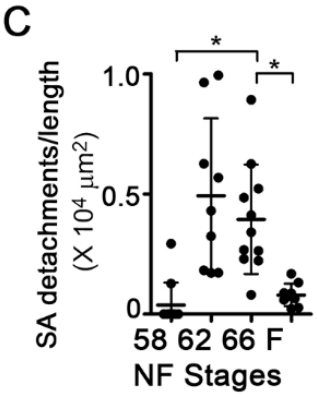
C
SA detachments/length
(X 10^4 μm^2)
1.0
0.5
0
58 62 66 F
NF Stages

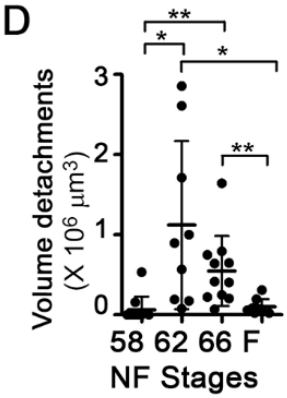
D
Volume detachments
(X 10^6 μm^3)
3
2
1
0
58 62 66 F
NF Stages

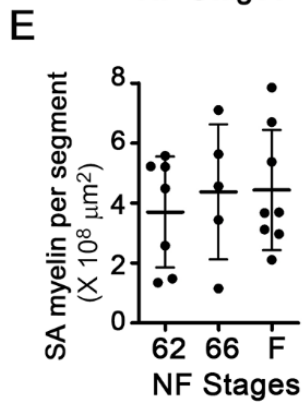
E
SA myelin per segment
(X 10^8 μm^2)
8
6
4
2
0
62 66 F
NF Stages

Figure 2.8 Gamma synuclein is highly expressed in RGCs with large caliber myelinated axons

(A) Sub-selection of Stage 62 whole-mount retina immunolabled with gamma synuclein (Sncg, green) showing that it is expressed in the same cells as the mRNA for the RGC marker, *rbpms* (red). Scale bar = 50 μm. **(B)** Sub-selection of Stage 62 whole-mount retina showing co-localization of mRNA for heavy neurofilament (*nefh*, green) in RGCs that highly express *sncg* mRNA (red). Scale bar = 50 μm. **(C)** Sub-selection of Stage 62 whole-mount retina immunolabeled with large caliber axon marker, 3A10 (green) showing the RGCs which have high expression of *sncg* mRNA (red) are labeled with 3A10. Arrows show cells labeled by both 3A10 and *sncg.* Scale bar = 50 μm. **(D)** Immunolabled confocal images of Stage 58 cross-sectional optic nerve cryo-section shows co-localization of Sncg (red) with Mbp or 3A10 (green). Scale bar = 20 μm. **(E)** Pearson's coefficient showing co-localization of Sncg with myelinated axon markers based on segmented signal from confocal optic nerve cross-sectional images at Stage 58 (n= 10). Measurements show mean ± SD.

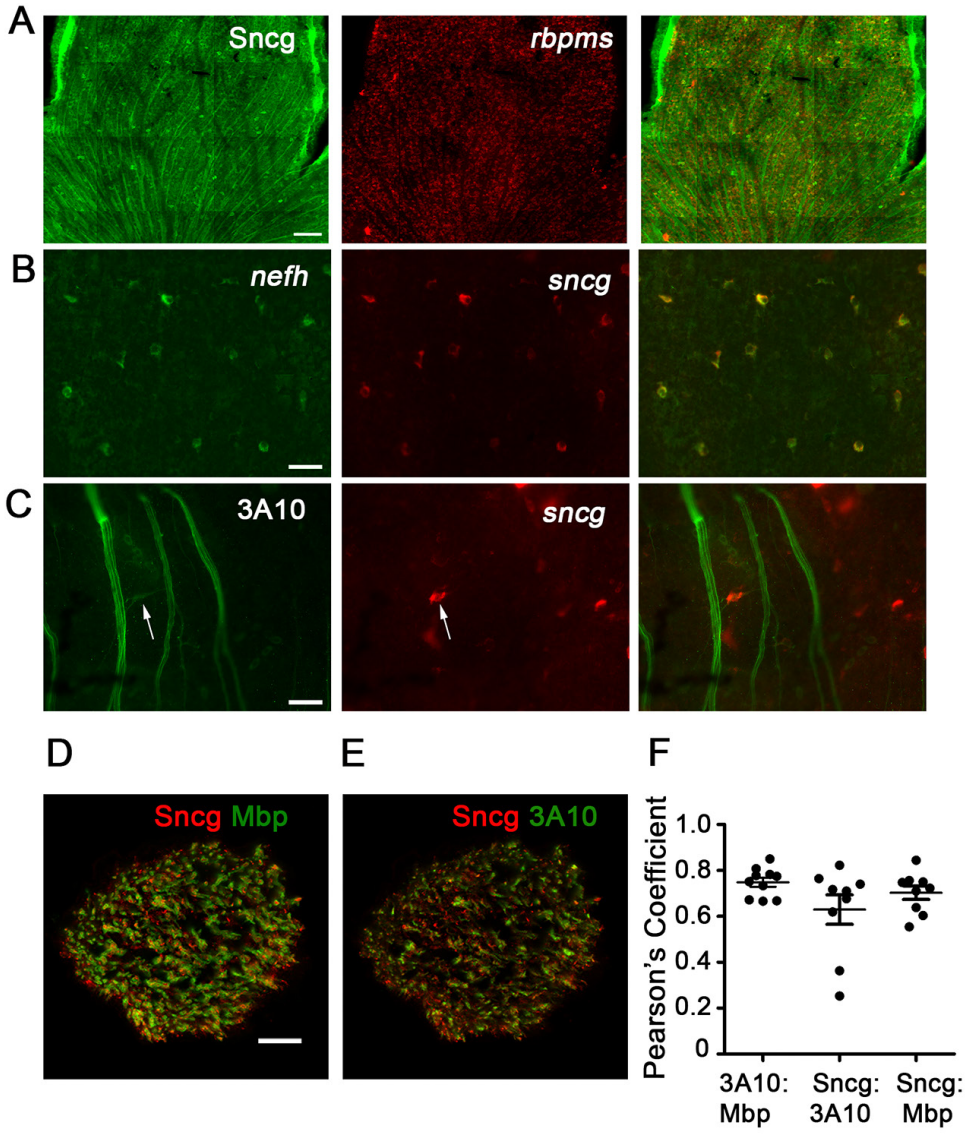
A
Sncg
rbpms
B
nefh
sncg
C
3A10
sncg
D
Sncg Mbp
E
Sncg 3A10
F
Pearson's Coefficient
1.0
0.8
0.6
0.4
0.2
0
3A10: Mbp
Sncg: 3A10
Sncg: Mbp

Figure 2.9 A population of myelinated axon derived material that is no longer associated with intact axons peaks during metamorphic climax

(A) Maximum intensity projections of confocal imaged optic nerve longitudinal cryo-sections at Stages 58, 62, and 66, immunolabeled with Mbp (blue), and large caliber axon marker 3A10 (white), with discrete Mbp structures not associated with axons (pseudo-colored red). Scale bar = 50 μm. **(B)** Maximum intensity projections of confocal imaged optic nerve longitudinal cryo-sections at Stages 58, 62, and 66 immunolabeled with Sncg (green), 3A10 (white), and Sncg labeled structures not associated with axons (pseudo-colored red). Scale bar = 50 μm. **(C)** Percentage of Mbp not co-localizing with 3A10 per optic nerve (n= 10) based on 3D reconstructions of confocal datasets. **(D)** Percentage of Sncg not co-localizing with 3A10 per optic nerve (n= 10) based on 3D reconstructions of confocal datasets. **(E)** Pearson's coefficient showing co-localization between Mbp and Sncg particles not associated with axons. All measurements show mean ± SD. *P < 0.05, **P < 0.01, and ***P < 0.001 by the Games-Howell test (C) or Tukey's test (D).

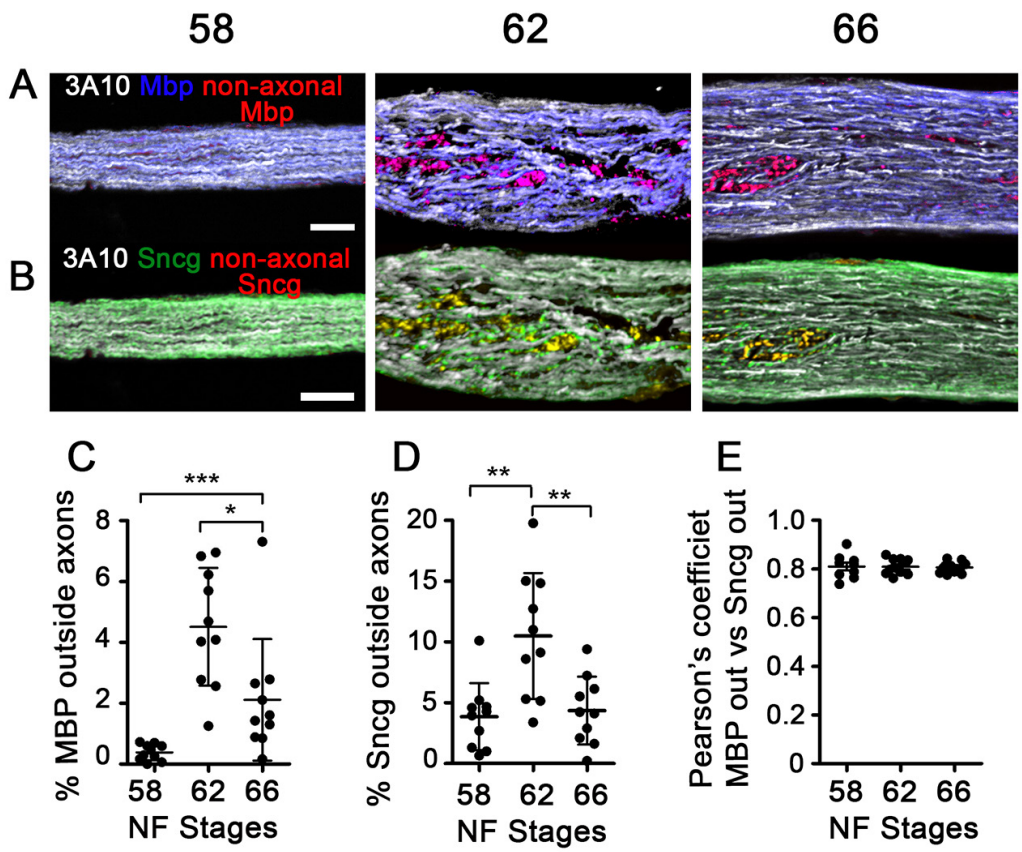
58
62
66
A
3A10 Mbp non-axonal Mbp
B
3A10 Sncg non-axonal Sncg
C
% MBP outside axons
***
*
0
2
4
6
8
58 62 66
NF Stages
D
% Sncg outside axons
**
**
0
5
10
15
20
58 62 66
NF Stages
E
Pearson's coefficiet MBP out vs Sncg out
0
0.2
0.4
0.6
0.8
1.0
58 62 66
NF Stages

Figure 2.10 Dystrophic axonal myelin is removed from segments and internalized during metamorphic optic nerve shortening

(A) Debris myelin intermediates observed in TEM micrographs from Stage 66 optic nerve cross-sections include myelin whorls associated with axons (i), debris myelin enwrapped by phagocyte lamellar processes (ii), and debris myelin within phagocyte soma (iii). Scale bar = 1 μm. **(B)** Percentage of debris intermediates in each category shown in (A). The transitional category represents myelin separated from axons but not fully internalized by a phagocyte. Metamorphic climax stages have a greater proportion of myelin in the process of being removed from axons. **(C)** Total area of debris myelin per optic nerve cross-section (n= 6). **(D)** Percentage of myelin in the form of debris per optic nerve cross-section (n= 6). B-D measurements obtained from traced TEM micrographs. All measurements show mean ± SD, with * $P < 0.05$ and ** $P < 0.01$ assessed by the Games-Howell test.

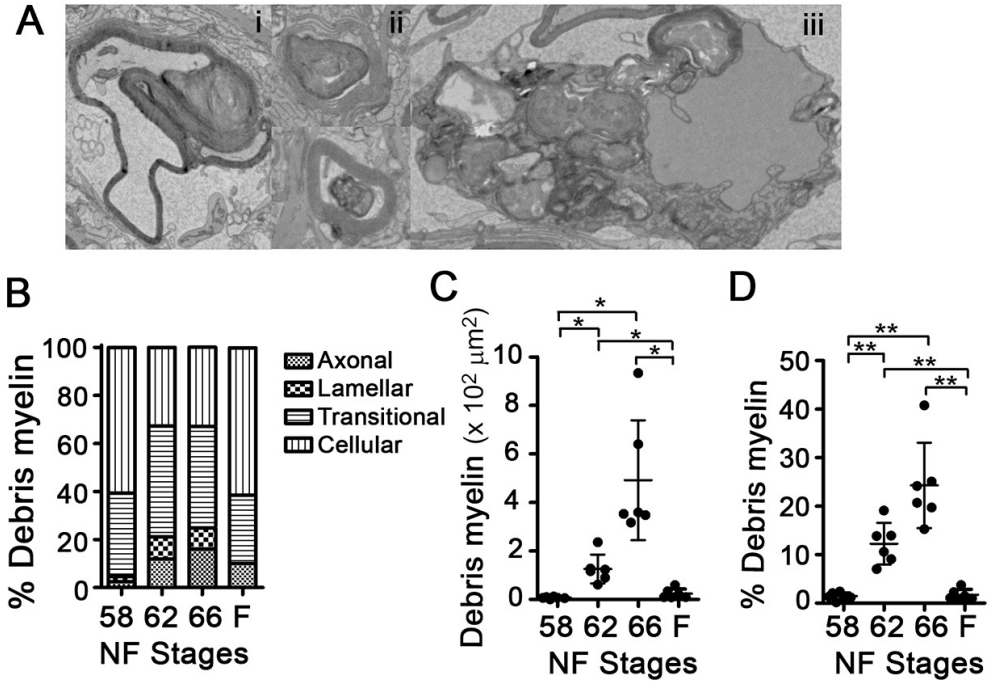

Figure 2.11 Regions of focal myelin detachments and protrusions are contacted by and selectively removed from axons by cellular processes from neighboring cells during optic nerve remodeling

(A) Phagocyte processes contact and enwrap focal myelin protrusions and detachments on remodeling metamorphic axons. Subsets of axon reconstructions from SBEM datasets for Stages 62 and 66 shown in Figures 2.7 (boxed regions), showing myelin (light and dark blue), axoplasm (yellow), focal peri-axonal space enlargements (white), and phagocyte processes (red). Scale bar = 5 µm. **(B)** Reconstruction based on SBEM data shows astrocyte (red) using lamellar processes (dark red) to internalize axonal material, containing both myelin (blue) and axoplasm (yellow). Scale bar = 5 µm.

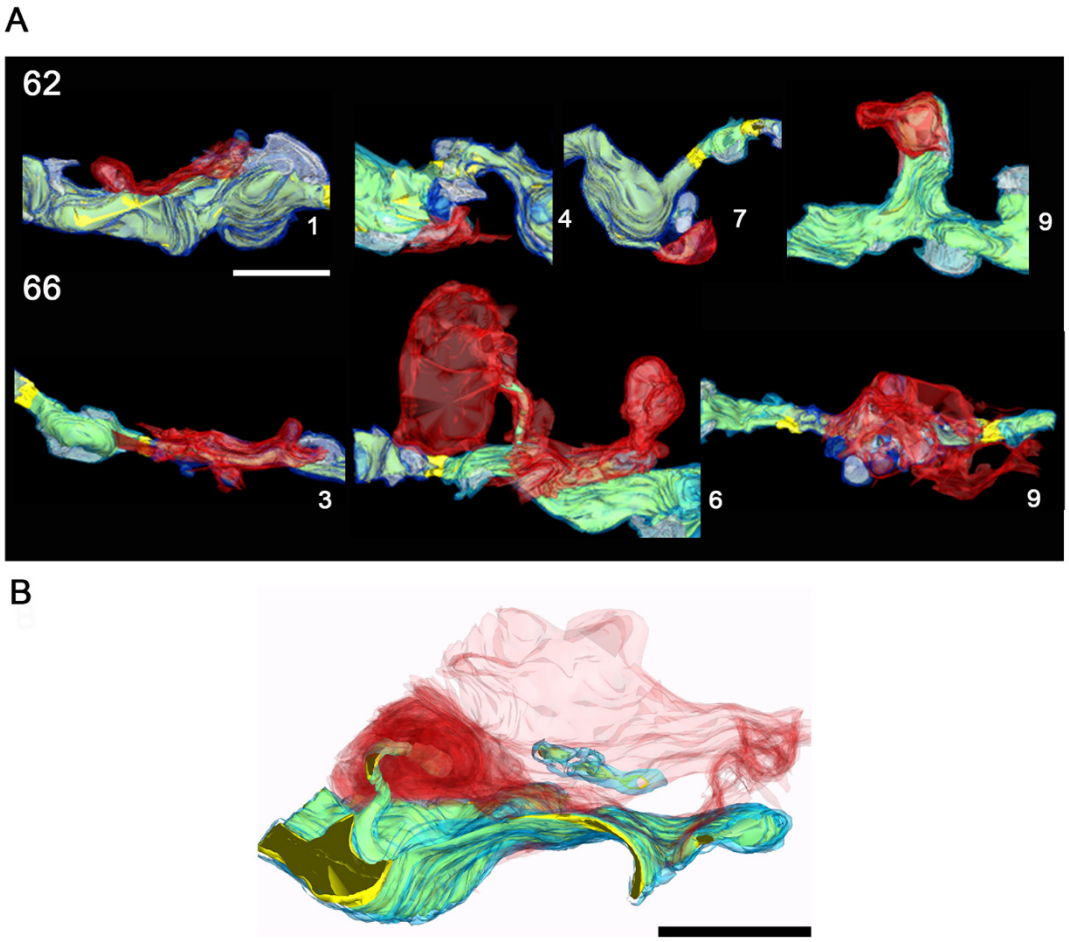

Figure 2.12 Internalized myelin accumulates and increases lipid droplet production in cells

(A) Mean area of individual debris myelin fragments averaged per optic nerve cross section (n= 6). **(B)** TEM micrograph showing myelin breakdown and lipid droplet accumulation within an astrocyte in Stage 66 optic nerve. Scale bar = 2 μm. **(C)** Mean area of individual lipid droplets averaged per optic nerve (n= 6). **(D)** Area of lipid droplets relative to total myelin area per optic nerve cross-section, measured from traced TEM micrographs in n= 6 optic nerves per stage showing mean ± SD. *P < 0.05 as assessed by the Games-Howell test. **(E)** Correlation between mean value per optic nerve (n= 6) of total area of lipid droplets and total area of debris myelin at Stage 66. R^2=0.92. Measurements show mean ± SD. Values for (A, C-E) derived from traced TEM micrographs. *P < 0.05, **P < 0.01, ***P < 0.001 by the Games-Howell test.

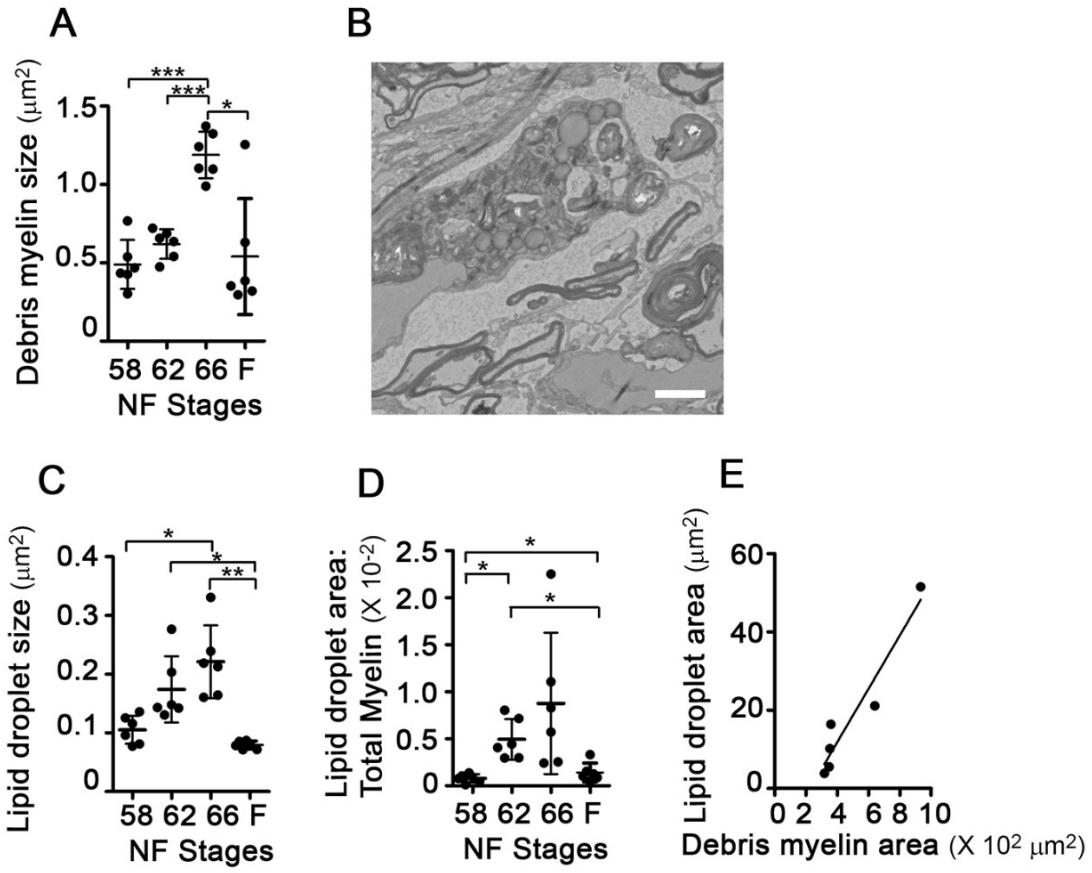

Chapter 3: Role of thyroid hormone in RGCs, oligodendrocytes, and astrocytes in the regulation of optic nerve remodeling

The structural remodeling of the head and accompanying shortening of the optic nerve represents one of many morphological changes that take place during the developmental period of metamorphosis in the frog, *Xenopus laevis*. These diverse remodeling events are all under the control of a single transcriptional regulator, thyroid hormone (Schreiber et al., 2001). In many cases, these morphological changes require the nervous system to respond by altering innervation patterns. In this way, the shortening of the optic nerve can be understood as the nervous system's response to the restructuring of the head. Since this remodeling event occurs during the developmental period of peak thyroid hormone levels, metamorphic climax, it appeared likely that, similar to other previously described remodeling events, optic nerve shortening is controlled by thyroid hormone.

Optic nerve shortening is mediated by thyroid hormone

I confirmed that optic nerve shortening is driven by thyroid hormone using a metamorphosis induction assay. Remodeling events that are under the control of thyroid hormone can be induced in pre-metamorphic animals, which have low circulating levels of thyroid hormone, through exposure to 3,5,3'-triiodothyronine (T3), the active metabolite of thyroid hormone (Tata, 2003). The pre-metamorphic Stage 54 *X. laevis* tadpoles, which have begun developing lower limbs but have otherwise experienced very little remodeling, were used. Stage 54 tadpoles treated with 20 nM T3 for 3 days remodeled their heads to become smaller in size and more triangular in shape (Figure 3.1A), which is consistent with the structural changes that take place during natural metamorphosis (Figure 2.1). In accordance with the head remodeling, the optic nerves from these animals shortened from 3.9 ± 0.2 mm to 2.9 ± 0.1 mm as a result of T3 treatment (Figure 3.1B). Furthermore, immunohistochemistry for myelin marker Mbp, axon

marker 3A10, and paranodal marker Neurofascin revealed that the internodal distance in the optic nerve had also decreased in length in these animals from 32.3 ± 7.7 μm at Stage 54 to 23.9 ± 3.7 μm following T3 treatment (Figure 3.1C). This shows that metamorphic optic nerve shortening is mediated by thyroid hormone, but does not indicate which cell type(s) drive this process and whether they are acting cell autonomously under the direct transcriptional control of thyroid hormone.

Transgenic expression of a thyroid hormone receptor dominant negative construct

Thyroid hormone shapes vertebrate development through a combination of transcriptional and non-genomic effects (Bassett et al., 2003), though amphibian metamorphic remodeling appears to be mediated almost exclusively through transcriptional regulation (Buchholz et al., 2004). Transcriptional regulation by thyroid hormone is mediated through its nuclear hormone receptors, which function as heterodimeric transcription factors. The binding of thyroid hormone or its active form, T3, to the C-terminus of its receptor leads to a conformational change resulting in the release of a repressor and recruitment of an activator, thereby facilitating gene transcription (Kim et al., 1999). Therefore, it is possible to interfere with metamorphic remodeling events in *X. laevis* through the use of transgenically expressed constructs that prevent the binding of thyroid hormone to its receptor(s).

A construct of thyroid hormone receptor α containing a C-terminal truncation, TRΔC, can bind to thyroid hormone regulated genes but is incapable of being activated by thyroid hormone, and thus works as a dominant negative (Marsh-Armstrong et al., 1999). The use of this dominant negative construct also circumvents the loss of gene repression that occurs with thyroid hormone receptor knockouts, which is the best explanation for the discrepancies between hypothyroid and thyroid hormone receptor knockout studies. Since there are two kinds of thyroid hormone receptor, α and β, often expressed within the same cell, the loss of gene repression through one kind can lead to the production of novel phenotypes when combined with the thyroid

hormone mediated gene expression by other receptor isoforms (Flamant and Samarut, 2003; Koibuchi et al., 2003). In contrast, the dominant negative thyroid hormone receptor α remains bound to thyroid hormone response genes, thus maintaining repression in the absence of hormone. In conjunction with the appropriate cell-type specific promoters, TRΔC can, in theory, be used to study any aspect of metamorphic remodeling. Indeed, this TRΔC construct has been effectively used to obtain mechanistic insight into other metamorphic remodeling events, such as limb growth, tail reabsorption, and intestinal, skin and pancreas remodeling (Buchholz et al., 2004; Schreiber et al., 2005; Schreiber et al., 2001). Therefore, I chose to use the TRΔC construct in an attempt to elucidate the contribution(s) of the major optic nerve cell types to metamorphic optic nerve remodeling.

Major cell types of the optic nerve can be targeted with cell-type specific promoters

The optic nerve is composed primarily of RGC axons and two populations of macroglia: oligodendrocytes and astrocytes. Small populations of other cell types such as immune system derived microglia, and oligodendrocyte precursor cells also exist, but their low numbers make them unlikely candidates as the primary drivers of optic nerve remodeling. Therefore, in order to address which cell type(s) are mediating metamorphic optic nerve remodeling, I placed the TRΔC construct under the control of cell-type specific promoters for RGCs, oligodendrocytes, and astrocytes. I used the zebrafish Islet2b (Isl2) promoter for expression in RGCs (Pittman et al., 2008), the mouse Myelin basic protein (Mbp) promoter for expression in oligodendrocytes (Kaya et al., 2012), and the *X. tropicalis* Brain lipid binding protein (Blbp) promoter for expression in astrocytes (Watson et al., 2012). In order to circumvent potential developmental defects or confounders, the expression of TRΔC in oligodendrocytes and astrocytes was performed in a tetracycline inducible manner using the reverse transactivator, rtTA2 (Das and Brown, 2004) and tetracycline operator (abbreviated TetOp). The inducible promoters are, however, somewhat leaky and thus less specific in their expression of the TRΔC transgene. As a dominant negative

transgene, TRΔC must be expressed at high levels to effectively block thyroid hormone mediated transcriptional activity, and since non-specific expression is much weaker than the cell-type specific expression, it is unlikely that the TRΔC transgene is functional in these off-target cell populations.

The cell-type specificity and potency of the TRΔC transgene to block thyroid hormone mediated gene expression was validated using *in situ* hybridization of a known thyroid hormone response gene. The open reading frame, *gene 12*, is strongly up-regulated in response to thyroid hormone in nearly all cell types examined (Berry et al., 1998). Since *gene 12* is sensitive to even low levels of thyroid hormone, I used a T3 induction assay on Stage 54 tadpoles. The tadpoles were treated with 3 nM T3 for 2 days in order to induce expression of the most sensitive thyroid hormone responsive genes without inducing the widespread morphological changes that occur with exposure to high concentrations of T3. This allowed me to test the ability of the TRΔC transgene to directly block thyroid hormone mediated transcription, as opposed to a downstream effect of remodeling. Animals expressing the TRΔC transgene under the tetracycline inducible promoters, Mbp and Blbp, received brain injections of 50 mg/L doxycycline 24 hours prior to T3 exposure and had rearing solution supplemented with 50 mg/L doxycycline for the duration of the experiment. Eyes and optic nerves were obtained from the animals at the conclusion of the experiment for gene expression analysis via quantitative *in situ* hybridization.

Expression of TRΔC transgene in RGCs prevents thyroid hormone mediated gene up-regulation

Following T3 induction, the thyroid hormone response gene, *gene 12* was up-regulated 7 fold in the retina (Figure 3.2A-B) and 10 fold specifically in RGCs (Figure 3.2C), as identified by the expression of *rbpms* (Figure 3.2A). Expression of the TRΔC transgene in RGCs severely blunted the up-regulation of *gene 12* specifically in RGCs (Figure 3.2C), as the up-regulation of gene 12 in non-RGCs was not affected in the retinas of these animals (Figure 3.2D). Therefore,

the Isl2: TRΔC transgene effectively blocks thyroid hormone mediated gene transcription specifically in RGCs.

Expression of TRΔC transgene in optic nerve prevents thyroid hormone mediated gene up-regulation in a cell-type specific manner

In the optic nerve, *gene 12* was up-regulated approximately 100 fold following T3 induction (Figure 3.2E-G). Although *gene 12* is up-regulated in nearly all cells in response to thyroid hormone, *gene 12* expression appears to be unaffected in oligodendrocytes, as identified by the expression of *plp*. *Gene 12* was found to be absent or weakly expressed in oligodendrocytes in the optic nerve (Figure 3.2E), and thus could be used to address specificity but not functionality of the TRΔC transgene in oligodendrocytes. The overall expression of *gene 12* in the optic nerves from animals expressing the TRΔC transgene under the Mbp promoter was comparable to the level of expression found in the nerves of wild-type animals treated with T3 (Figure 3.2G), indicating that expression of this transgene does not block thyroid hormone mediated transcription in the other cell types of the optic nerve. In contrast, *gene12* expression was severely blunted in the optic nerves from animals expressing the TRΔC transgene in astrocytes (using the Blbp promoter), such that the nerves resemble those from untreated animals (Figure 3.2F).

Since oligodendrocytes do no strongly express *gene 12*, and the majority of cells in the optic nerve are astrocytes, the widespread blunting of *gene 12* expression in the nerve is not an indication of non-specificity, but rather strong functionality of the transgene. Based on the strength and specificity of the Mbp promoter (Kaya et al., 2012) and potency of the TRΔC transgene under all promoters tested here and previously (Buchholz et al., 2003; Das et al., 2002; Marsh-Armstrong et al., 2004; Marsh-Armstrong et al., 1999; Nakajima and Yaoita, 2003; Schreiber and Brown, 2003), the TRΔC transgene expressed under the Mbp promoter likely blunts thyroid hormone mediated transcription in oligodendrocytes at a level comparable to those

shown here for the Isl2 and Blbp promoters. Overall, the *gene 12* in situ hybridization analysis indicates that the expression of the TRΔC transgene is sufficient to block thyroid hormone mediated transcription in the major cell types of the optic nerve.

Electron microscopy based quantitative analysis of the optic nerve during metamorphosis in animals expressing the TRΔC transgene

An electron microscopy based quantitative analysis on the optic nerves of animals expressing the TRΔC transgene in RGCs, oligodendrocytes, or astrocytes during metamorphic optic nerve shortening was performed to determine the contribution of these cell types to the remodeling process. The electron microscopy study was similar to the one performed on wild-type animals described in Chapter 2 with a few minor differences. In this study only the metamorphic time-points, Stages 62 and 66, were examined since this is the period of peak thyroid hormone levels and related morphological change. Furthermore, the expression of the TRΔC transgene was not induced in the animals in which the transgene was driven by the Mbp and Blbp promoters in a tetracycline inducible manner until Stage 58 to ensure that any changes seen in the optic nerves from these animals could be attributed to the loss of thyroid hormone mediated activity during remodeling and not a residual effect from an earlier point in development.

The optic nerves from the TRΔC expressing animals were compared to nerves from a control set of animals comprised of a combination of two lines of animals expressing fluorescent proteins and should have no effect on remodeling or any other function of the optic nerve cells. Since the *X. laevis* frogs used in this study are an out-bred population, a high degree of natural variation across animals is expected, although the progeny derived from the same founder will of course be most similar to each other. Ideally, comparisons would be made between siblings who differ on their expression of the transgene, however, given the time intensive nature of manual tracing, having separate control groups for each transgene was not practical. Therefore, in order

to circumvent the potential problem of natural variation in the measured features amongst the transgenic lines that is unrelated to the transgene itself, two different transgenic controls were used. This resulted in the metrics spanning a wider region of the phenotypic space, and thereby effectively increased the variability of the control group. Furthermore, the transgenic lines were compared to one another, although only significant comparisons between transgenic and control lines are shown.

Optic nerve shortening is delayed but not prevented by cell-type specific expression of TRΔC transgene

The analysis of the metamorphic optic nerves from the transgenic lines expressing the TRΔC transgene revealed that none of the cell types investigated is directly responsible for the shortening of the optic nerve in a thyroid hormone dependent manner. The expression of the TRΔC transgene in each of the cell types tested did result in these animals having significantly longer optic nerves at metamorphic climax, Stage 62 (Figure 3.3A). However, this appears to be due to a delay rather than an inhibition of shortening since by the end of metamorphosis, Stage 66, the nerve lengths were generally comparable for all groups (Figure 3.3B). The optic nerves from animals expressing the TRΔC transgene under the Mbp promoter remained significantly longer at 2.0 ± 0.2 mm compared to controls which were 1.6 ± 0.3 mm at this later stage, but they had still shortened between Stages 62 and 66. Therefore, nerve shortening does not occur in direct response to thyroid hormone signaling in any one of these cell types alone. The delay seen in all the transgenic lines suggests that proper shortening requires the coordinated actions of several cell populations in the optic nerve, though it appears likely that thyroid hormone activity in some cell types is more influential than others in this process. Furthermore, it is likely that the shortening itself is most directly controlled by a different cell type, particularly ones which might lie outside of the nervous system altogether, such as the optic nerve sheath and connective tissue of the head which also remodel during metamorphic climax.

The induction of pre-metamorphic animals with T3 indicated that both nerve shortening and myelin segment shortening occur in response to thyroid hormone exposure. However, since segment shortening has not been shown to occur outside of whole nerve shortening, it is unclear whether segment shortening is directly mediated by thyroid hormone or it is an indirect effect of thyroid hormone mediated optic nerve shortening. An analysis of internodal distance was carried out on longitudinal optic nerve cryo-sections from animals expressing the TRΔC transgene, compared to control animals, at metamorphic climax, Stage 62. Internodal distance was determined using maximum intensity projections of confocal imaged optic nerves following immunohistochemistry with the paranodal marker Neurofascin in conjunction with the myelin marker Mbp and myelinated axon marker 3A10 (Figure 3.3C). In this case, the control nerves were derived from transgenic animals containing an inducible form of the transgene, but which had not been induced with doxycycline. The internodal distances in optic nerves from animals expressing the TRΔC transgene were highly similar to those found in control nerves (Figure 3.3C). Once again, the internodal distances from the animals expressing the TRΔC transgene under the Mbp promoter (32. 5 ± 6.0 μm) were slightly longer than control (27.1 ± 5.5 μm), which is consistent with these animals having longer nerves, or a delay in shortening. This further supports the notion that myelin segment shortening is coupled to optic nerve shortening, and thus is not solely a function of direct thyroid hormone mediated signaling in any of the cell types examined.

Expression of TRΔC transgene does not induce cell death or an immune response in the optic nerve

In order to determine whether the expression of the TRΔC transgene affected the viability of axons or cells in the optic nerve, an analysis was performed on the optic nerves from these animals using the cell death and degeneration marker cleaved-caspase-3. An increase in axon or cell death in the optic nerve would be expected to result in an inflammatory immune response, as

indicated by an increase in the presence of immune cells such as macrophages or microglia in the nerve. I performed immunohistochemistry on longitudinal optic nerve cryo-sections for cleaved-caspase-3 and the microglia/macrophage marker IB4-lectin-FITC. Optic nerves from animals expressing the TRΔC transgene were compared to nerves from siblings that did not express the transgene. The optic nerves were quantified using a segmentation based script written by my advisor. None of the transgenes showed a significant increase in the amount of cell/axonal death (Figure 3.4A-F), however, there was an increase in the number of microglia/macrophages per unit area (Figure 3.4G-L) for animals expressing the TRΔC transgene in RGCs in the optic nerve during metamorphic climax. Therefore, axon health or viability is likely affected by the loss of TRΔC mediated signaling in RGCs. But overall, there does not appear to be a major pathological response to the expression of the TRΔC transgene.

Loss of thyroid hormone mediated transcription leads to a decrease in number of myelinated axons in optic nerve

The quantitative analysis of the TEM micrographs from the optic nerves from animals expressing the TRΔC transgene in RGCs revealed that these nerves had approximately 30% fewer myelinated axons. The optic nerves from the Isl2: GFP-TRΔC (abbreviated as Isl2: TRΔC) animals had 509 ± 65 and 585 ± 124 axons compared to control nerves with 746 ± 215 and 910 ± 179 axons at Stages 62 and 66, respectively (Figure 3.5A-B). Decreases in numbers of myelinated axons in the optic nerve have been previously noted in studies from hypothyroid and thyroid hormone receptor mutant mouse studies (Baas et al., 2002; Leung et al., 1992). This result, however, has generally been attributed to a loss or defect in myelination, but they involved global, not cell specific loss of thyroid hormone activity. The decreased number of myelinated axons could indicate a specific deficit in new myelination during metamorphosis, or could have developed as a result of having a smaller pool of RGC axons available for myelination or most likely some combination of both. Retinas from animals expressing the Isl2: TRΔC transgene at a

stage prior to metamorphic climax when thyroid hormone levels are low, Stage 56, quantified for expression of the RGC marker, *rbpms*, were found to be indistinguishable from wild-type retinas (Figure 3.5C-D). In contrast, retinas from Isl2: TRΔC expressing animals during metamorphic climax, Stage 62, contained, on average, approximately 20% fewer *rbpms* labeled RGCs, as they had only 16,900 ± 430 RGCs compared to 21,000 ± 670 RGCs in wild-type retinas (Figure 3.5E-F). This indicates that the TRΔC transgene in RGCs only produces a phenotype when thyroid hormone levels are elevated, as occurs during metamorphic climax.

The decreased number of RGCs could result from a decrease in cell proliferation or an increase in cell death. Quantification of terminal deoxynucleotidyl transferase dUTP nick end labeled (TUNEL) retinas showed a nearly two-fold increase in TUNEL positive cells at metamorphic climax in retinas from animals expressing the Isl2: TRΔC transgene. TUNEL labeling is an indication of DNA fragmentation, which usually occurs in the context of apoptotic cell death. Therefore, the increase in TUNEL positive cells from 0.000016 ± 0.000008 cells per unit area in control retinas to 0.000028 ± 0.00001 cells per unit area in Isl2: TRΔC retinas (Figure 3.5G-H) suggests an increase in the death of RGCs, and that thyroid hormone is important for the survival of the RGCs during metamorphosis. The increase in cell death would also account for the decreased number of RGCs in these retinas. The increased presence of microglia in the optic nerves (Figure 3.4G-H) from these animals then could be due to the reduced viability of RGCs and their associated axons. These findings further suggest that the decreased number of myelinated axons in the optic nerves from the Isl2: TRΔC expressing animals is related to a decrease in the overall number of RGC axons in the optic nerve, although an additional deficit in the ability of RGC axons to recruit oligodendrocytes to initiate myelination cannot be ruled out.

The optic nerves from the animals expressing the TRΔC transgene in RGCs also had less total myelin, as they contained an area of 722 ± 299 μm^2 per cross-section, compared to an area of 1050 ± 392 μm^2 per cross-section in control nerves (Figure 3.5I). This likely occurs as a natural extension of these animals having less myelinated axons in their optic nerves.

Furthermore, these optic nerves also have approximately one-quarter less debris myelin. The area of debris per cross-section is only 151 ± 94 μm^2 in Isl2: TRΔC optic nerves compared to 518 ± 287 μm^2 in control nerves (Figure 3.5J). This supports the view that debris myelin is derived from remodeling axons rather than degenerating axons, such that less debris is generated when there are less myelinated axons to be shortened.

Expression of TRΔC transgene in RGCs produced a severe phenotype in a subset of animals.

The decrease in the number of myelinated axons and overall myelin levels in the optic nerves from animals expressing the TRΔC transgene in RGCs were consistent across all animals examined at both metamorphic stages. In general, the optic nerves obtained from Isl2: TRΔC animals at Stage 62 were similar to one another on all metrics. In contrast, at Stage 66 there was a clear dichotomy in the optic nerves on a subset of metrics. These differences were likely due to variation in the expression of the transgene in the progeny of the founder lines. A subsequent characterization of F1 progeny revealed considerable differences in transgene expression, suggesting potential transgene rearrangement. All of the animals used for this study were screened for high transgene expression in the eye during early development, through the use of a fluorescent reporter, but individual genomic differences between animals may have affected the transgene later in development.

Interestingly, the axons themselves did not differ between the two groups (Figure 3.6A), but rather the myelin sheaths surrounding the axons. In one group of animals, there was little space between the axons or between the axon and myelin membranes, while in the other group there were large intramyelinic vacuoles and vast expansion of the peri-axonal space (Figure 3.6B-C). The latter phenotype may have arisen due to an excessive loss of axo-glial adhesive attachments during metamorphic remodeling. It is possible that severe disruption of thyroid hormone mediated transcriptional activity in RGC axons, as achieved through very high

expression of the TRΔC transgene, negatively affected the expression of genes needed to maintain the adhesive complexes bridging axon and myelin membranes. Therefore, as some attachments are disrupted in the course of axon shortening, the nearby attachments, which are normally maintained, are weak and thus readily lost as well, leading to the unraveling of myelin from the axon. In response to the impairment of thyroid hormone receptor activity in RGCs, the presence of two distinct groups is not unprecedented. Accelerated degeneration of RGCs was found in retinas of a subset of rodents lacking all thyroid hormone receptor isoforms (Baas et al., 2002). This study had also been unable to determine the exact underlying cause, and similarly attributed the disparity to genetic variation.

Optic nerves from animals expressing the TRΔC transgene in oligodendrocytes have thinner myelin sheaths and less overall myelin

The expression of the TRΔC transgene in oligodendrocytes also led to myelin related changes in the optic nerve, as might be expected from interfering with myelin producing cells. The role of thyroid hormone in myelination is one of the best studied effects of thyroid hormone in the central nervous system. In mammals, thyroid hormone has been demonstrated to increase the production of mature myelinating oligodendrocytes during development by promoting the differentiation of OPCs and expression of myelin associated proteins (Billon et al., 2002; Farsetti et al., 1991). The effects of thyroid hormone, however, are highly dependent on the period of development. Animals lacking thyroid hormone in their central nervous system during the peak period of myelination will experience a delay in myelination and decrease in overall levels of myelin (Rodriguez-Pena et al., 1993; Zoeller and Rovet, 2004). Therefore, the loss of thyroid hormone in oligodendrocytes exclusively during the period of metamorphic climax might be expected to produce delays in myelin remodeling and myelination. Consistent with these animals experiencing a delay and/or reduction in optic nerve shortening during metamorphosis; morphologically, their optic nerves more closely resembled those found in pre-metamorphic

animals. The myelinated axon sizes in the optic nerves of animals expressing Mbp: rtTA/TetOp: GFP-TRΔC (abbreviated Mbp: TRΔC) of 0.52 ± 0.06 μm^2 at Stage 62 and 0.70 ± 0.12 μm^2 at Stage 66 (Figure 3.7A-B) were reminiscent of Stage 58 axons with an average area of 0.68 ± 0.02 μm^2 (Figure 2.3A). These axons were thus much smaller than those found in control optic nerves with areas of 0.77 ± 0.20 μm^2 and 0.92 ± 0.21 μm^2 at Stages 62 and 66, respectively. Additionally, the myelin sheaths surrounding these axons were correspondingly smaller such that the area of myelin per axon was smaller (3.7C-D) and there was a rightward shift in the distribution of G'-ratios (Figure 3.7E), indicative of thinner myelin sheaths in these optic nerves. Consequently, the total area of axonal myelin per cross-section in the Mbp: TRΔC optic nerves at Stage 66, 473 ± 148 μm^2, was significantly less than the area of 761 ±214 μm^2 in control nerves (Figure 3.7F)

Since the cross-sectional growth of axons is generally associated with the addition of myelin wraps around the axon, the decreased size of the myelinated axons in these nerves could be due to a deficit in myelin production by the oligodendrocytes. Alternatively, there could be a decrease in the production of the oligodendrocytes themselves, via a decrease in OPC differentiation. However, *in situ* hybridization for *pdgfrα* and *plp* on longitudinal optic nerve cryo-sections at metamorphic climax (Figure 3.7H) revealed that neither the density of OPCs (Figure 3.7I) nor mature oligodendrocytes (Figure 3.7J) was altered in the optic nerves from animals expressing the Mbp: TRΔC transgene. This suggests that the differentiation of OPCs into myelinating oligodendrocytes was not affected. Additionally, although the axons were smaller, the amount of myelinated axons in these nerves was comparable to the optic nerves from control animals (Figure 3.7G). Since individual oligodendrocytes are thought to have a limit to the amount of myelin they can produce and maintain, the number of segments they produce is likely related to the overall size of the individual segments. Therefore, oligodendrocytes could produce many thin segments or fewer thicker ones. If the level of myelin-associated proteins such as Mbp and Plp is too low due to a lack of thyroid hormone mediated transcription, the oligodendrocytes

would be compromised in their ability to produce new myelin. Therefore, if the myelin producing capacity of each oligodendrocyte in the Mbp: TRΔC optic nerves was limited, then each oligodendrocyte might compensate by producing thinner segments. In this way, myelination could proceed at a normal rate during metamorphosis. The decreased size, but normal numbers of myelinated axons suggest that the lack of thyroid hormone mediated transcription in the oligodendrocytes during metamorphosis reduces overall levels of myelin but does not necessarily lead to a loss of myelination.

Since the optic nerves from the Mbp: TRΔC expressing animals did not shorten to the same magnitude as wild-type animals, the myelinated axons would also be expected to experience a delay or reduction in remodeling. In most cases, the smaller axon size found in the Mbp: TRΔC optic nerves would be an indication of impairment in growth and/or myelination. However, since metamorphosis is accompanied by a transient enlargement of the optic nerve and its associated axons, the smaller axons size could be due to a lack of this shortening-related axonal hypertrophy. If the pre-existing axons remain longer and thinner, their associated myelin sheaths would also be less affected.

The increased internodal distance in these nerves during metamorphic climax suggests that myelin segments remain longer and thus are unlikely to develop as many regions of dystrophic myelin, such that less 'excess' myelin would need to be removed from these segments. Indeed, the myelinated axons from the Mbp: TRΔC expressing optic nerves have a decrease in the amount of focal axo-glial detachments based on quantification of the associated peri-axonal space enlargements in cross-sectional TEM micrographs. The Mbp: TRΔC optic nerve cross-sections had 0.18 ±0.06 and 0.16 ± 0.04 myelin detachments per axon compared to 0.32 ± 0.09 and 0.30 ± 0.09 detachments per axon in control nerves at Stages 62 and 66, respectively (Figure 3.7K-L). Additionally, the area of enlarged peri-axonal space associated with the detachment at Stage 66 is, at 43.4 ± 15.6 μm^2, also smaller than the peri-axonal space area of 108.2 ± 37.3 μm^2 in control nerves (Figure 3.7M). Furthermore, the amount of debris myelin per optic nerve cross

section is decreased from 518 ± 287 μm^2 in control nerves to 210 ± 138 μm^2 in optic nerves expressing the Mbp: TRΔC transgene (Figure 3.7N). This result is likely related to the decreased amount of axonal myelin, such that the area of myelin contained in a detachment or evulsion, and thus targeted for removal, would be less for axons with smaller thinner myelin sheaths.

Expression of the TRΔC transgene in astrocytes leads to an impairment in the remodeling related removal of excess myelin from axons

In contrast to the well-studied effect of thyroid hormone on oligodendrocytes and myelination, the effect of thyroid hormone on astrocytes is less well understood. In regards to thyroid hormone the primary role for astrocytes has historically been its conversion of thyroid hormone (T4) to its active form, T3, through the enzyme, deiodinase 2 (Anderson, 2001). This enzyme is not expressed in neurons, therefore thyroid hormone mediated transcription in neurons is dependent upon the conversion of thyroid hormone and release of active T3 by astrocytes. Whether astrocytes themselves were responsive to thyroid hormone had been controversial, yet recent evidence suggests that they are directly affected primarily through thyroid hormone receptor α (Morte et al., 2004). Similar to oligodendrocytes, the proliferation and maturation of astrocytes appears to be sensitive to thyroid hormone, at least during some periods of development (Mohacsik et al., 2011).

The use of the Blbp promoter to drive TRΔC transgene expression in astrocytes could also potentially influence other cell types since Blbp is also found in progenitor cell populations such as radial glia. However, the use of the tetracycline inducible system allows expression of the transgene to be confined to the period of metamorphic remodeling, and thus avoid any potentially critical periods of early development. Nevertheless, it is possible that some thyroid hormone receptor mediated effects of thyroid hormone in astrocytes also impact other cell types, including neurons and oligodendrocytes. However, since the major phenotype was unique in relation to the

other cell types examined, it suggests that off-target effects of the TRΔC transgene were likely minimal.

Surprisingly, the optic nerves from animals expressing the TRΔC transgene in astrocytes displayed phenotypes indicative of a deficit in the removal of excess myelin from remodeling axons during late metamorphosis. Early during the remodeling process, at Stage 62, the axons in the optic nerves from animals expressing Blbp: rtTA/TetOp: GFP-TRΔC (abbreviated Blbp: TRΔC) were largely similar to nerves from control animals in terms of numbers of myelinated axons (Figure 3.8A), axon size (Figure 3.8B), and myelin per axon (Figure 3.8C). There appeared to be, however, a delay in myelin remodeling and removal as indicated by a decreased number of focal myelin detachments (Figure 3.8D). By Stage 66, there was a clear distinction between optic nerves from Blbp: TRΔC expressing and control animals. Interestingly, the number of myelinated axons in the optic nerve remained flat during this time with an average of 687 ± 122 axons at Stage 62 and 672 ± 160 axons at Stage 66 (Figure 3.8E), suggesting there may be a deficit in new myelination. Since Blbp expressing astrocytes have been implicated in promoting the differentiation of OPCs, this may explain the effect on myelination. At Stage 62, these nerves have a trend toward a decreased ratio of oligodendrocytes/OPCs based on expression of *plp* and *pdgfrα* (Figure 3.8H), however, this could also be explained by expression of the transgene in progenitor cells, and thus may be an off-target effect not directly mediated by the action of thyroid hormone in astrocytes.

Most strikingly, there was an excess of myelin on the existing axons, as the ratio of myelin: axoplasm was elevated from 0.9 ± 0.2 in control nerves to 1.3 ± 0.3 in optic nerves from animals expressing Blbp: TRΔC (Figure 3.8F). This was accompanied by an increase in size of the focal detachments (Figure 3.8G). Together, these results suggest that optic nerve astrocytes also contribute to myelin remodeling during metamorphic optic nerve shortening and places them as the potential phagocytic cell population responsible for removing excess myelin from shortening axons.

The mechanism by which thyroid hormone activity in astrocytes contributes to their phagocytosis of myelin remains unclear. In metamorphic pruning in *Drosophila*, expression of the phagocytic receptor Draper is induced in the phagocytic glia in response to the equivalent insect metamorphic hormone, ecdysone (Awasaki et al., 2006) (Tasdemir-Yilmaz and Freeman, 2014). In *X. laevis*, expression of some phagocytic receptor genes, including *megf10, itgB3*, and *lrp1*, appear to be slightly reduced in optic nerve astrocytes expressing the TRΔC transgene (Figure 3.8I). However, whether thyroid hormone directly affects the transcriptional activity of these genes in *X. laevis* astrocytes remains unknown.

Similar to its role in mammals, thyroid hormone transcriptional activity may also influence the abundance of mature astrocytes, such that a smaller number of astrocytes are interacting with axons and removing myelin. However, a metric of the total number of myelin interacting and phagocytically active astrocytes cannot reliably be attained from fixed preparations and would require live imaging of this dynamic process at a resolution that is not currently available. Ultimately, the role of thyroid hormone in myelin removal by astrocytes cannot be adequately addressed without an assessment of which genes are transcriptionally regulated by thyroid hormone in optic nerve astrocytes during metamorphic climax.

Overall, the study involving the expression of the thyroid hormone receptor dominant negative transgene, TRΔC, under cell-specific promoters in the optic nerve revealed that metamorphic optic nerve remodeling involves the coordinated activities of multiple cell types. No single cell type was found to control the process, but rather, all three of the major optic nerve cell types: RGCs, oligodendrocytes and astrocytes contribute to remodeling in a thyroid hormone dependent manner. The major roles of thyroid hormone during remodeling are in the myelination of axons and the modulation of the amount of myelin on axons, through control of myelin sheath thickness by oligodendrocytes and removal of excess myelin by astrocytes.

Figure 3.1 Optic nerve shortening is driven by thyroid hormone

(A) Representative image showing induced metamorphic remodeling of the head in a wild-type Stage 54 animal after treatment with exogenous 3,5,3′-′triiodothyronine (T3) for 3 days. Scale bar = 5 mm **(B)** Optic nerve length of Stage 54 tadpoles treated with T3 compared to untreated animals (n= 5 nerves). **P < 0.01 by Student's t-test. **(C)** Internodal distances of myelin segments measured from confocal images of longitudinal cryo-sections immunolabeled with 3A10 and Neurofascin from control and T3-treated Stage 54 animals. Measurements from 32 axons derived from 4 optic nerves per condition. All measurements show mean ±SD. ***P < 0.001 by Student's t-test with Welch's correction.

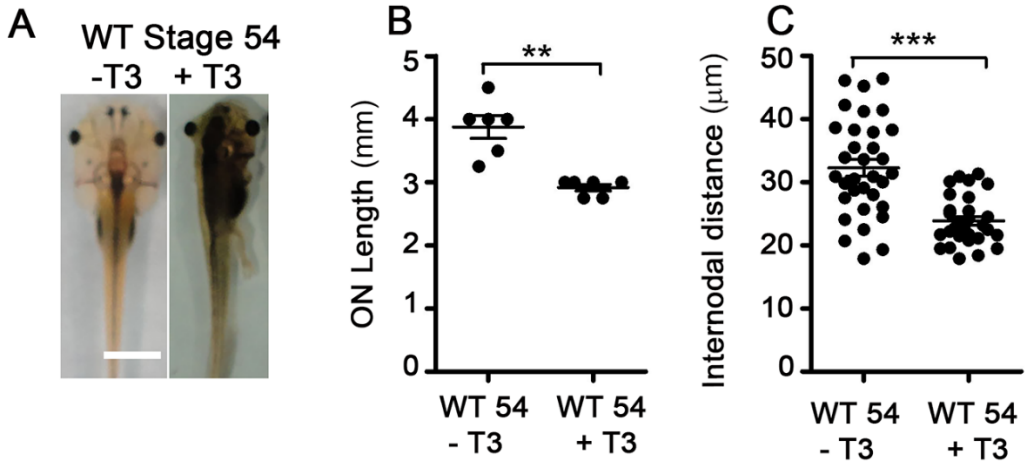

Figure 3.2 The TRΔC transgene blocks thyroid hormone mediated transcription in a cell-type specific manner

(A) T3-induced *gene 12* mRNA (red) is broadly up-regulated in retina by exogenous T3, but in Isl2: GFP-TRΔC animals the up-regulation is specifically inhibited in RGCs, which were identified by *rbpms* mRNA (green) expression. Nuclei labeled with Dapi (blue). ONL= Outer nuclear layer, INL= Inner nuclear layer, GCL= Retinal ganglion cell layer. Scale bar = 50 μm. **(B)** *Gene 12* mRNA signal mean fluorescence intensity in all cells of retina (n= 5 retinas). **P < 0.01 and ***P < 0.001 by the Games-Howell test. **(C)** *Gene 12* mRNA signal mean fluorescence intensity in RGCs only (n= 5 retinas). ***P < 0.001 by Tukey's test. **(D)** Gene 12 mRNA signal mean fluorescence intensity in all cells of retina except RGCs (n= 5 retinas). **P < 0.01 and ***P < 0.001 by the Games-Howell test. **(E)** T3-induced *gene 12* mRNA (red) up-regulation by T3 in the optic nerve, which is primarily in astrocytes, is blunted in the Blbp: rtTA/TetOp: GFP-TRΔC ON. In Mbp: rtTA/TetOp: GFP-TRΔC animals, total *gene 12* expression is not inhibited, since mature oligodendrocytes, identified by expression of *plp* (green), only weakly express *gene 12*. Scale bar = 50 μm. **(F)** Up-regulation of gene 12 mRNA (red) in the optic nerve by T3 is primarily in Blbp immunolabeled astrocytes (green). Scale bar = 50 μm. **(G)** *Gene 12* mRNA signal mean fluorescence intensity in all cells of optic nerve (n= 6, 8, or 5 ON in WT, Blbp or Mbp, respectively). *P < 0.05 and **P < 0.01 by the Games-Howell test.

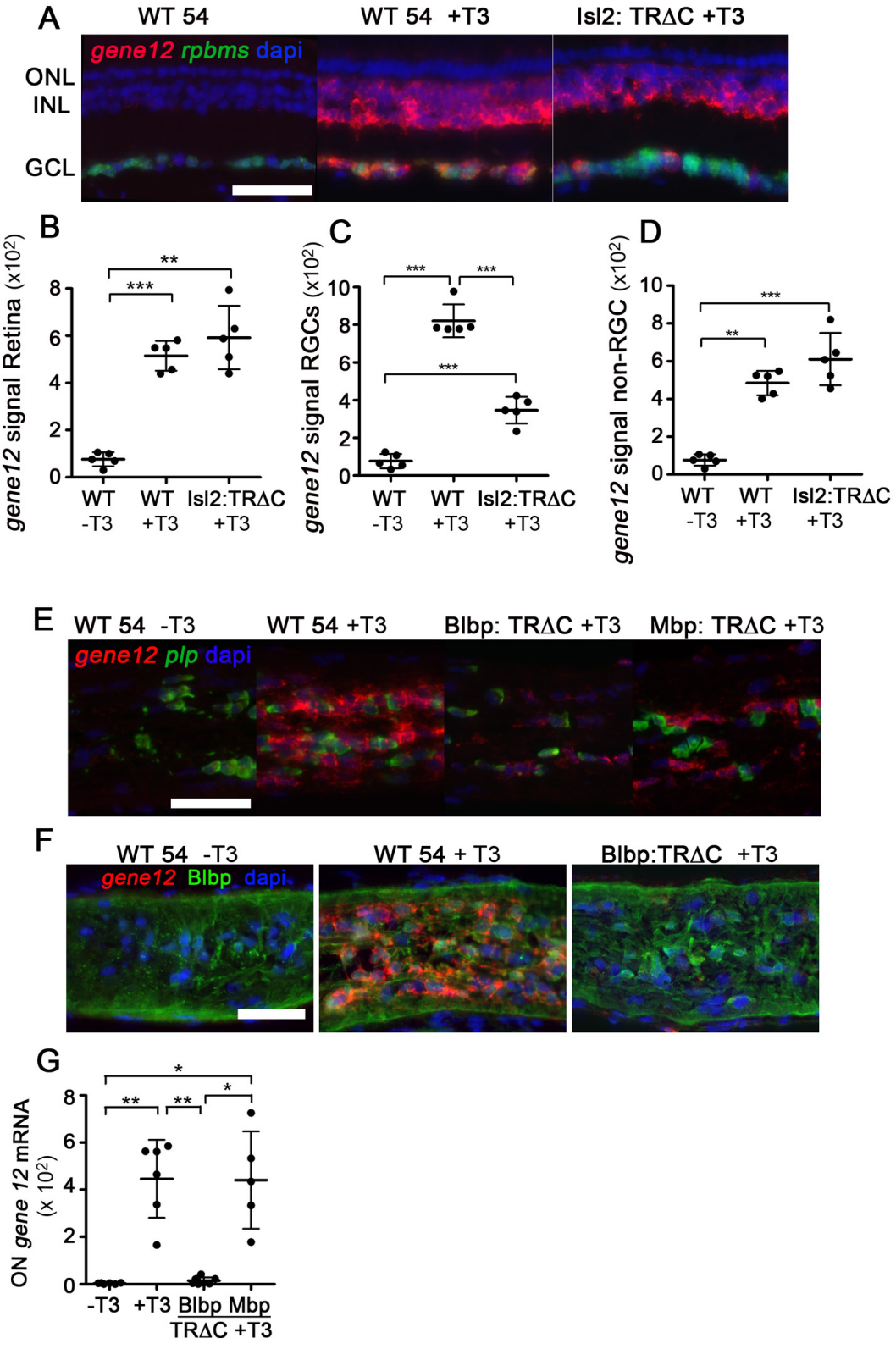
A
WT 54
WT 54 +T3
Isl2: TRΔC +T3
gene12 rpbms dapi
ONL
INL
GCL
B
gene12 signal Retina (x10²)
C
gene12 signal RGCs (x10²)
D
gene12 signal non-RGC (x10²)
WT -T3
WT +T3
Isl2:TRΔC +T3
E
WT 54 -T3
WT 54 +T3
Blbp: TRΔC +T3
Mbp: TRΔC +T3
gene12 plp dapi
F
WT 54 -T3
WT 54 + T3
Blbp:TRΔC +T3
gene12 Blbp dapi
G
ON gene 12 mRNA (x 10²)
-T3
+T3
Blbp Mbp TRΔC +T3

Figure 3.3 Optic nerve and myelin segment shortening is not prevented by cell-type specific expression of the TRΔC transgene

(A) Optic nerve length at Stage 62 for animals expressing the TRΔC transgene under the Isl2, Mbp, or Blbp promoters compared to a control transgene (n= 8 nerves per transgene). **(B)** Optic nerve length at Stage 66 for animals expressing the TRΔC transgene or a control transgene (n= 8). **(C)** Internodal distances of myelin segments measured from confocal images of longitudinal cryo-sections immunolabeled with 3A10 and Neurofascin from animals expressing a control or the TRΔC transgene (n= 40 axons from 4 optic nerves per transgene). All measurements show mean ± SD. **P < 0.01 and ***P < 0.001 by Dunnett's test (A-B) or the Games-Howell test (C).

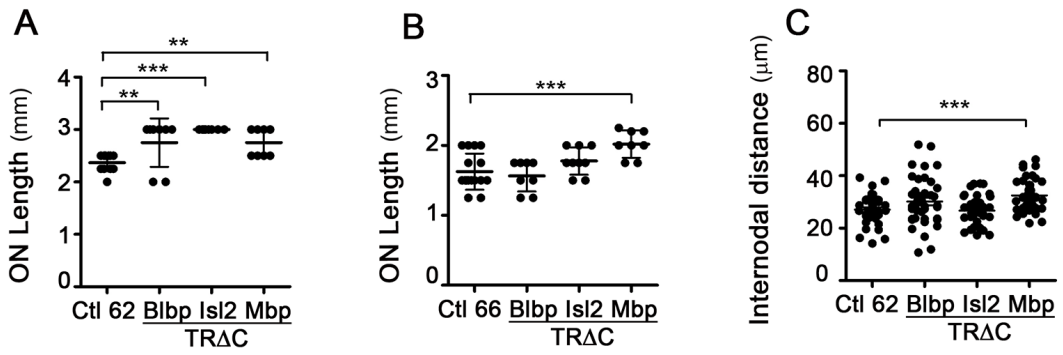

Figure 3.4 Expression of TRΔC transgene does not induce cell death or microglia infiltration in the optic nerve

(A) Optic nerve cryo-sections from wild-type or animals at Stage 62 immunolabeled with Mbp (myelinated axons, green), cleaved-caspase-3 (degenerating axons, red), Dapi (nuclei, blue) from animals expressing the Isl2: GFP-TRΔC transgene (or wild-type control), **(C)** Mbp: rtTA/TetOp: GFP-TRΔC transgene (or non-doxycycline induced control), or **(E)** Blbp: rtTA/TetOp: GFP-TRΔC transgene (or non-doxycycline induced control). Scale bar = 50 μm. **(B)** Cleaved-caspase-3 segmented signal normalized per unit area per optic nerve for Isl2: GFP-TRΔC (n= 5 nerves), **(D)** Mbp: rtTA/TetOp: GFP-TRΔC (n= 5 nerves), or **(F)** Blbp: rtTA/TetOp: GFP-TRΔC (n= 5 nerves). **(G)** Optic nerve cryo-sections from wild-type or animals at Stage 62 immunolabeled with IB4 lectin-FITC (microglia, green), Laminin (nerve sheath, red), Dapi (nuclei, blue) expressing the Isl2: GFP-TRΔC transgene (or wild-type), **(J)** Mbp: rtTA/TetOp: GFP-TRΔC (or non-doxycycline induced), or **(L)** Blbp: rtTA/TetOp: GFP- TRΔC (or non-doxycycline induced). Scale bar = 50 μm. **(H)** IB4 lectin^{+} cells in optic nerve parenchyma normalized per unit area Isl2: TRΔC (n= 5 nerves), **(K)** Mbp: rtTA/TetOp: GFP-TRΔC (n= 5 nerves), or **(M)** Blbp: rtTA/TetOp: GFP- TRΔC (n= 5 nerves). All measurements show mean ± SD. *P < 0.05 by Student's t-test.

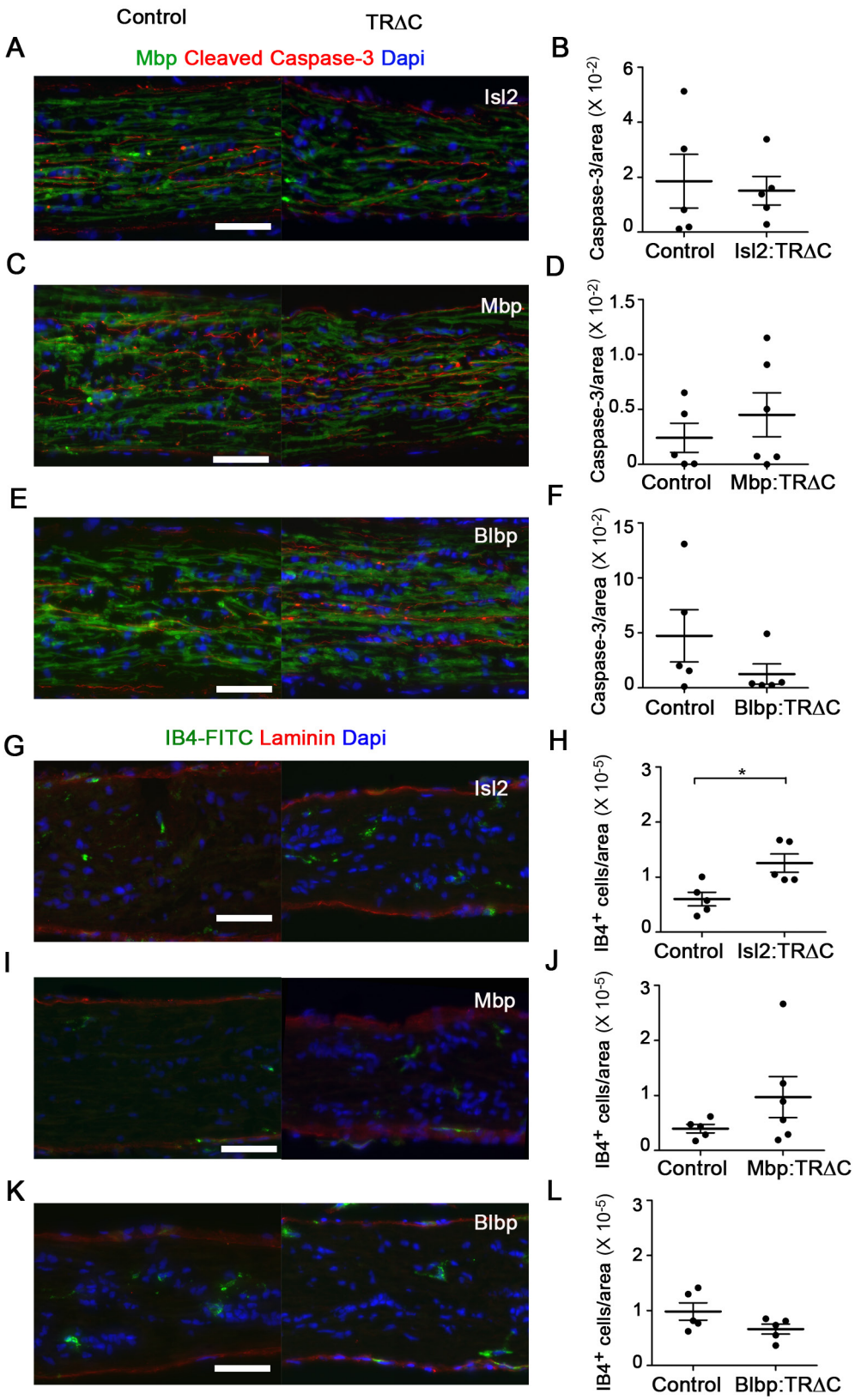
Control
TRΔC
A
Mbp Cleaved Caspase-3 Dapi
Isl2
B
Caspase-3/area (X 10-2)
6
4
2
0
Control
Isl2:TRΔC
C
Mbp
D
Caspase-3/area (X 10-2)
1.5
1.0
0.5
0
Control
Mbp:TRΔC
E
Blbp
F
Caspase-3/area (X 10-2)
15
10
5
0
Control
Blbp:TRΔC
G
IB4-FITC Laminin Dapi
Isl2
H
IB4+ cells/area (X 10-5)
*
3
2
1
0
Control
Isl2:TRΔC
I
Mbp
J
IB4+ cells/area (X 10-5)
3
2
1
0
Control
Mbp:TRΔC
K
Blbp
L
IB4+ cells/area (X 10-5)
3
2
1
0
Control
Blbp:TRΔC

Figure 3.5 Thyroid hormone in RGCs is critical for maintenance of RGCs in the retina and number of myelinated axons in the optic nerve

(A) Number of myelinated axons per optic nerve cross section at Stage 62 (n= 8 Isl2: GFP-TRΔC, n= 15 Control). **(B)** Number of myelinated axons per optic nerve cross section at Stage 66 (n= 8 Isl2: GFP-TRΔC, n= 16 Control). **(C)** Whole-mount retina Stage56 from Isl2: GFP-TRΔC or wild-type animal expressing mRNA for the RGC marker, *rbpms*. Scale bar = 100 μm. **(D)** Number of RGCs per retina at Stage 56 based on expression of *rbpms* (n= 4, Isl2: TRΔC vs. wild-type). **(E)** Whole-mount retina Stage 62 from Isl2: GFP-TRΔC or wild-type animal expressing mRNA for *rbpms*. Scale bar = 100 μm. **(F)** Number of RGCs per retina at Stage 62 based on expression of *rbpms* (n= 10, Isl2: GFP-TRΔC vs. wild-type). **(G)** Whole-mount retina Stage 62 following Terminal deoxynucleotidyl transferase dUTP nick end labeling (TUNEL) from Isl2: GFP-TRΔC or wild-type animals. Scale bar = 100 μm. **(H)** Number of $TUNEL^{+}$ cells in RGC layer per retina normalized to area at Stage 62 (n= 10, Isl2: GFP-TRΔC vs. wild-type). **(I)** Total area of myelin per optic nerve cross-section at Stage 66 (n= 8 Isl2: GFP-TRΔC, n= 16 Control). **(J)** Area of debris myelin per optic nerve cross-section at Stage 66 (n= 8 Isl2: GFP-TRΔC, n= 16 Control). All measurements show mean ± SD. Values for (A-B, and I-J) were derived from traced TEM micrographs. *P < 0.05, **P < 0.01, and ***P < 0.001 by the Games-Howell test (A and J), Student's t-test (D, F, H), or Dunnett's test (B and I).

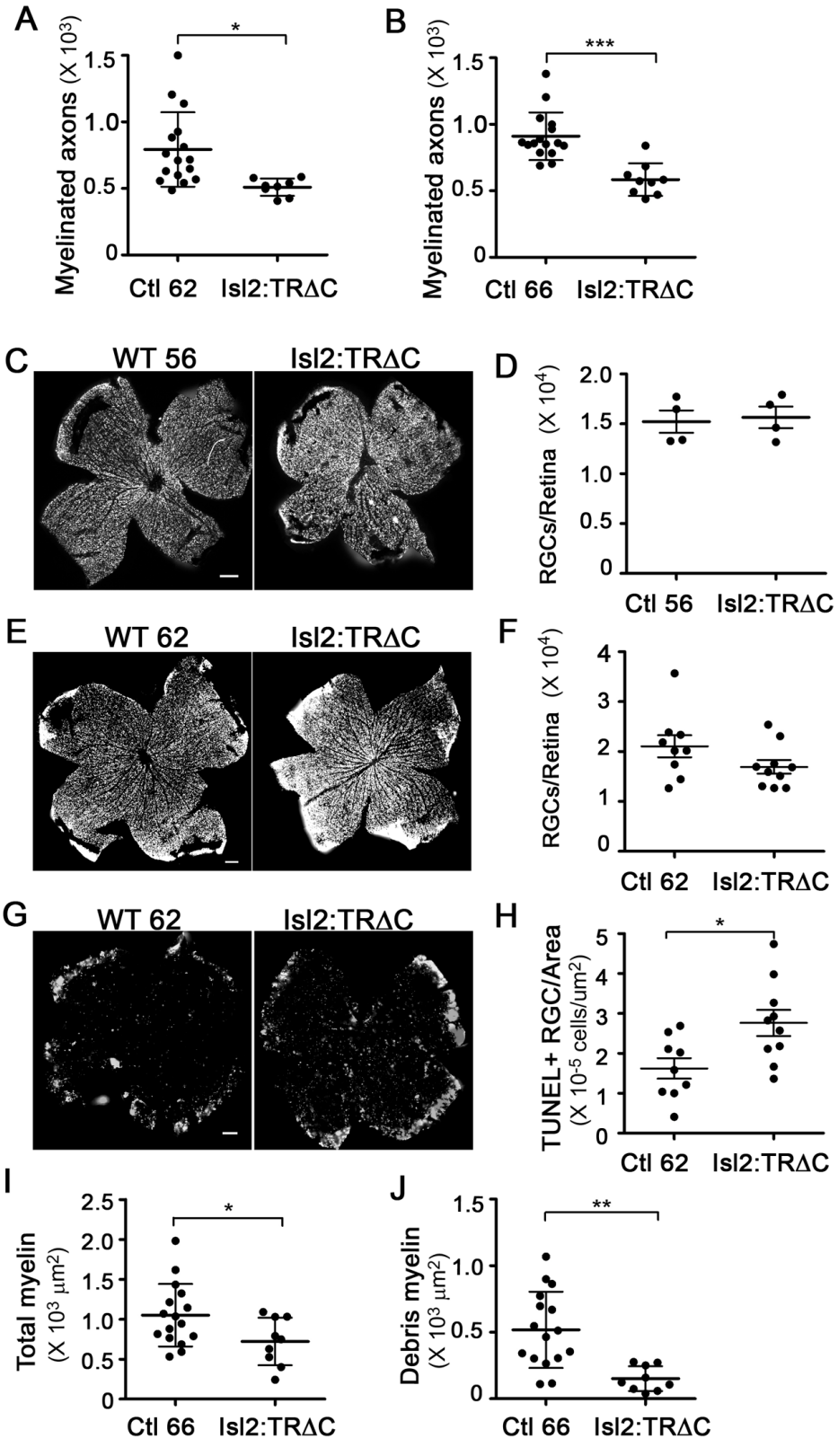
A
Myelinated axons (X 10³)
1.5
1.0
0.5
0
*
Ctl 62
Isl2:TRΔC
B
Myelinated axons (X 10³)
1.5
1.0
0.5
0
***
Ctl 66
Isl2:TRΔC
C
WT 56
Isl2:TRΔC
D
RGCs/Retina (X 10⁴)
2.0
1.5
1.0
0.5
0
Ctl 56
Isl2:TRΔC
E
WT 62
Isl2:TRΔC
F
RGCs/Retina (X 10⁴)
4
3
2
1
0
Ctl 62
Isl2:TRΔC
G
WT 62
Isl2:TRΔC
H
TUNEL+ RGC/Area
(X 10⁻⁵ cells/um²)
5
4
3
2
1
0
*
Ctl 62
Isl2:TRΔC
I
Total myelin
(X 10³ μm²)
2.5
2.0
1.5
1.0
0.5
0
*
Ctl 66
Isl2:TRΔC
J
Debris myelin
(X 10³ μm²)
1.5
1.0
0.5
0
**
Ctl 66
Isl2:TRΔC

Figure 3.6 Expression of the TRΔC transgene in RGCs produced two distinct phenotypes in the optic nerve

(A) Area of axoplasm per myelinated axon averaged per optic nerve at Stage 66 (n= 8 Isl2: GFP-TRΔC, n= 12 Control). **(B)** TEM micrographs of optic nerves from two different animals expressing the Isl2: GFP-TRΔC transgene at Stage 66 showing two groups of phenotypes. The micrograph on the right shows a hyper-vacuolated phenotype. Scale bar = 2 μm. **(C)** Area of peri-axonal space under focal myelin detachments averaged per optic nerve, nerves cluster into two groups having either very large or very small peri-axonal vacuoles at Stage 66 (n= 8 Isl2: GFP-TRΔC, n= 12 Control). All measurements show mean ± SD. Values for A and C derived from traced TEM micrographs. Statistical comparisons were made using Dunnett's test (A) or the Games-Howell test (C). Values based on measurement of 5418 and 2265 axons from Control and Isl2: TRΔC optic nerves, respectively.

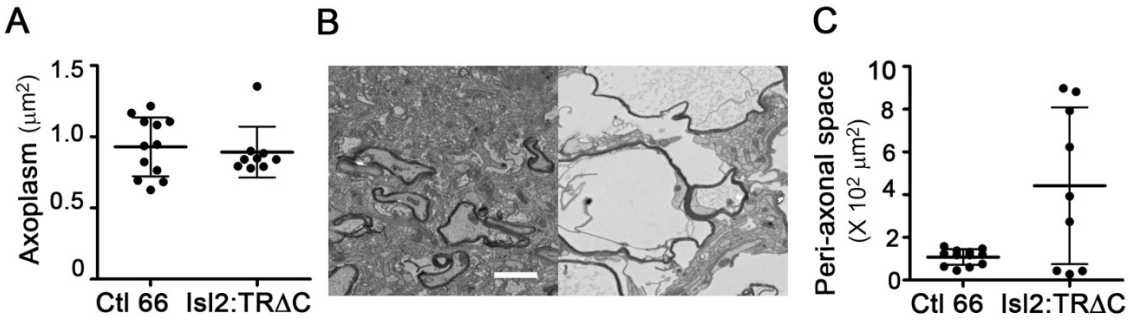

Figure 3.7 Thyroid hormone in oligodendrocytes is necessary for proper myelination

(A) Area of axoplasm per myelinated axon averaged per optic nerve at Stage 62 (n= 8 Mbp: rtTA/TetOp: GFP-TRΔC, n= 15 Control). **(B)** Area of axoplasm per myelinated axon averaged per optic nerve at Stage 66 (n= 8 Mbp: rtTA/TetOp: GFP- TRΔC, n= 12 Control). **(C)** Area of myelin per axon averaged per optic nerve at Stage 62 (n= 8 Mbp: rtTA/TetOp: GFP-TRΔC, n= 15 Control). **(D)** Area of myelin per axon averaged per optic nerve at Stage 66 (n= 8 Mbp: rtTA/TetOp: GFP- TRΔC, n= 16 Control). **(E)** Frequency distribution of G'ratios at Stage 66. Calculated as the ratio of the areas bound by the inner to the outer myelin membranes. **(F)** Total area of myelin on axons per optic nerve cross-section at Stage 66 (n= 8 Mbp: rtTA/TetOp: GFP-TRΔC, n= 16 Control). **(G)** Myelinated axons per optic nerve at Stage 66 (n= 8 Mbp: rtTA/TetOp: GFP-TRΔC, n= 16 Control) **(H)** Optic nerve cryo-sections showing mRNA for *pdgfrα* (OPC marker, red), *plp* (oligodendrocyte marker, green), and nuclear marker Dapi (blue) from Mbp: rtTA/TetOp: GFP-TRΔC animals (+/-doxycycline). Scale bar = 50 μm. **(I)** $Pdgfr\alpha^{+}$ cells per optic nerve cryo-section normalized per unit area (n= 5 nerves). **(J)** Number of Plp^{+} cells per optic nerve cryo-section normalized per unit area (n= 5 nerves). **(K)** Focal myelin detachments per axon averaged per optic nerve at Stage 62 (n= 8 Mbp: rtTA/TetOp: GFP-TRΔC, n= 15 Control). **(L)** Focal myelin detachments per axon averaged per optic nerve at Stage 66 (n= 8 Mbp: rtTA/TetOp: GFP- TRΔC, n= 12 Control). **(M)** Area of peri-axonal space beneath detachments per axon averaged per optic nerve at Stage 66 (n= 8 Mbp: rtTA/TetOp: GFP-TRΔC, n= 12 Control). **(N)** Area of debris myelin per optic nerve cross section at Stage 66 (n= 8 Mbp: rtTA/TetOp: GFP-TRΔC, n= 16 Control). Measurements show mean ± SD. Values for A-F and J-M are derived from traced TEM micrographs and based on measures from 6127 and 3572 axons at Stage 62, and 5418 and 3450 axons at Stage 66 from Control and Mbp: rtTA/TetOp: GFP-TRΔC optic nerves, respectively. *P < 0.01, **P < 0.01, and ***P < 0.001 by the Games-Howell test (A, C, D, L, M, N), Dunnett's test (B, F, G, K), or Student's t-test (I-J).

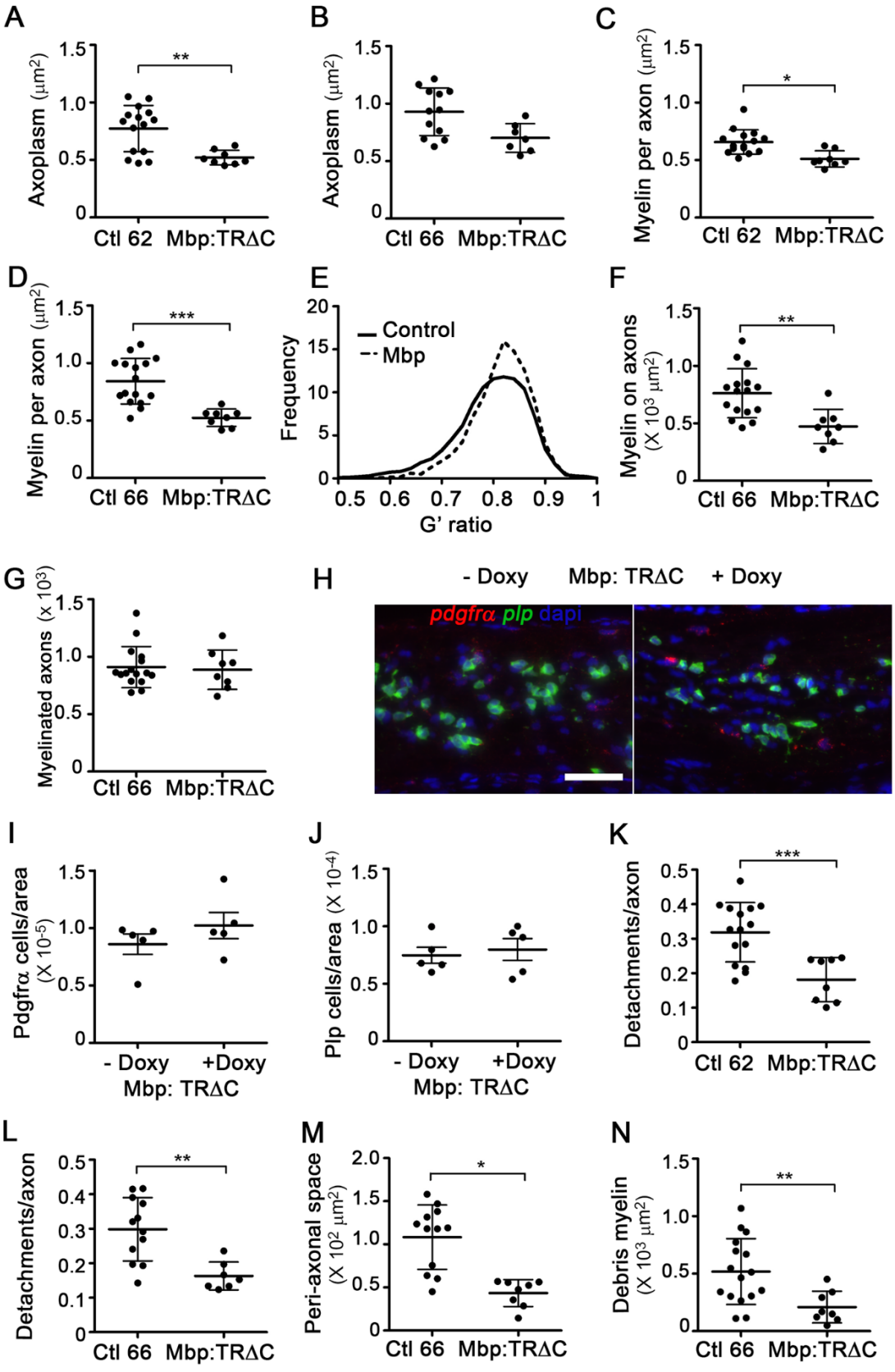
A
Axoplasm (μm²)
1.5
1.0
0.5
0
**
Ctl 62
Mbp:TRΔC
B
Axoplasm (μm²)
Ctl 66
Mbp:TRΔC
C
Myelin per axon (μm²)
*
Ctl 62
Mbp:TRΔC
D
Myelin per axon (μm²)
***
Ctl 66
Mbp:TRΔC
E
Frequency
20
15
10
5
0
Control
Mbp
0.5 0.6 0.7 0.8 0.9 1
G' ratio
F
Myelin on axons (X 10³ μm²)
**
Ctl 66
Mbp:TRΔC
G
Myelinated axons (x 10³)
Ctl 66
Mbp:TRΔC
H
- Doxy
Mbp: TRΔC
+ Doxy
pdgfrα plp dapi
I
Pdgfrα cells/area (X 10⁻⁵)
- Doxy
+Doxy
Mbp: TRΔC
J
Plp cells/area (X 10⁻⁴)
- Doxy
+Doxy
Mbp: TRΔC
K
Detachments/axon
***
Ctl 62
Mbp:TRΔC
L
Detachments/axon
**
Ctl 66
Mbp:TRΔC
M
Peri-axonal space (X 10² μm²)
2.0
1.5
1.0
0.5
0
*
Ctl 66
Mbp:TRΔC
N
Debris myelin (X 10³ μm²)
**
Ctl 66
Mbp:TRΔC

Figure 3.8 Loss of thyroid hormone mediated transcription in astrocytes impairs removal of excess myelin on remodeling axons

(A) Number of myelinated axons per optic nerve at Stage 62 (n= 8 Blbp: rtTA/TetOp: GFP-TRΔC, n= 15 Control). **(B)** Mean area of axoplasm per myelinated axon averaged per optic nerve at Stage 62 (n= 8 Blbp: rtTA/TetOp: GFP-TRΔC, n= 15 Control). **(C)** Ratio of area of myelin to area of axoplasm per axon averaged per optic nerve at Stage 62 (n= 8 Blbp: rtTA/TetOp: GFP-TRΔC, n= 15 Control). **(D)** Number of focal myelin detachments per axon averaged per optic nerve at Stage 62 (n= 8 Blbp: rtTA/TetOp: GFP-TRΔC, n= 15 Control). **(E)** Number of myelinated axons per optic nerve at Stage 66 (n= 8 Blbp: rtTA/TetOp: GFP- TRΔC, n= 16 Control). **(F)** Ratio of area of myelin to area of axoplasm per axon averaged per optic nerve at Stage 66 (n= 8 Blbp: rtTA/TetOp: GFP-TRΔC, n= 12 Control). **(G)** Percentage of detached myelin area relative to axon size at Stage 66 (n= 8 Blbp: rtTA/TetOp: GFP- TRΔC, n= 12 Control). **(H)** Ratio of cells expressing mRNA for *plp* (oligodendrocyte) to *pdgfrα* (OPC) per optic nerve cryo-section for Blbp: rtTA/TetOp: GFP-TRΔC (+/- doxycycline) at Stage 62 (n= 5 nerves). **(I)** mRNA for phagocytic receptors *itgβ3*, *lrp1*, *megf10* (red) and Blbp immunolabeling (green) in optic nerve cryo-sections at Stage 62 for Blbp: rtTA/TetOp: GFP-TRΔC (+/- doxycycline). All measurements show mean ± SD. Values derived from traced TEM micrographs and based on measures of 6127 and 3482 axons at Stage 62, and 5418 and 3014 axons at Stage 66 from Control and Blbp: rtTA/TetOp: GFP-TRΔC optic nerves, respectively. *P < 0.05, **P < 0.01, and ***P < 0.001 by the Games-Howell test (A-C, F-G), or Dunnett's test (D-E), or Student's t-test (H).

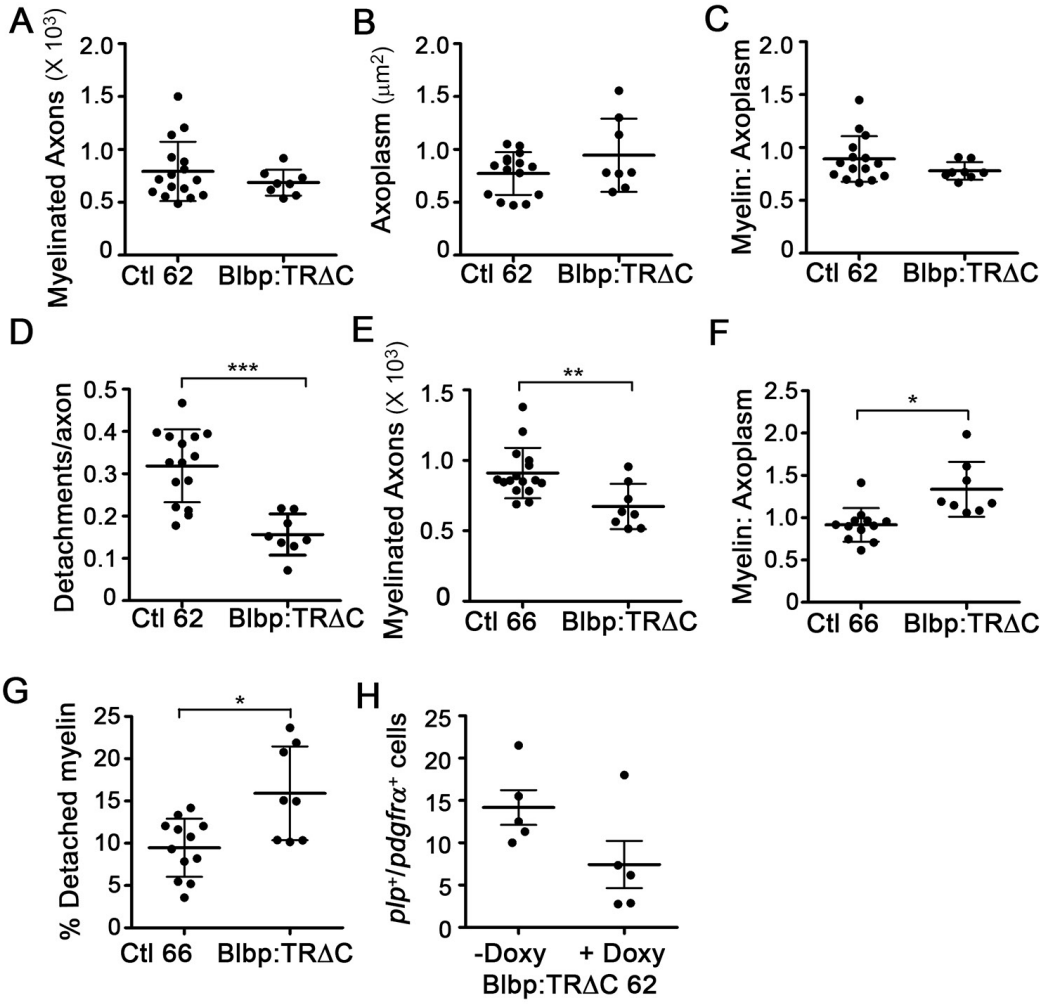
A
Myelinated Axons (X 10³)
2.0
1.5
1.0
0.5
0
Ctl 62
Blbp:TRΔC
B
Axoplasm (μm²)
2.0
1.5
1.0
0.5
0
Ctl 62
Blbp:TRΔC
C
Myelin: Axoplasm
2.0
1.5
1.0
0.5
0
Ctl 62
Blbp:TRΔC
D
Detachments/axon
***
0.5
0.4
0.3
0.2
0.1
0
Ctl 62
Blbp:TRΔC
E
Myelinated Axons (X 10³)
**
1.5
1.0
0.5
0
Ctl 66
Blbp:TRΔC
F
Myelin: Axoplasm
*
2.5
2.0
1.5
1.0
0.5
0
Ctl 66
Blbp:TRΔC
G
% Detached myelin
*
25
20
15
10
5
0
Ctl 66
Blbp:TRΔC
H
plp⁺/pdgfrα⁺ cells
25
20
15
10
5
0
-Doxy
+ Doxy
Blbp:TRΔC 62
I
itgβ3 Blbp
lrp1 Blbp
megf10 Blbp
- Doxy
+ Doxy

Chapter 4: Role of phagocytic optic nerve astrocytes in myelin segment remodeling

Metamorphic remodeling of the optic nerve involves the production and resolution of small hyper-myelinic dystrophies. The presence of cellular processes contacting myelin evulsions on remodeling axons and myelin debris inside cells indicates that the excess myelin is actively removed from axons by cells within the optic nerve. The phenotype of excess myelin on axons at the conclusion of metamorphic optic nerve shortening in the optic nerves from animals expressing a dominant negative version of the thyroid hormone receptor α in astrocytes suggested that thyroid hormone signaling in astrocytes is needed for the proper removal of myelin from axons during remodeling. This result could indicate that astrocytes are directly involved in myelin removal or that thyroid hormone promotes the production and/or secretion of a signal that recruits other phagocytic cells.

Astrocytes have been shown to phagocytose axonal material during axon degeneration (Bechmann and Nitsch, 1997), as well as in non-pathological contexts such as in a homeostatic manner in the rodent optic nerve head (Nguyen et al., 2011), during metamorphic pruning in *Drosophila* (Tasdemir-Yilmaz and Freeman, 2014), and developmental synapse elimination in the visual system (Chung et al., 2013). In contrast, the phagocytosis of myelin by astrocytes has only been demonstrated in the context of degeneration or de-myelination due to injury (Colavincenzo and Levine, 2000; Vaughn and Pease, 1970), aging (Peters, 2002), or disease (Lee et al., 1990). Furthermore, the amount of myelin found to be internalized by astrocytes pales in comparison to professional phagocytes, such as macrophages. Indeed, the most important role for astrocytes in myelin clearance established thus far is the recruitment of macrophages and microglia to lesion sites (Skripuletz et al., 2013). Therefore, I wanted to determine whether astrocytes recruit microglia into the optic nerve during metamorphic remodeling.

Microglia infiltrate the optic nerve to clear degenerating axons following injury

The microglia associated with the optic nerve in *X. laevis* are primarily localized to the optic nerve sheath and infiltrate the optic nerve parenchyma in the context of degeneration inducing injury to clear axonal and cellular debris (Goodbrand and Gaze, 1991). Previous studies have noted the apparent lack of microglia infiltration in the optic nerve during metamorphosis (Cima and Grant, 1982b), therefore I wanted to confirm this observation with a quantitative analysis. I used the microglia/macrophage marker IB4-lectin-FITC to label microglia (Naujoks-Manteuffel and Niemann, 1994) in longitudinal optic nerve cryo-sections.

First, I confirmed that IB4-lectin-FITC reports microglial infiltration using an injury paradigm. The optic nerve was severed behind the eye in Stage 60 tadpoles and the nerves were examined 3 days following injury when the animals were beginning to enter metamorphic climax (Stage 61). The microglia residing in the optic nerve parenchyma and optic nerve sheath were quantified separately for both the cut and contralateral nerves for each animal. The optic nerve sheath was defined by immunolabeling for the extracellular matrix glycoprotein laminin. The number of IB4-lectin positive cells inside the nerve parenchyma and localized to the optic nerve sheath per optic nerve section were manually counted based on expression of both IB4-lectin-FITC and the nuclear marker Dapi (Figure 4.1A-C). The IB4-lectin-FITC signal per unit area was increased in both the optic nerve parenchyma and sheath of the injured optic nerve compared to the contralateral control nerve. This indicates that IB4-lectin positive microglia are capable of infiltrating the optic nerve during metamorphosis in the context of injury. Furthermore, the degenerating axons were rapidly cleared in the injured optic nerves, as indicated by the decrease in cleaved-caspase-3 immunolabeled axons from the first day to the third day following nerve transection (Figure 4.1D), though myelin debris as indicated by Mbp immunolabeling persisted longer.

Microglia are preferentially localized to the nerve sheath and do not infiltrate optic nerve core during metamorphosis

In order to determine whether microglia also infiltrate the optic nerve during the course of metamorphic optic nerve shortening, a similar IB4-lectin-FITC analysis was carried out in optic nerves from animals at Stages 58, 62 and 66 (Figure 4.1E). There was no increase in the amount of IB4-lectin FITC positive cells per unit area during the period of optic nerve remodeling in the optic nerve parenchyma (Figure 4.1F). Interestingly, however, there was an increase in the amount of IB4-lectin positive cells in the optic nerve sheath during optic nerve remodeling as compared to the optic nerves prior to the onset of metamorphic climax (Figure 4.1G). This suggests that microglia are recruited to the optic nerve sheath but do not infiltrate the nerve parenchyma during optic nerve remodeling. Whether astrocytes drive the recruitment of microglia to the sheath remains unclear since optic nerves expressing the thyroid hormone receptor dominant negative transgene in astrocytes had normal numbers of microglia in both the optic nerve core and sheath. In either case, it appears unlikely that microglia are the major phagocytes involved in optic nerve remodeling since the debris myelin is localized to cells within the optic nerve core and most of the microglia reside in the sheath.

Optic nerve astrocytes express phagocytic genes

Since astrocytes are not involved in the recruitment of monocytes into the optic nerve, it is likely that they are the primary phagocytes involved in the removal of excess myelin from remodeling axons during metamorphosis. Transcriptional profiling from purified cortical astrocytes from early postnatal mice revealed that at least during development astrocytes are enriched in genes involved in phagocytosis (Cahoy et al., 2008). In order to determine whether the astrocytes in the optic nerve of *X. laevis* also express phagocytic genes, I used *in situ* hybridization. Optic nerve cryo-sections from animals at metamorphic climax, Stage 62, were found to express phagocytosis associated genes including homologs of the classical *C. elegans* cell death abnormal (ced) genes. The phagocytosis genes expressed in the metamorphic optic nerve are: the receptors *megf10* (ced-1 homolog candidate) (Hamon et al., 2006; Suzuki and

Nakayama, 2007), *megf11* (ced-1 homolog candidate) (Wu et al., 2009), *lrp1* (ced-1 homolog candidate) (Su et al., 2002), *itgβ3* (integrin receptor) (Rubartelli et al., 1997), and *itgβ5* (integrin receptor) (Finnemann et al., 1997), the integrin interacting opsonin *mfge8* (Hanayama et al., 2002), the adaptors: *gulp* (ced-6 homolog) (Su et al., 2002) and *crkII* (ced-2 homolog) (Reddien and Horvitz, 2000), the transporter *abca1* (ced-7 homolog) (Wu and Horvitz, 1998a), the guanine nucleotide exchange factor *dock1* (ced-5 homolog) (Wu and Horvitz, 1998b) with its binding partner *elmo1* (ced-12 homolog) (Gumienny et al., 2001), and the Rho GTPase *rac1* (ced-10 homolog) (Reddien and Horvitz, 2000) (Figure 4.2). Based on the co-localization with the astrocyte marker Blbp, the majority of the cells expressing phagocytic genes are astrocytes. A subpopulation of cells that strongly express the phagocytic genes, but do not co-localize with Blbp can also be found in the optic nerves and likely represent the small population of professional phagocytes previously shown to reside in the nerve, as identified by IB4-lectin. The expression of these phagocytic genes in astrocytes indicates that optic nerve astrocytes contain the phagocytic machinery necessary to remove excess myelin from remodeling axons.

Transgenic intervention of phagocytic machinery in astrocytes using dominant negative constructs

Expression of the phagocytic genes alone, however, does not indicate that the astrocytes use their phagocytic machinery during metamorphic nerve shortening. Therefore, an intervention was needed to determine whether the phagocytic machinery in astrocytes plays a functional role in optic nerve remodeling. Since it is not currently possible to knock-out genes in the allotetraploid *X. laevis* in a conditional manner, I used transgenic over- expression of dominant negative constructs in order to selectively interfere with astrocyte phagocytic genes. Consequently, my analysis was restricted to genes for which dominant negative constructs were possible and had been previously characterized.

Lipoprotein receptor related protein 1, Lrp1, is the best receptor candidate to mediate the internalization of myelin by astrocytes during optic nerve remodeling. Lrp1 plays an important role in lipid metabolism in the central nervous system and has been shown to act as a scavenger receptor to clear cellular debris, including necrotic oligodendrocytes and degenerating myelin (Beisiegel et al., 1989; Gaultier et al., 2009). Unfortunately, Lrp1 is an approximately 85 kb gene which contains numerous functional domains making it an intractable target for transgenic overexpression. The NPXY and NPXYXXL domains in the 51 kD cytoplasmic domain of Lrp1 would be the optimal target sites for intervention, as these sites are involved in the maturation of the receptor and mediating internalization (Reekmans et al., 2010), however, this type of intervention requires the ability to cell type restrict a knock-in a mutation to a specific site in the genome, which is not yet possible in *X. laevis*.

Since Lrp1 could not be genetically manipulated in *X. laevis*, I focused on one of the other ced-1 homologs expressed in astrocytes, Megf11. The Multiple-epidermal-growth-factor-like-domains (MEGF) family of proteins includes several receptors implicated in phagocytosis, namely Megf10, Megf11, and Megf12 (also known as Jedi-1 or Pear-1) (Wu et al., 2009). Megf10 has been shown to participate as a phagocytic receptor in the nervous system through the clearance of apoptotic neurons and during the process of synapse elimination (Chung et al., 2013; Scheib et al., 2012). Over-expression of Megf10 or Megf12 with a truncation of the NPXY and YXXL containing cytoplasm domain has been demonstrated to act as a dominant negative construct with regard to phagocytic activity, at least in cell culture systems (Wu et al., 2009). However, as opposed to previously studied systems with predominantly Megf10 expression, the optic nerve astrocytes of *X. laevis* had very strong expression of Megf11 and much weaker expression of Megf10 (Figure 4.2). A C-terminal truncation of Megf11 would also eliminate its YXXL domain, and thus due to its high homology with Megf10 (Wu et al., 2009), is likely to also function in a dominant negative manner. Therefore, I attempted to interfere with the phagocytic activity of optic nerve astrocytes through the transgenic overexpression of a C-terminal truncated

form of Megf11 fused to GFP under the astrocytic Blbp promoter, Blbp: Megf11ΔC-GFP (abbreviated Blbp: Megf11ΔC).

An electron microscopy based quantitative analysis, similar to the one described for the thyroid hormone dominant negative transgenic lines in Chapter 3, was performed on the optic nerves from animals expressing dominant negative transgenes designed to interfere with phagocytic machinery specifically in astrocytes. Since the purpose of the study was to determine whether optic nerve astrocytes use their phagocytic machinery to remove excess myelin from remodeling axons during optic nerve shortening, the analysis was once again confined to the period of active nerve shortening, Stages 62 and 66. The cross-sectional optic nerve TEM micrographs were traced and quantified as described for the developmental analysis in wild-type animals in Chapter 2. Statistical analysis involved a one-way analysis of variance (ANOVA) and post-hoc multiple comparison tests between all six experimental transgenic lines (3 TRΔC transgenic lines described in Chapter 3 and 3 phagocytic machinery dominant negative transgenic lines described here in Chapter 4) and the control transgenic lines (described in Chapter 3). This method increases the stringency of the analysis so that only differences relevant to a particular intervention and not the small natural variations that are expected in out-bred populations are significant.

Transgenic interference with phagocytic receptor Megf11 has little effect on optic nerve remodeling, but may impair degradation of internalized myelin

The expression of the dominant negative phagocytic receptor, Megf11ΔC, in astrocytes did not significantly affect optic nerve remodeling. On nearly all metrics examined, the optic nerves from animals expressing the Blbp: Megf11ΔC transgene were similar to nerves from animals expressing a control transgene. As expected for a transgene expressed in astrocytes, metrics relevant to RGC axons such as the number of myelinated axons (Figure 4.3A-B) and axon size (Figure 4.3C-D) were unaffected at both metamorphic stages. However, metrics related to

myelin remodeling and removal, including myelin: axoplasm (Figure 4.3E), the amount and size of focal myelin detachments on axons (Figure 4.3F-G), and the amount of debris myelin per optic nerve cross-section (Figure 4.3H) were also similar to control nerves. The amount of myelin on axons and the size of the detachment regions on axons are slightly, but not significantly, elevated at Stage 66, which might suggest that interfering with only one of the phagocytic receptors slightly impairs the removal and internalization of myelin from axons, but overall the system compensates and optic nerve remodeling proceeds in a relatively normal manner. This compensation is not, however, mediated by the increased presence of professional phagocytes, such as microglia, since there was no change in the density of IB4-lectin positive cells in the optic nerves of animals expressing Blbp: Megf11ΔC, as compared to a control transgene (Figure 4.3I-J).

Interference with the Megf11 phagocytic receptor in astrocytes was not completely neutral, and did indeed lead to the production of one prominent phenotype involving debris myelin. The unit size of debris myelin was increased in the optic nerves from Blbp: Megf11ΔC expressing animals with average areas of $0.9 \pm 0.3\ \mu m^2$ and $1.3 \pm 0.3\ \mu m^2$ compared to the areas in control nerves of $0.6 \pm 0.2\ \mu m^2$ and $0.9 \pm 0.3\ \mu m^2$ at Stages 62 and 66, respectively (Figure 4.3K-L). These results likely occurred due to the expression of multiple phagocytic receptors in optic nerve astrocytes such that the loss of any one receptor can be compensated for by an increase in uptake of myelin through the other receptors. Additionally, if Lrp1, not Megf11, is indeed the primary phagocytic receptor involved in myelin internalization then interfering with Megf11 would not be expected to have a major effect on debris myelin internalization. The intracellular domains of each receptor which serve as scaffolds for the binding of other proteins and initiate signaling cascades (May and Machesky, 2001) however, are not identical amongst the various receptors. Therefore, compensation could occur for the internalization of debris, but not necessarily for the downstream signaling that accompanies receptor binding. The Megf11ΔC construct is missing its intracellular signaling domain, and thus works as a dominant negative

when overexpressed by out- competing endogenous receptors for debris binding but failing to initiate the intracellular signaling cascades that would normally accompany receptor binding. Consequently, due to the high homology between Megf10 and Megf11 in the extracellular binding domains, and the lower expression of Megf10 relative to Megf11 in the optic nerve, it is likely that the Megf11ΔC construct operates as a dominant negative to diminish the activity of both receptors. However, if Megf10 were to have a significantly higher affinity for debris myelin than Megf11, the Megf11ΔC construct would have little effect on Megf10 debris binding activity. The fate of phagocytosed particles appears to depend on the receptors involved in the internalization. The signaling downstream of the ced-1 receptor and homologs such as Megf10 and Megf11 has been shown to be involved in phagosome maturation, including lysosome based acidification (Zhou and Yu, 2008). Lack of Megf10/11 debris binding and intracellular signaling might then be expected to lead to normal internalization but impaired acidification, and thus degradation of debris, which would be consistent with the increased unit size of debris myelin in the optic nerves of Blbp: Megf11ΔC expressing animals.

Mfge8-integrin interaction may also be important for myelin degradation in astrocytes and debris clearance

The integrin receptors β3 and β5 were also expressed in the optic nerve astrocytes of *X. laevis*. These receptors have also been shown to participate in the phagocytosis of apoptotic cells (Rubartelli et al., 1997) and photoreceptor outer segments in mammals (Finnemann et al., 1997). The opsonin Mfge8 is a secreted protein that acts as a bridge between apoptotic cells or other debris coated with the 'eat me' signal of the exposed membrane phospholipid phosphatidylserine and integrin receptors on phagocytic cells (Hanayama et al., 2002). A dominant negative version of Mfge8 with a point mutation in the RGD integrin binding domain, Mfge8-D89E, can bind to exposed phosphatidylserine on debris but cannot bind integrin receptors and thus prevents integrin receptor mediated internalization of debris (Hanayama et al., 2002). This dominant

negative construct has been used in mammals to impair the phagocytosis of apoptotic cells by integrin receptor expressing phagocytes (Akakura et al., 2004; Fuller and Van Eldik, 2008). In order to determine the role of integrin receptors in the removal of excess myelin from remodeling axons during metamorphic optic nerve shortening, I expressed a mCherry tagged dominant negative version of *Xenopus* Mfge8, Mfge8-D91E, in astrocytes using the Blbp promoter (Blbp: Mfge8-D91E-mCherry, (abbreviated Blbp: Mfge8-D91E).

The loss of Mfge8 in mice has been associated with a hyper responsive immune system, but the use of the dominant negative transgene in *Xenopus* did not lead to an increased presence of microglia, as determined by IB4-FITC, in the optic nerve (Figure 4.4A-B). The analysis of optic nerve TEM micrographs from animals expressing the Blbp: Mfge8-D91E transgene showed a phenotype similar to the nerves from animals expressing the other phagocytic receptor transgene, Blbp: Megf11ΔC. At the earlier metamorphic time point, Stage 62, the optic nerves appear to show impairment in the generation of debris myelin, likely due to the decreased removal of myelin from axons. The total amount of myelin on axons in Blbp: Mfge8-D91E optic nerves was similar to control nerves (Figure 4.4C), however the percentage of myelin in the form of debris was lower, at only 7.6 ± 2.9% compared to 12.7 ± 4.4% in control nerves (Figure 4.4D). In contrast, by Stage 66, the total amount of axonal myelin was still comparable to controls (Figure 4.4E), yet the percentage of myelin in the form of debris was now elevated to 34.7 ± 10.0% compared to 25.3 ± 8.3% in control nerves (Figure 4.4F). This could be due to a sudden increase in the phagocytic activity of the optic nerve astrocytes during late metamorphic climax, or, more likely, due to an accumulation of internalized myelin within astrocytes. The latter alternative is supported by the slight, but not statistically significant increase in the ratio of myelin: axoplasm (Figure 4.4G) and the increased unit size of debris myelin in the optic nerves from Blbp: Mfge8-D91E expressing animals at Stage 66 (Figure 4.4H). The unit size of debris myelin was 1.5 ± 0.3 μm^2 in Blbp: Mfge8-D91E optic nerves compared to 0.9 ± 0.3 μm^2 in control nerves. This suggests that integrin receptors are involved in the internalization of myelin

early in the remodeling process, but once again they are likely not the primary receptors and the other phagocytic receptors eventually compensate. The primary role for Mfge8-integrin receptor signaling appears to be in mediating the degradation of the internalized debris. A similar role has been described for Mfge8 in dendritic cells since the trafficking of internalized debris to acidified degradative compartments was found to be impaired in dendritic cells from mice lacking Mfge8 (Peng and Elkon, 2011).

Since the Mfge8 transgene was tagged to the fluorophore mCherry, which maintains its fluorescence in acidified environments (Shaner et al., 2004), it was possible to visualize Mfge8 tagged debris in astrocytes during metamorphosis. As a secreted protein, Mfge8 is found throughout the optic nerve, however the tagged Mfge8 transgene is not visible unless it is concentrated and bound to debris, which occurs when small pieces of debris heavily coated in Mfge8 are internalized. Consequently, Mfge8 tagged to a fluorophore that does not withstand internalization or acidification, such as GFP, is not visible in the metamorphic optic nerve (not shown). Therefore, the mCherry fluorescent signal detected in the optic nerves from animals transgenically expressing a mCherry tagged version of Mfge8 most likely represents Mfge8 tagged debris that has been internalized by astrocytes. The debris visible by mCherry fluorescence is likely to be comprised primarily of myelin, since that is the largest source of membranous debris found in the metamorphic optic nerve, however, this could not be confirmed because myelin quickly loses antigenicity following internalization (as described in Chapter 2, Figure 2.9). The size of the mCherry tagged particles in astrocytes is larger in optic nerve cross-sections from animals expressing the dominant negative transgene Mfge8-D91E-mCherry compared to nerves from animals transgenically expressing a wild-type version, Mfge8-mCherry, in astrocytes (Figure 4.4I). Consequently the overall, mCherry signal was higher in optic nerves expressing the dominant negative relative to the wild-type version of the Mfge8 transgene. This increase occurred at a developmental time point prior to optic nerve shortening, Stage 58, and during shortening at Stages 62 and 66 (Figure 4.4J). Although there is much less debris in the

optic nerve at Stage 58, some myelin/membranous debris does exists at this stage and is likely derived from degenerating axons. If Mfge8-integrin mediated internalization and/or signaling is important for the degradation of membranous debris in general, and not specific to metamorphic remodeling, then internalized debris generated throughout development would be expected to accumulate in astrocytes in animals expressing the Mfge8-D91E transgene. Alternatively, it is possible that the interaction with integrin is necessary for Mfge8 to disengage with internalized debris, such that the mCherry tagged transgene is reporting an increase in internalized debris still tagged with Mfge8, and not necessarily an overall buildup of astrocyte internalized debris. The debris myelin phenotypes seen in these animals in the TEM micrograph analysis suggest that membranous debris is indeed accumulating in the astrocytes. Although there is no increase in the amount of Mfge8-mCherry signal per unit area in the optic nerve during metamorphic climax, the cross-sectional area greatly increases as the nerve undergoes a transient hypertrophy at this time (Figure 2.2B), thus the overall amount of mCherry signal increases, but does so in proportion with the size of the nerve.

Lysosomes and lipid droplets increase in astrocyte processes during metamorphic optic nerve remodeling

The build-up of Mfge8 tagged debris within astrocyte processes in the optic nerves of animals expressing a dominant negative version, but not a wild-type version of Mfge8, suggests that debris internalized by astrocytes is normally degraded and/or released by the astrocyte. In order to determine whether there was an increase in the presence of degradative machinery in the optic nerve, I used a transgenic reporter for the tetraspaninin CD63, which is a lysosomal associated protein (Metzelaar et al., 1991) which has been shown to promote lysosome based degradation in other contexts (Takino et al., 2003). Therefore, an increase in CD63 would be expected to indicate an increase in overall lysosome based degradation. The use of a CD63 reporter tagged to mCherry and driven in astrocytes with the Blbp promoter (Blbp: CD63-

mCherry) revealed an increase in the amount of CD63-mCherry signal per unit area in optic nerve cross-sections at Stage 66, relative to Stages 58 and 62 (Figure 4.5A-B). The large increase in CD63 during the stage with the largest amount of debris myelin in the optic nerve, suggests it is involved in the degradation of debris, however, it is also possible that CD63 simply increases in astrocytes during metamorphosis independent of nerve remodeling.

The increase in CD63 suggests that degradative processes are occurring within astrocytes during metamorphic climax, but does not address whether they are related specifically to the degradation of internalized myelin. Lipid droplets are lipid storage organelles involved in lipid metabolism. Although they can be found in most cells, their abundance generally increases in phagocytic cells following the internalization of lipid rich cellular debris (Franson, 1985). Since myelin is extremely lipid, particularly cholesterol, rich the internalization of myelin by phagocytes is associated with the formation of lipid droplets, as a temporary storage for some the lipids most intractable to digestion by the cell (Bignami and Ralston, 1969; Stoll et al., 1989). The developmental TEM micrograph based analysis in wild-type optic nerves revealed an increase in the presence of lipid droplets, particularly in cells containing internalized myelin, during metamorphic nerve remodeling. The use of a fluorescently tagged lipid membrane reporter (Zehmer et al., 2008) expressed in astrocytes, Blbp: hA-AMB-mCherry, revealed that lipid droplets increase in astrocytes during metamorphic climax (Figure 4.5C-D). This further supports the hypothesis that astrocytes are the phagocytic cells in the optic nerve involved in removal of myelin from remodeling axons, and that they are capable of at least partially degrading the myelin they internalize.

The localization of mCherry visualized debris and lipid droplets in astrocyte processes, particularly along the pial lining suggest that the astrocytes may be releasing some of the more intractable lipid debris into the nerve sheath to be picked up by the resident microglia. The buildup of lipid debris in processes abutting the pial lining, no longer identifiable as myelin, is also visible in the TEM micrographs (Figure 4.5E). Furthermore, similar lipid debris and lipid

droplets are present in cells residing in the nerve sheath (Figure 4.5F), which supports the idea that myelin debris partially broken down by astrocytes is ultimately cleared from the nerve into the nerve sheath, which contains vasculature and professional phagocytes.

Interfering with Rac1 impairs the removal of myelin associated with focal axon-myelin detachments on remodeling axons

Due to the presence of multiple phagocytic receptors and the potential for compensation, interfering with the receptors had little effect on optic nerve remodeling overall. Intervention with the candidate phagocytic receptors in astrocytes produced phenotypes related to the processing of debris myelin after it had been internalized which indicates that optic nerve astrocytes are indeed internalizing myelin, but does not indicate the source of the myelin. Therefore, I chose to target the Rho GTPase Rac1, which is involved in the re-organization of the actin cytoskeleton necessary for phagocytic activity and downstream of the multiple receptor pathways (Castellano et al., 2000; Chimini and Chavrier, 2000). I used the construct of GFP tagged Rac1-N17 which acts as dominant negative (Feig and Cooper, 1988) since this form of Rac1 preferentially binds and thereby sequesters GEFs, thus preventing them from activating endogenous Rac (Schweighoffer et al., 1993). The GFP-Rac1-N17 construct was transgenically overexpressed in astrocytes using the Blbp promoter in a tetracycline inducible manner, Blbp: rtTA/ TetOp: GFP-Rac1-N17 (referred to as Blbp: RacN17). In order to circumvent potential developmental defects due to the disruption of the actin cytoskeleton in astrocytes, the transgene was induced just prior to metamorphic nerve remodeling, starting at Stage 58.

Visualization of the transgene using immunohistochemistry for GFP revealed that the transgene is not uniformly expressed in the optic nerve astrocytes (Figure 4.6A). Some astrocytes, preferentially located near the periphery of the nerve had high levels of GFP expression and showed a dystrophic morphology whereby they appear to have retracted some of their cell processes. This phenotype seems consistent with a disruption to the actin cytoskeleton,

as would be expected from a mutation in Rac1. Most of the astrocytes, however, have moderate levels of GFP expression and relatively normal morphology. The reason for this discrepancy is unclear and may indicate that the Blbp: RacN17 transgene is only expressed at a high enough level to effectively act as a dominant negative in a subset of astrocytes, and thus the potency of this intervention may be reduced.

Similar to the other transgenic interventions tested, the expression of the Blbp: RacN17 transgene did not change the amount of microglia, as determined by IB4-FITC, localized to the optic nerve (Figure 4.6B-C). A quantitative analysis of cross-sectional optic nerve TEM micrographs at Stages 62 and 66, as described for the other transgenic lines was undertaken for the Blbp: RacN17 transgene expressing animals. At Stage 62, the optic nerves from the animals expressing the Rac1 dominant negative transgene in astrocytes were similar to control nerves on most metrics, however, there appears to be a specific deficit in the presence of lamellar enwrapped debris myelin when debris is categorized in accordance with the classification scheme described in Chapter 2 (Figure 2.10A-B). The fraction of lamellar enwrapped debris is reduced from 14.1 ± 7.8% in control nerves to 4.4 ± 5.3% in optic nerves from animals expressing the Blbp: RacN17 transgene (Figure 4.6D). This phenotype is consistent with the role of Rac in the remodeling of the actin cytoskeleton, and may be related to the altered astrocyte morphology and reduction in process extension seen in nerves from these animals at this stage at the light level.

The decrease in lamellar enwrapped debris suggests an impairment in the removal of myelin from axons during optic nerve remodeling. By Stage 66, evidence for a myelin removal defect is apparent. Similar to the expression of the thyroid hormone dominant negative transgene in astrocytes, interference with the ability of the actin cytoskeleton to remodel in astrocytes led to an increase in the ratio of myelin: axoplasm for optic nerve axons. The ratio of myelin: axoplasm was elevated from 0.9 ± 0.2 in control nerves to 1.2 ± 0.2 in Blbp: RacN17 optic nerve at Stage 66 (Figure 4.6E). However, unlike in the animals expressing the Blbp: TRΔC transgene, the number and size of the myelinated axons in the optic nerves from Blbp: RacN17 expressing

animals were comparable to control nerves (Figure 4.6F-G). Also, unlike intervention with the individual phagocytic receptors, the unit size of internalized myelin was similar to control nerves (Figure 4.6H), suggesting that the myelin which is internalized is processed and degraded normally, and further supports the hypothesis that myelin degradation is controlled by specific receptor mediated signaling pathways. Instead these nerves showed a trend toward less debris myelin (Figure 4.6I).

Additionally, the optic nerves show evidence of excess myelin remaining on axons through an increase in both the number and size of focal axon-myelin detachments (Figure 4.6J-K), which are clearly visible in the TEM micrographs from these nerves (Figure 4.6L). The area of the peri-axonal space beneath the detachments doubles from $108 \pm 37\ \mu m^2$ in control nerves to $218 \pm 59\ \mu m^2$ in nerves expressing Blbp: RacN17. This suggests that interfering with astrocyte machinery involved in the reorganization of the actin cytoskeleton necessary for phagocytic activity impairs the removal of myelin from axons during metamorphic optic nerve remodeling.

Overall, transgenic intervention of components of the phagocytic machinery in astrocytes during metamorphic optic nerve remodeling led to a reduction in the removal of myelin from axons and the degradation/clearance of the internalized myelin which was not compensated for by an increase in professional phagocytes, such as microglia. Interfering with individual phagocytic receptors did not significantly affect levels of myelin removal/internalization likely due to the presence of multiple phagocytic receptors and produced primarily defects in myelin degradation. Targeting the downstream effector Rac1, circumvented the compensatory effect of multiple receptors and led to optic nerves with too much dystrophic myelin remaining on axons by the end of nerve shortening. Together these results place astrocytes as the primary phagocytes in the removal of excess myelin on remodeling axons during metamorphic optic nerve shortening in *X. laevis*.

Figure 4.1 Microglia infiltrate the optic nerve during injury but not during metamorphic remodeling

(A) Microglia, labeled with IB4 lectin-FITC (green), found in Laminin-immunolabeled optic nerve sheath (red) and optic nerve parenchyma, in optic nerve longitudinal cryo-sections. IB4-lectin^{+} microglia infiltrate the optic nerve parenchyma in Stage 60 animals 3 days after optic nerve transection. Nuclei labeled with Dapi (blue). Scale bar = 50 μm. **(B)** IB4 lectin^{+} cells per optic nerve cryo-section normalized to area in the optic nerve parenchyma 3 days after transection (n= 5). **(C)** IB4 lectin^{+} cell per optic nerve cryo-section normalized to area in the optic nerve sheath (n=5). **(D)** Optic nerve longitudinal cryo-sections immunolabeled with cleaved-caspase-3 (degenerating axons, red) or Mbp (myelin, red), IB4 lectin-FITC (microglia, green) and Dapi (nuclei, blue) on Days 1, 2, and 3 following optic nerve transection at Stage 60. Scale bar = 50 μm. **(E)** Optic nerve longitudinal cryo-sections immunolabeled with IB4 lectin-FITC, Laminin, and Dapi at Stages 58, 62, and 66. Scale bar = 50 μm. **(F)** IB4 lectin^{+} cells per optic nerve cryo-section normalized to area in the optic nerve parenchyma (n= 5 per stage). **(G)** IB4 lectin^{+} cells per optic nerve cryo-section normalized to area in the optic nerve sheath (n= 5 per stage).

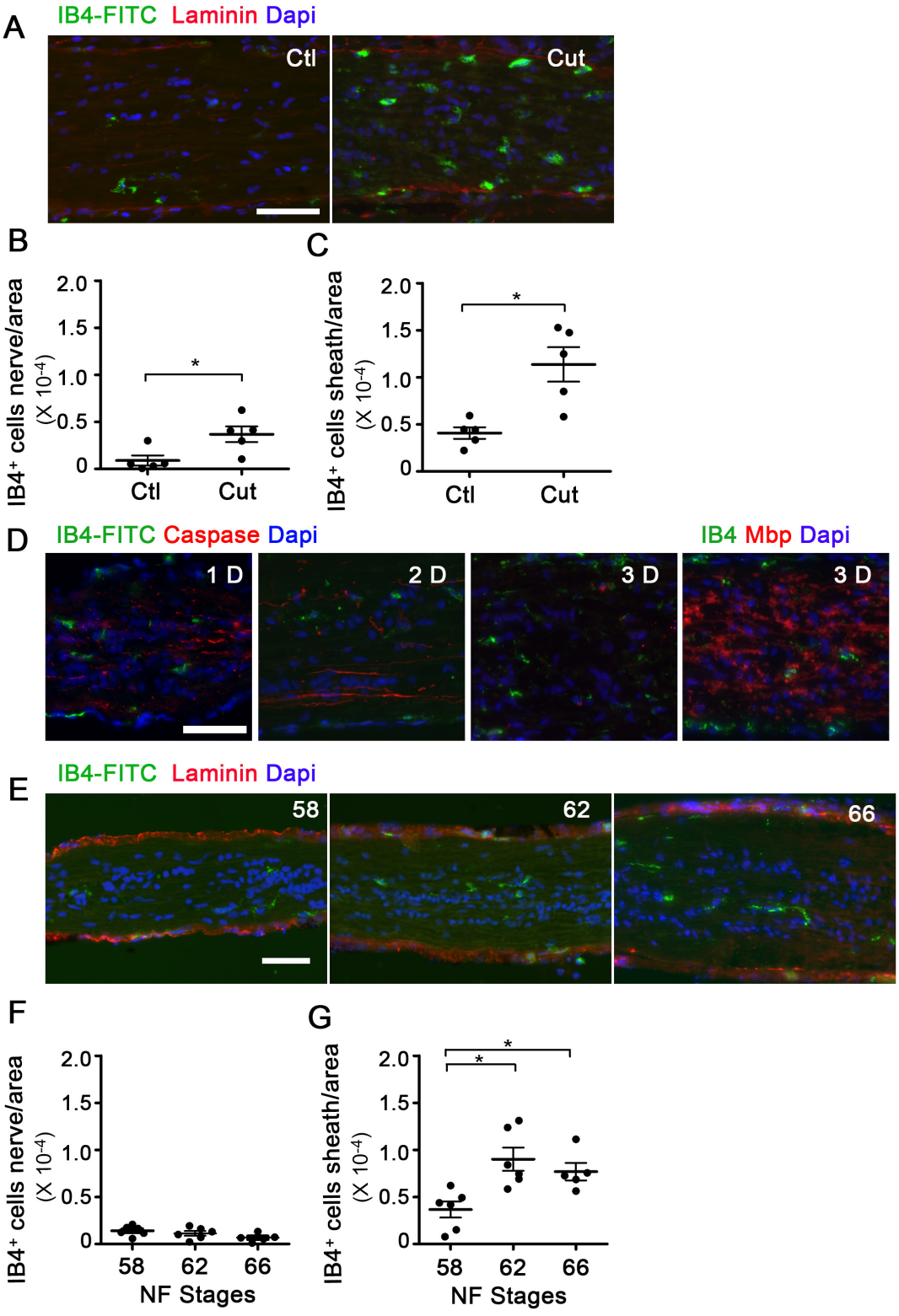
A
IB4-FITC Laminin Dapi
Ctl
Cut
B
IB4⁺ cells nerve/area (X 10⁻⁴)
2.0
1.5
1.0
0.5
0
*
Ctl
Cut
C
IB4⁺ cells sheath/area (X 10⁻⁴)
2.0
1.5
1.0
0.5
0
*
Ctl
Cut
D
IB4-FITC Caspase Dapi
1 D
2 D
3 D
IB4 Mbp Dapi
3 D
E
IB4-FITC Laminin Dapi
58
62
66
F
IB4⁺ cells nerve/area (X 10⁻⁴)
2.0
1.5
1.0
0.5
0
58
62
66
NF Stages
G
IB4⁺ cells sheath/area (X 10⁻⁴)
2.0
1.5
1.0
0.5
0
*
*
58
62
66
NF Stages

Figure 4.2 Optic nerve astrocytes express phagocytic genes

Optic nerve longitudinal cryo-sections show that astrocytes, immunolabled with Blbp (green), express the mRNAs (red) for phagocytic genes, including *abca1, crkII, dock1, elmo1, gulp, itgβ3, itgβ5, lrp1, megf10*, *megf11, mfge8,* and *rac1 as* shown at Stg. 62. Scale bar = 50 μm.

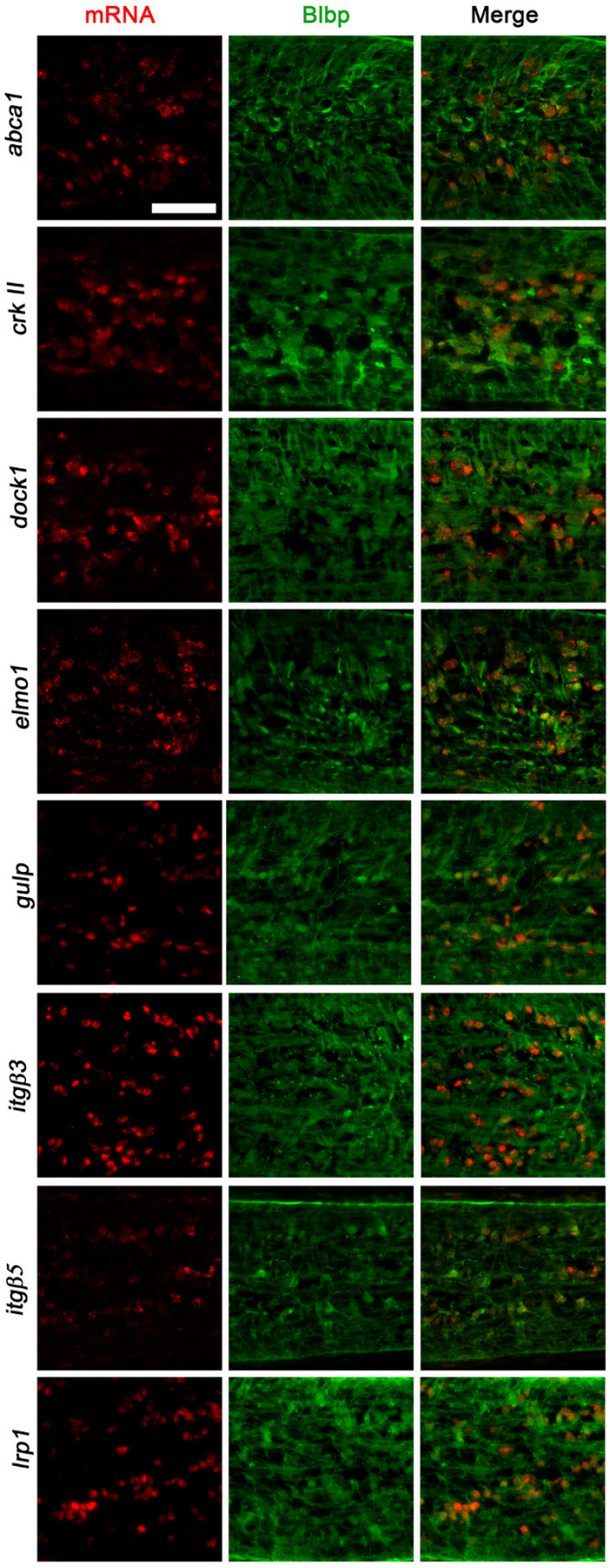
mRNA
Blbp
Merge
abca1
crk II
dock1
elmo1
gulp
itgβ3
itgβ5
lrp1

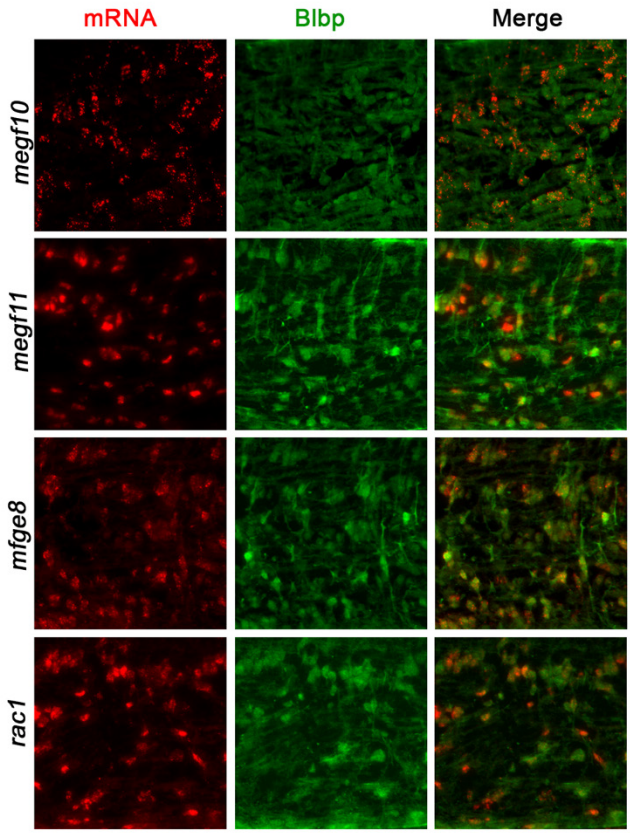
mRNA
Blbp
Merge
megf10
megf11
mfge8
rac1

Figure 4.3 Transgenic interference with Megf11 does not prevent remodeling and leads to larger debris myelin

(A) Number of myelinated axons per optic nerve at Stage 62 (n= 8 Blbp: Megf11ΔC-GFP, n= 15 Control). **(B)** Number of myelinated axons per optic nerve at Stage 66 (n= 8 Blbp: Megf11ΔC-GFP, n= 16 Control). **(C)** Mean area of axoplasm per myelinated axon averaged per optic nerve at Stage 62 (n= 8 Blbp: Megf11ΔC-GFP, n= 15 Control). **(D)** Mean area of axoplasm per myelinated axon averaged per optic nerve at Stage 66 (n= 8 Blbp: Megf11ΔC-GFP, n= 12 Control). **(E)** Ratio of area of myelin to area of axoplasm per axon averaged per optic nerve at Stage 66 (n= 8 Blbp: Megf11ΔC-GFP, n= 12 Control). **(F)** Number of focal myelin detachments per axon averaged per optic nerve at Stage 66 (n= 8 Blbp: Megf11ΔC-GFP, n= 12 Control). **(G)** Area of peri-axonal space beneath focal myelin detachments at Stage 66 (n= 8 Blbp: Megf11ΔC-GFP, n= 12 Control). **(H)** Debris myelin area per optic nerve at Stage 66 (n= 8 Blbp: Megf11ΔC-GFP, n= 16 Control). **(I)** Optic nerve cryo-section immunolabeled with IB4 lectin-FITC (microglia, green), Laminin (nerve sheath, red), and Dapi (nuclei, blue) from Blbp: Megf11ΔC-GFP and control (wild-type) animals at Stage 62. Scale bar = 50 um. **(J)** IB4 lectin^{+} cells per optic nerve cryo-section normalized to area in optic nerve parenchyma (n= 5). **(K)** Mean unit size of debris myelin averaged per optic nerve at Stage 62 (n= 8 Blbp: Megf11ΔC-GFP, n= 15 Control). **(L)** Mean unit size of debris myelin averaged per optic nerve at Stage 66 (n= 8 Blbp: Megf11ΔC-GFP, n= 16 Control). All measurements show mean ±SD. Values for A-H and K-L derived from traced TEM micrographs and based on the measurement of 6127 and 3467 axons at Stage 62, and 5814 and 3187 axons at Stage 66 from the Control and Blbp: Megf11ΔC-GFP optic nerves, respectively. **P < 0.01 and ***P < 0.001. Statistical comparisons made using the Games-Howell test (A, C, E, G, H, L), Dunnett's test (B, D, F, K), or Student's t-test with Welch's correction (J).

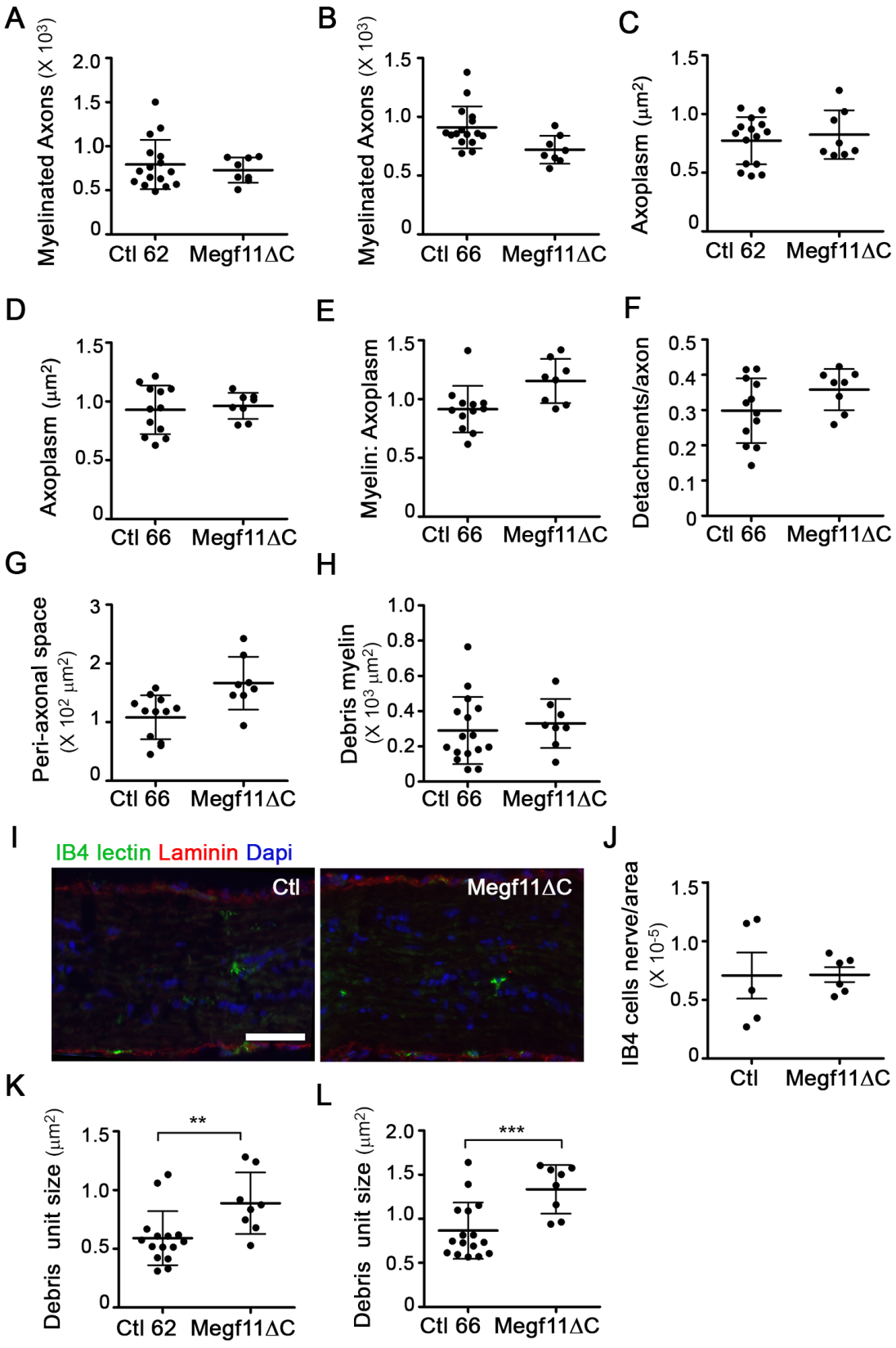
A
Myelinated Axons (X 10³)
2.0
1.5
1.0
0.5
0
Ctl 62
Megf11ΔC
B
Myelinated Axons (X 10³)
1.5
1.0
0.5
0
Ctl 66
Megf11ΔC
C
Axoplasm (µm²)
1.5
1.0
0.5
0
Ctl 62
Megf11ΔC
D
Axoplasm (µm²)
1.5
1.0
0.5
0
Ctl 66
Megf11ΔC
E
Myelin: Axoplasm
1.5
1.0
0.5
0
Ctl 66
Megf11ΔC
F
Detachments/axon
0.5
0.4
0.3
0.2
0.1
0
Ctl 66
Megf11ΔC
G
Peri-axonal space
(X 10² µm²)
3
2
1
0
Ctl 66
Megf11ΔC
H
Debris myelin
(X 10³ µm²)
1.0
0.8
0.6
0.4
0.2
0
Ctl 66
Megf11ΔC
I
IB4 lectin Laminin Dapi
Ctl
Megf11ΔC
J
IB4 cells nerve/area
(X 10⁻⁵)
1.5
1.0
0.5
0
Ctl
Megf11ΔC
K
Debris unit size (µm²)
**
1.5
1.0
0.5
0
Ctl 62
Megf11ΔC
L
Debris unit size (µm²)
***
2.0
1.5
1.0
0.5
0
Ctl 66
Megf11ΔC

Figure 4.4 Transgenic interference with Mfge8-Integrin receptor association primarily leads to larger debris myelin

(A) Optic nerve longitudinal cryo-sections at Stage 62 immunolabled with IB4 lectin-FITC (microglia, green), Laminin (nerve sheath, red), Dapi (nuclei, blue) from animals expressing a transgene for the wild-type or dominant negative (Mfge8D91E) version of Mfge8 in astrocytes. **(B)** IB4 lectin^{+} cells per optic nerve cryo-section normalized to area in the optic nerve parenchyma (n= 5 Blbp: Mfge8-mCherry vs. Blbp: Mfge8D91E-mCherry). **(C)** Total area of myelin on axons at Stage 62 per optic nerve cross-section (n= 8 Blbp: Mfge8D91E-mCherry, n= 15 Control). **(D)** Percent of optic nerve myelin in the form of debris at Stage 62 per optic nerve cross-section (n= 8 Blbp: Mfge8D91E-mCherry, n= 15 Control). **(E)** Total area of myelin on axons at Stage 66 per optic nerve cross-section (n= 7 Blbp: Mfge8D91E-mCherry, n= 16 Control). **(F)** Percent of optic nerve myelin in the form of debris at Stage 66 per optic nerve cross-section (n= 7 Blbp: Mfge8D91E-mCherry, n= 16 Control). **(G)** Ratio of area of myelin to area of axoplasm per axon averaged per optic nerve at Stage 66 (n= 7 Blbp: Mfge8D91E-mCherry, n= 12 Control). **(H)** Mean unit size of debris myelin per optic nerve cross-section at Stage 66 (n= 7 Blbp: Mfge8D91E-mCherry, n= 16 Control). **(I)** Immunofluorescence due to Blbp: Mfge8-mCherry or Blbp: Mfge8D91E-mCherry transgenes in optic nerve cross-sections at Stage 66. mCherry fluorescence (red) within Blbp immunolabeled astrocytes (green) is higher in animals expressing the dominant negative construct. Scale bar = 50 μm. **(G)** The mCherry signal per unit area is elevated in the Mfge8D91E-mCherry transgene relative to the Mfge8-mCherry transgene at all stages. All measurements show mean ± SD. Values for C-H derived from traced TEM micrographs based on the measurement of 6127 and 2790 axons at Stage 62 and 5418 and 2466 axons at Stage 66 in the Control and Blbp: Mfge8D91E optic nerves, respectively. *$P < 0.05$ and ***$P < 0.001$ by Student's t-test (B), the Games-Howell test (C, E, G, H, J), or Dunnett's test (D, F).

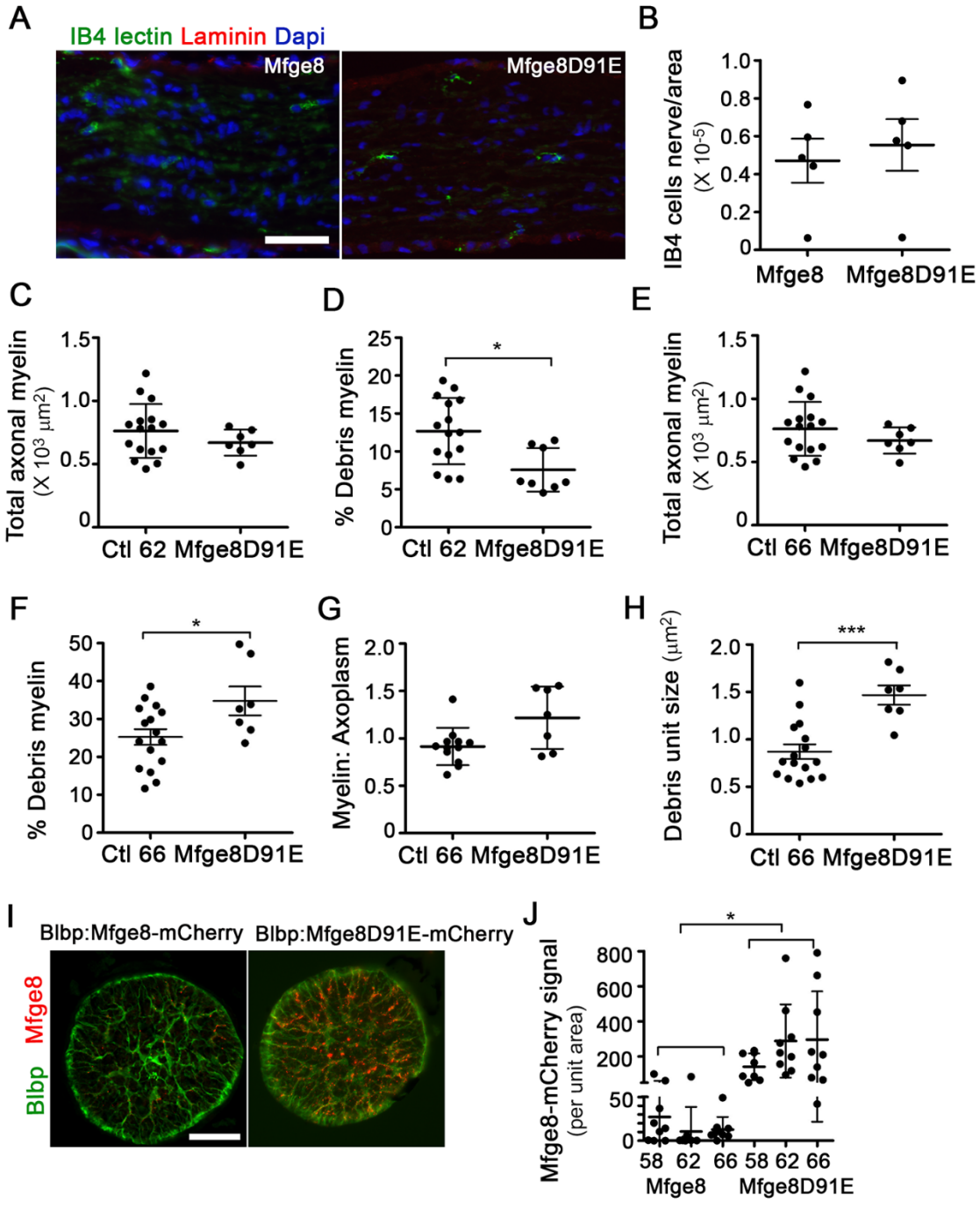
A
IB4 lectin Laminin Dapi
Mfge8
Mfge8D91E
B
IB4 cells nerve/area (X 10-5)
1.0
0.8
0.6
0.4
0.2
0
Mfge8
Mfge8D91E
C
Total axonal myelin (X 10³ µm²)
1.5
1.0
0.5
0
Ctl 62 Mfge8D91E
D
% Debris myelin
25
20
15
10
5
0
*
Ctl 62 Mfge8D91E
E
Total axonal myelin (X 10³ µm²)
1.5
1.0
0.5
0
Ctl 66 Mfge8D91E
F
% Debris myelin
50
40
30
20
10
0
*
Ctl 66 Mfge8D91E
G
Myelin: Axoplasm
2.0
1.5
1.0
0.5
0
Ctl 66 Mfge8D91E
H
Debris unit size (µm²)
2.0
1.5
1.0
0.5
0
***
Ctl 66 Mfge8D91E
I
Blbp:Mfge8-mCherry
Blbp:Mfge8D91E-mCherry
Blbp
Mfge8
J
Mfge8-mCherry signal (per unit area)
800
600
400
200
50
0
*
58 62 66 58 62 66
Mfge8
Mfge8D91E

Figure 4.5 Lysosomes and lipid droplets localized to astrocyte processes increase during metamorphic optic nerve remodeling

(A) Immunofluorescence due to Blbp: CD63-mCherry transgene (exosome/lysosome marker, red) accumulates in processes of Blbp immunolabeled astrocytes (green) in optic nerve cross-sections shown at Stages 58 and 66. Scale bar = 50 μm. **(B)** The mCherry signal for Blbp: CD63-mCherry per unit area is elevated at Stage 66. Measures show mean ± SD (n= 10 optic nerves per stage). *P < 0.05 as assessed by the Games-Howell test. **(C)** Immunofluorescence due to Blbp: A-AMB-mCherry transgene (lipid droplet marker, red) accumulates in processes of Blbp immunolabeled astrocytes (green) during metamorphosis in optic nerve cross-sections shown at Stages 58 and 66. Scale bar = 50 μm. **(D)** The mCherry signal for Blbp: A-AMB-mCherry per unit area is elevated at metamorphic Stages 62 and 66 (n= 10 optic nerves per stage). **(E)** TEM micrographs of optic nerve at Stage 66 showing accumulation of debris myelin and lipid droplets in astrocyte processes (boxed area) contacting the pial lining of the nerve. Scale bar = 1 μm. **(F)** TEM micrographs of optic nerve at Stage 66 showing accumulation of lipid droplets in microglial cells (arrows) located in optic nerve sheath. Scale bar = 1 μm. All measurements show mean ± SD. *P < 0.05 by the Games-Howell test (B) or Tukey's test (D).

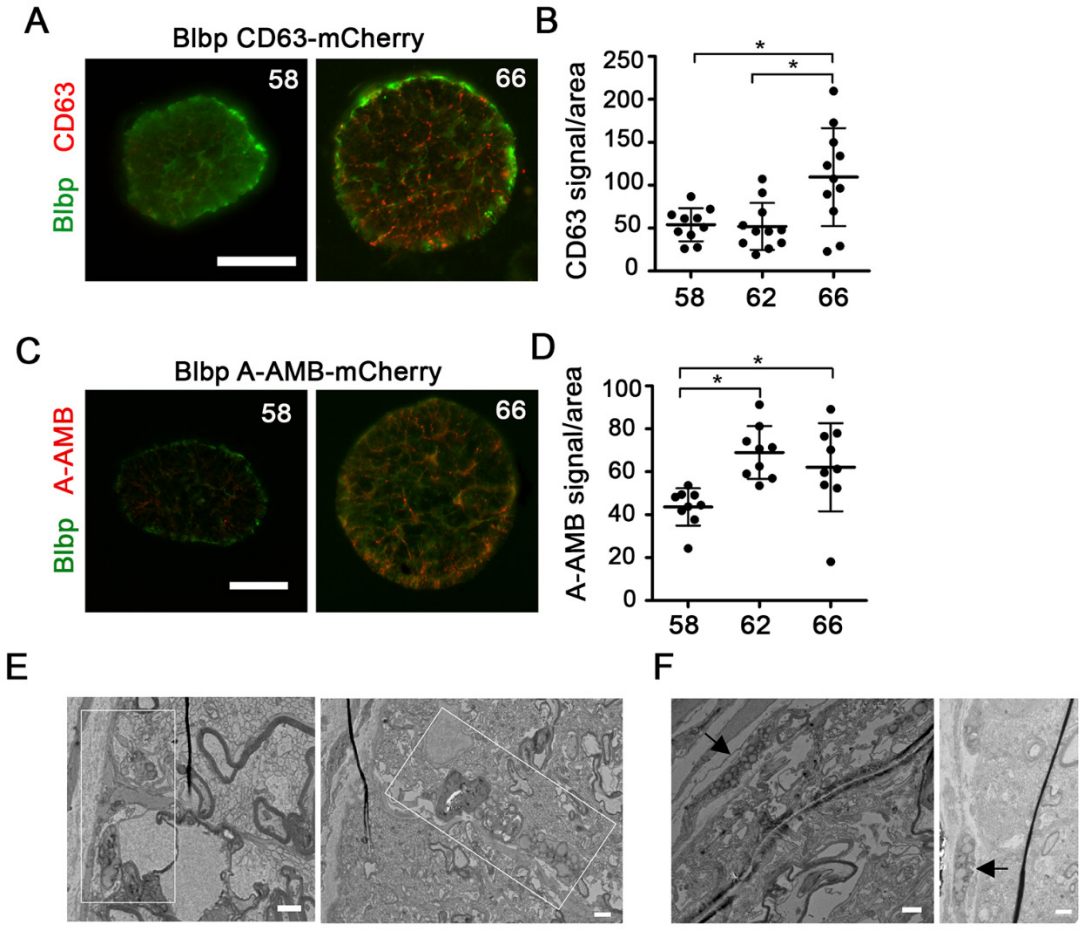
A
Blbp CD63-mCherry
Blbp CD63
58
66
B
CD63 signal/area
250
200
150
100
50
0
58
62
66
*
*
C
Blbp A-AMB-mCherry
Blbp A-AMB
58
66
D
A-AMB signal/area
100
80
60
40
20
0
58
62
66
*
*
E
F

Figure 4.6 Transgenic interference with Rac1 impairs the removal of myelin from remodeling axons during metamorphosis

(A) Optic nerve longitudinal cryo-section from Blbp: rtTA/TetOp: GFP-Rac1N17 expressing animals at Stage 62 immunolabeled with GFP (transgene, green), Blbp (astrocytes, red), and Dapi (nuclei, blue) showing that the transgene is expressed at highest level in a subset of astrocytes near the periphery of the optic nerve. Scale bar = 50 μm. **(B)** Optic nerve longitudinal cryo-sections from animals containing the Blbp: rtTA/TetOp: GFP-Rac1N17 transgene at Stage 62 that were untreated or treated with doxycycline to induce transgene expression, immunolabeled with IB4 lectin-FITC (microglia, green), Laminin (nerve sheath, red), and Dapi (nuclei, blue). **(C)** IB4 lectin^{+} cells per optic nerve cryo-section normalized to area in Blbp: rtTA/TetOp: GFP-Rac1N17 animals with or without doxycycline (n= 5). **(D)** Percentage of debris myelin enwrapped by lamellar processes at Stage 62 per optic nerve cross-section (n= 8 Blbp: rtTA/TetOp: GFP-RacN17, n= 15 Control). **(E)** Ratio of area of myelin to area of axoplasm per axon averaged per optic nerve at Stage 66 (n= 8 Blbp: rtTA/TetOp: GFP-Rac1N17, n= 12 Control). **(F)** Number of myelinated axons per optic nerve at Stage 66 (n= 8 Blbp: rtTA/TetOp: GFP-Rac1N17, n= 16 Control). **(G)** Area of axoplasm per axon averaged per optic nerve cross- section at Stage 66 (n= 8 Blbp: rtTA/TetOp: GFP-Rac1N17, n= 12 Control). **(H)** Mean unit debris myelin size at Stage 66 per optic nerve cross-section (n= 8 Blbp: rtTA/TetOp: GFP-Rac1N17, n= 16 Control). **(I)** Total area of debris myelin per optic nerve cross-section at Stage 66 (n= 8 Blbp: rtTA/TetOp: GFP-Rac1N17, n= 16 Control). **(J)** Number of focal myelin detachments per optic nerve cross-section at Stage 66 (n= 8 Blbp: rtTA/ TetOp: GFP-Rac1N17, n= 12 Control). **(K)** Total area of peri-axonal space beneath focal myelin detachments per optic nerve cross-section (n= 8 Blbp: rtTA/TetOp: GFP-Rac1N17, n= 12 Control). **(L)** TEM micrograph of Blbp: rtTA/TetOp: GFP-Rac1N17 at Stage 66 showing enlargements of the myelin detachments on axons and expansion of peri-axonal space. Scale bar = 2 μm. All measurements show mean ± SD. Values for D-K were

derived from traced TEM micrographs and based on the measurement of 5418 and 2840 axons at Stage 66 from Control and Blbp: rtTA/TetOp: GFP-Rac1N17 optic nerves, respectively. *P < 0.05, ** P < 0.01 and ***P < 0.001 by Student's t-test (C), Dunnett's test (D, F, G), or the Games-Howell test (E, H-K).

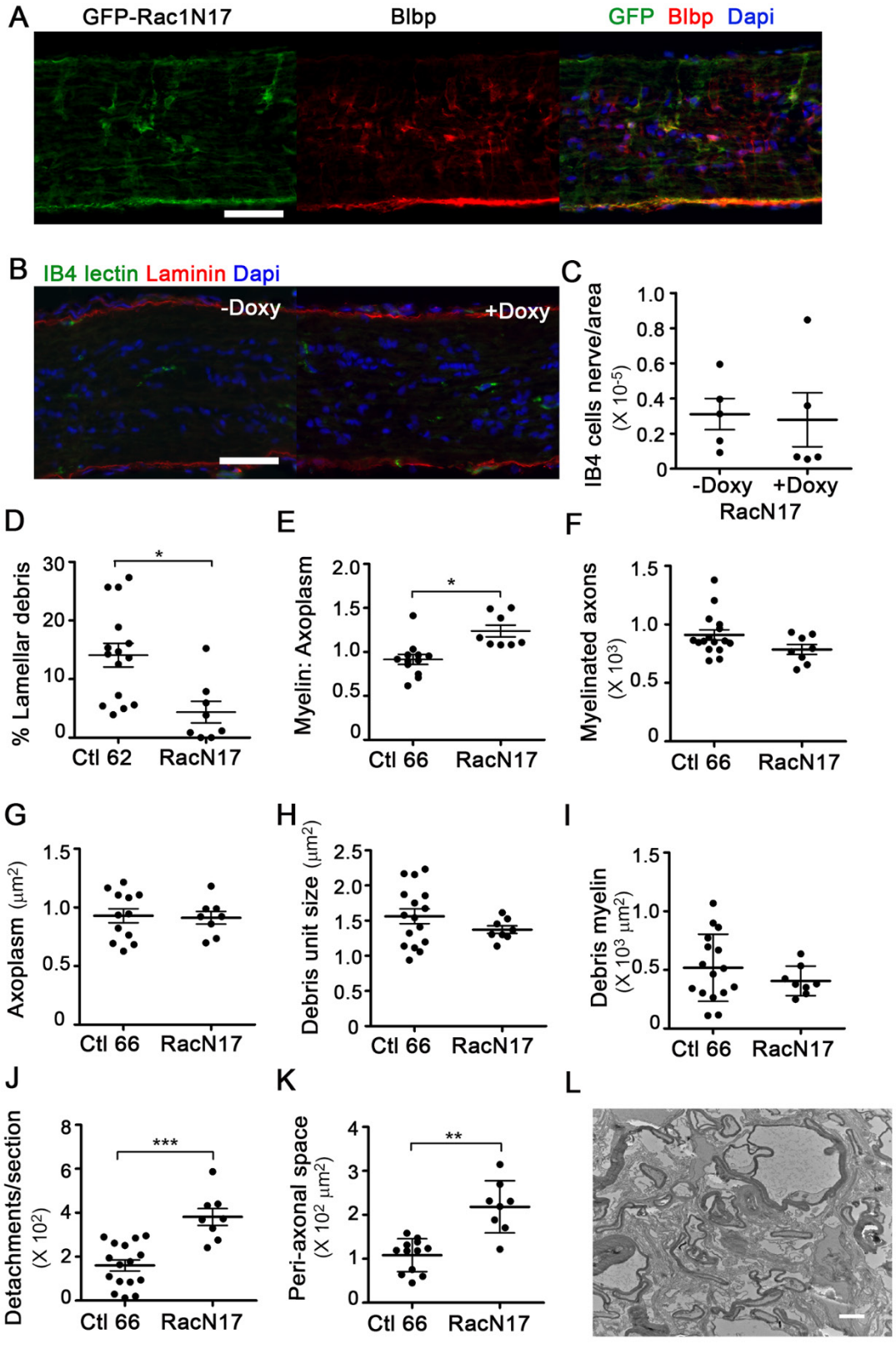
A
GFP-Rac1N17
Blbp
GFP Blbp Dapi
B
IB4 lectin Laminin Dapi
-Doxy
+Doxy
C
IB4 cells nerve/area (X 10-5)
1.0
0.8
0.6
0.4
0.2
0
-Doxy
+Doxy
RacN17
D
% Lamellar debris
30
20
10
0
*
Ctl 62
RacN17
E
Myelin: Axoplasm
2.0
1.5
1.0
0.5
0
*
Ctl 66
RacN17
F
Myelinated axons (X 10³)
1.5
1.0
0.5
0
Ctl 66
RacN17
G
Axoplasm (µm²)
1.5
1.0
0.5
0
Ctl 66
RacN17
H
Debris unit size (µm²)
2.5
2.0
1.5
1.0
0.5
0
Ctl 66
RacN17
I
Debris myelin (X 10³ µm²)
1.5
1.0
0.5
0
Ctl 66
RacN17
J
Detachments/section (X 10²)
8
6
4
2
0
***
Ctl 66
RacN17
K
Peri-axonal space (X 10² µm²)
4
3
2
1
0
**
Ctl 66
RacN17
L

Chapter 5: Discussion

My thesis work has demonstrated that the metamorphic shortening of the optic nerve in *Xenopus laevis* involves the thyroid hormone regulated remodeling of myelin segments by phagocytic astrocytes. This remodeling requires the coordinated activities, as mediated by thyroid hormone, of the three major cell types of the optic nerve; the RGC axons, the myelinating oligodendrocytes, and the astrocytes. It also occurs within the context of massive cell proliferation and new outgrowth, such that new axons are being myelinated while the segments on pre-existing axons are being shortened. During axon shortening, small regions of myelin lose their interaction with the axon membrane. The dystrophic myelin in these detached regions is then selectively removed from the myelin segments by local astrocyte processes using classical phagocytic machinery.

Role of thyroid hormone in optic nerve shortening

Although the shortening of the optic nerve clearly occurs in a thyroid hormone dependent manner, as it can be induced prematurely through exposure to exogenous T3, it is not driven as a direct response to thyroid hormone mediated signaling in any one of the major cell types of the optic nerve. Therefore, it is likely that the shortening of the nerve occurs indirectly, through the thyroid hormone mediated remodeling of muscular and connective tissues in the head. Metamorphic tissue remodeling in other organ systems in *X. laevis*, have been shown to involve non-cell-autonomous effects of thyroid hormone through cell-cell interactions or molecular signals derived from the extracellular matrix (Ishizuya-Oka, 2011). Consequently, it may be that cues from the connective tissue of the sheath drives the shortening of the axons in the optic nerve itself. Incidentally, the use of the Mbp promoter to drive the dominant negative thyroid hormone receptor transgene (TRΔC) produced a slight deficit or delay in optic nerve shortening, which may be attributable to expression in facial connective tissues, which could be detected through a fluorescent reporter in young pre-metamorphic tadpoles. Also, optic nerve shortening is not a

general feature of amphibian metamorphosis, but rather occurs only in a subset of animals such as *X. laevis*, which have laterally oriented eyes during the larval period and whose head greatly decrease in size (Hoskins, 1990). Therefore, it may have made more sense evolutionarily for nerve shortening/remodeling to be initiated in response to head growth related signaling.

Hypertrophy of optic nerve during shortening

A striking feature of the optic nerve at metamorphic climax is the hypertrophy that accompanies shortening. This massive increase in nerve diameter is not simply a function of the compression of axons, but rather involves the expansion of cellular components and the extracellular space, as revealed through electron microscopy. Increases in extracellular fluid are usually associated with trauma in the nervous system, which results in the breakdown of tissue partitions or cellular membranes thus causing an ionic imbalance. Similarly, tissue edema can also occur due to a disruption in the homeostatic functioning of astrocytes (Chen and Swanson, 2003; Manley et al., 2004; Stokum et al., 2014). In the metamorphic optic nerve, a shortening related disruption in the epithelial cells or extracellular matrix of the nerve sheath could lead to an increase in extracellular fluid in the nerve parenchyma from the subarachnoid space. Additionally, a disruption in the flushing of nerve fluid (Xie et al., 2013) into the sheath space, which in mammals also involves transient increases in extracellular space, by pial lining contacting astrocytes could lead to a similar phenotype. This could occur due to a shortening related disturbance in the attachment points of astrocyte endfeet, or thyroid hormone mediated changes in astrocyte function, such as the retraction or mobilization of cell processes in order to mediate the phagocytic removal of myelin from axons. The hypertrophy of the nerve likely occurs through a combination of these and other factors. However, as opposed to injury where such hypertrophy would be an indication of pathology and thus deleterious to the health of the tissue, the expansion of the optic nerve during metamorphosis is part of a highly regulated developmental process which may be beneficial to the remodeling process. Similarly high levels

of extracellular space are also seen in the optic nerve during early development in mammals, particularly during the time of myelination (Williams et al., 1986). Thus the expansion of the optic nerve may provide space for the new outgrowth and myelination of RGC axons. Furthermore, similar to pathological conditions, the space may provide for an increase in the number and mobility of phagocytes, which may enhance the efficiency of debris clearance.

Optic nerve remodeling does not involve an immune response

As a period of extensive nervous system remodeling, cell death is a major feature of metamorphosis. However, in the optic nerve, RGC axon loss is generally associated with new RGCs, and likely reflects a failure in establishing proper connections with the target tissue. In *X. laevis*, the retina grows and adds new RGCs throughout the life of the animal (Straznicky and Hiscock, 1984; Wilson, 1971). The cells are born in the ciliary marginal zone and thus the newest RGCs are located at the margins of the retina (Feldman and Gaze, 1972). Based on the organization of the optic nerve, the axons of these new RGCs are generally localized to the periphery of the nerve, particularly in the ventral region (Cima and Grant, 1982a, b). Consequently, immunolabeling for the dying axon marker, cleaved-caspase-3, confirmed that similar to pre-metamorphic nerves, the majority of dying axons during metamorphic climax are derived from newly projecting RGCs. Furthermore, these axons tend to be small and unmyelinated, whereas the myelinated axons are primarily localized to the central core of the nerve, which contains the largest and oldest axons (Cima and Grant, 1982a). Since these myelinated axons have longer lasting, more stable connections they are less prone to loss (Fried et al., 1982; Jenkins and Straznicky, 1986). Thus, the majority of the debris from axons undergoing Wallerian degeneration is derived from unmyelinated axons and is likely cleared in a typical manner by the small population of microglia in the optic nerve. Normally, there are very few microglia located within the optic nerve parenchyma in *X. laevis*, but they can be readily induced following axonal damage, suggesting their main role is in the removal of damaged cells

(Goodbrand and Gaze, 1991). The ratio of microglia to dying axons is generally maintained throughout metamorphosis, as both were found to increase proportionally with nerve area, such that when normalized to area, these metrics are unchanged throughout development in late stage tadpoles. Therefore, the microglia in the optic nerve appear to be involved in the clearance of a small population of primarily unmyelinated degenerating axons, and not in the shortening induced remodeling of myelin segments.

Optic nerve remodeling involves the production of focal myelin detachments on axons

In contrast, during metamorphosis, the removed myelin is not associated with degenerating axons or localized to debris fields in the extracellular space, but rather is selectively removed from intact myelin segments ensheathing axons. During optic nerve shortening, myelin segments develop focal detachments from the axons they ensheath. These detachments preferentially take place in the central region of the optic nerve. This likely reflects the developmental pattern of myelination, which starts in the center of the nerve and proceeds in a bidirectional manner, indicating that this region would have the highest density of myelin (Cima and Grant, 1982b). Additionally, the axons are likely to experience the greatest loss of tension in the center as the head and nerve sheath shorten, thereby leading to the bending or branching of the axons which occurs during metamorphic climax. This torsion then likely disrupts the already weak interactions between the axon and myelin membranes, leading in turn to the formation of these focal detachments.

These detachments also form preferentially at internodal regions, which may be the result of the adhesive attachments between myelin and axons being stronger at paranodal than internodal regions (Tait et al., 2000). The formation of these detachments, and the shortening of the myelin segments overall, which also likely requires a decrease in the adhesion of the axo-glial complexes at paranodal regions, may be facilitated by the characteristic composition and maturation state of *X. laevis* myelin during metamorphosis. The myelin of *X. laevis* tadpoles,

similar to juveniles in other species, is poor in myelin proteins, like Mbp, and galactolipids, both of which are important for providing stability to the myelin structure (Okamura and Kishimoto, 1983; Trapp et al., 1980). Moreover, a loss or lack of these components destabilize axo-glial interactions and leads to the formation regions of myelin which have lost contact with an axon and associated expansions of the peri-axonal space (Marcus et al., 2002), similar to the focal myelin detachments seen during metamorphic remodeling. The levels and composition of cerebroside, a class of galactolipid and major lipid component of myelin, affect myelin compaction and stability (O'Brien, 1965). Notably, the characteristic composition of cerebrosides in *X. laevis* differ significantly from mammalian myelin in having a greater proportion of unsaturated fatty acids, which would offer less stability to the membrane (Okamura and Kishimoto, 1983). Therefore, the myelin lipids in *X. laevis* confer greater fluidity than mammals, which is likely beneficial for this ectothermic species in adapting to temperature fluctuations. Notably, there is a decrease in myelin cerebrosides specifically during metamorphosis in *X. laevis* (Okamura and Kishimoto, 1983), which may further destabilize the myelin membranes in a manner that facilitates segment remodeling.

Myelin segments shorten at climax then elongate in the post-metamorphic period

Although metamorphosis is the period of transition from a larval to an adult body plan, the immediately post-metamorphic froglet does not yet have a fully mature nervous system. After metamorphosis, the juvenile frog enters another phase of growth, and continues to mature during this time. It is not until this post-metamorphic growth period then that the myelin also matures in terms of composition, structure and function (Cullen and Webster, 1979; Okamura and Kishimoto, 1983; Trapp et al., 1980). Indeed, the period of myelin segment remodeling appears to continue for several weeks past the completion of optic nerve shortening, as focal myelin dystrophies could still be detected at these later time points.

Interestingly, following the initial shortening, the myelin segments appear to elongate again after metamorphosis, which would require myelin synthesis to remain high and the axo-glial interactions to remain weak. Since the length of the nerve itself does not grow significantly during this time, it is likely, that the lengthening of segments requires the selective removal of some of the segments, which would also be facilitated by the presence of weakly attached destabilized myelin. This type of elongation-associated removal also occurs in other species and regions of the nervous system during development (Berthold and Nilsson, 1987; Fried and Hildebrand, 1982; Fried et al., 1982), which may be mediated by the weak adhesion afforded by the characteristic composition of juvenile myelin. Similar to what is seen in these other developmental systems, post-metamorphic segment elongation likely involves a mechanism of competition that results in the removal of the losing segments.

Radial growth and maturation of myelin occur during post-metamorphic period

The elongation occurs alongside the thickening of the myelin segments, as noted by a decrease in G-ratio, which together provide for increased conduction velocity along optic nerve axons (Waxman, 1980). Surprisingly, in spite of all of the remodeling, conduction of the myelinated axons is first detected both within the optic nerve and the optic tectum during metamorphosis (Chung et al., 1974; Chung et al., 1975; Payne, 1977). However, the very fast conduction associated with the adult optic nerve, is not detected until several months after the completion of metamorphosis (Payne, 1977), and likely relates to changes in the composition of myelin and the structure of the segments. The myelin in these juvenile frogs has a higher proportion of stabilizing myelin proteins and galactolipids (Trapp et al., 1980), which offer stronger axo-glial adhesion and enhanced membrane compaction. In general, the fastest conduction speeds in axons are associated with myelin segments with the most wrappings and longest lengths. Thus, the formation of focal detachments and shortening of the segments during metamorphosis likely slows conduction speeds and accounts for the lag between the completion

of metamorphosis and the appearance of fast conduction in the optic nerve. Consequently, the conduction velocities necessary for fast visual processing cannot be achieved until the segments have elongated, adhesive attachments have strengthened and stabilized the myelin, and all myelin dystrophies have been resolved.

Potential physiological significance of myelin segment shortening

Whether the shortening of the myelin segments during metamorphic optic nerve remodeling has a physiological purpose in the development of the visual system pathway, or occurs simply as an intermediate byproduct of nerve shortening remains unclear. The presence of short myelin segments, as occurs during remyelination (Gledhill and McDonald, 1977), results in a decrease in action potential conduction velocity along an axon (Brill et al., 1977), and is typically regarded as a detriment to signal processing. However, segment length variation can also alter conduction timing to contribute to the synchronization or coordination of various inputs onto a single target. This is particularly important for the auditory system, where timing information from the two ears must be integrated (Cheng and Carr, 2007). Single axons that bifurcate to receive input from each ear will have asymmetry in the length of the collaterals, and thus, also need to have different conduction velocities in order to coordinate their input. Recent evidence suggests that the conduction velocities of the two collaterals may be coordinated through oligodendrocyte mediated changes in internodal distance (Seidl, 2014).

During metamorphosis, the change in the position of the eyes in the head of *X. laevis* also underlies a transition from monocular to binocular vision, as the brain must now integrate the overlapping visual fields from the two eyes (Grant and Keating, 1986). Binocular vision develops over time in the juvenile post-metamorphic froglet during a critical period of binocular plasticity, which overlaps with the period of myelin maturation in the optic nerve (Udin, 2007, 2012). The slowed conduction afforded by these shortened segments could affect tectal activity patterns and potentially contribute to this period of plasticity. Conduction timing plasticity typically involves

differences in internodal distance along the length of an axon or between axons, whereas metamorphic segment shortening affects the entire nerve. However, since accurate internodal distance measurements were only obtained in the center region of the optic nerve, with the most active remodeling, it is unclear whether segment lengths in other regions were similarly altered. Since the myelin sheaths actively grow by adding segments along the rostral and caudal directions (Cima and Grant, 1982b), the length of these new segments may or may not be coordinated with the lengths of the remodeled center segments.

Furthermore, new myelin segments are also actively added to previously unmyelinated axons throughout this period, and whether the length of these segments is determined independently based on axon size, or is influenced by the remodeling process remains unknown. In other words, how does the length of newly generated myelin segments compare before, during, and after metamorphosis. Based on the increased diameter of RGC axons following nerve shortening, one might expect that new segments would be longer. However, since newly generated segments could not be unequivocally identified in the SBEM 3View volumes this remains an open question.

Thyroid hormone influences optic nerve myelination during metamorphosis in a cell-type specific manner

Next to segment shortening, the level of new myelination is one of the most striking features of the metamorphic optic nerve in *X. laevis*. Thyroid hormone has been known to promote myelination in mammals by inducing the differentiation of OPCs into mature myelinating oligodendrocytes and the expression of essential myelin components, such as Mbp and Plp (Baas et al., 1997). Thyroid hormone likely works in a similar manner in *X. laevis*, since the number of Plp expressing oligodendrocytes in the optic nerve increases during metamorphic climax. The optic nerves from animals expressing the thyroid hormone dominant negative receptor (TRΔC) transgene in mature oligodendrocytes had normal numbers of oligodendrocytes

and myelinated axons, but less overall myelin. This suggests that the rate of new myelination and thus number of myelinated axons is determined by the amount of mature oligodendrocytes, which is in turn likely determined by the differentiation rate of OPCs. However, since I did not target expression of the TRΔC transgene to OPCs, I cannot definitively conclude that the rise in mature oligodendrocytes during metamorphosis occurs as a direct response to thyroid hormone mediated transcriptional activity. Furthermore, the decrease in the thickness of the myelin sheaths in the optic nerve may be due to a delay or deficit in the maturation of the newly differentiated oligodendrocytes, such as a decrease in process extension or insufficient expression of necessary myelin proteins from the lack of thyroid hormone mediated signaling.

The small size of the axons themselves in animals expressing the TRΔC transgene in oligodendrocytes further suggests that during metamorphosis, thyroid hormone promotes the production of new myelin and thus the expansion of existing segments. Radial growth in axons is largely dependent on a network of neurofilaments, and thus factors that affect the accumulation, localization or phosphorylation status of these cytoskeletal features can alter axon growth dynamics (Williamson et al., 1996). The presence of oligodendrocytes in a nerve prior to myelination can trigger the accumulation and rearrangement of the axon neurofilaments leading to increases in axon caliber (Sanchez et al., 1996). The onset of myelination also affects neurofilament density and phosphorylation, which then leads to further expansion of axons (Cole et al., 1994), such that axon size is determined in part by oligodendrocyte-derived signals. Since the oligodendrocyte provides trophic support to the axon and the thickness of the myelin sheath increases with axon size in a characteristic manner based on the species and conduction velocity requirements of a particular white matter tract, it would be advantageous for a myelinating cell to influence the size of the axon which it ensheaths. If oligodendrocytes are compromised in their ability to produce compact myelin, such as seen in mice with reduced levels of Mbp or MAG, myelin sheaths are thinner and axon caliber is in general similarly decreased (Brady et al., 1999; Yin et al., 1998).

Thinner myelin is also a widely noted feature of remyelination after insult, but so is a corresponding decrease in axon diameter. On average, myelinated axons in an injured region are smaller, with a near absence of the largest caliber axons, suggesting that the newly generated oligodendrocytes may have lower myelogenic potential, and that axon size decreases to match the myelin carrying capacity of the new oligodendrocytes (Powers et al., 2012). In this way, although conduction speeds will be slower than before injury, the health of the axon and conduction can be preserved. In the peripheral nervous system, myelin sheath thickness and associated axon caliber are affected by mammalian target of rapamycin (mTOR) signaling in Schwann cells (Sherman et al., 2012). Notably, the G-ratio is unaffected in these myelinated axons in the absence of mTOR signaling, since both the axon and myelin sheaths are proportionally thinner. mTOR is involved in cell growth and proliferation in a variety of systems and in the central nervous system is thought to be involved in OPC differentiation and myelin production (Wood et al., 2013). Thyroid hormone has been shown to activate mTOR related signaling pathways (Cao et al., 2005), and may also play a role in promoting the radial growth of myelinated axons. The exact nature of the relationship between thyroid hormone, mTOR and myelination in oligodendrocytes, however, remains to be elucidated.

Thyroid hormone could also be acting to promote the rearrangement of the axon neurofilament network directly in RGCs. Although the decreased number of myelinated axons in the optic nerves of animals expressing the TRΔC transgene in RGCs is most likely due to the decreased number of RGCs overall, a deficit in radial axon expansion could also explain the lower myelination rate since myelination only occurs on axons that have reached a particular diameter size threshold. A lack of thyroid hormone has been shown to affect transport of cytoskeletal components such as microtubules and neurofilaments, and thus growth, in the rodent optic nerve (Stein et al., 1991a). Furthermore, the transport of synaptic proteins is also affected in these animals (Stein et al., 1991b), which could impact the ability these axons to produce and maintain synaptic connections. If these axons do not wire properly they may not receive adequate

trophic support and be subject to elimination. Deficits in growth and wiring could contribute to the decreased survival in RGCs with disrupted thyroid hormone signaling. Irrespective of the exact mechanism, proper myelination in the optic nerve appears to require the action of thyroid hormone is both RGCs and oligodendrocytes.

In addition, optic nerve astrocytes may also contribute to myelination, since astrocyte processes interact with actively forming axo-oligodendroglial associations during myelination (Ioannidou et al., 2014) and then continue to interact with mature myelinated axons at Nodes of Ranvier (Waxman, 1986). Blbp expressing astrocytes, such as those found in the optic nerve of *X. laevis*, have been shown to promote the differentiation of OPCs and induce an environment conducive to remyelination after injury (Kipp et al., 2011b). Moreover, thyroid hormone has been shown to be important for the differentiation and maturation of astrocytes, including the production of neuronal growth promoting factors, and extracellular matrix components (Trentin, 2006). Although, the expression of Blbp in progenitor cells may complicate the interpretation, the roles of Blbp expressing astrocytes in promoting axonal growth and myelination may explain the phenotype of decreased axon size and myelination rate in the optic nerves of *X. laevis* expressing the TRΔC transgene under the Blbp promoter. Thus, a lack of thyroid hormone could disrupt the balance of glial cells, inter-cellular signaling, and axon growth. Therefore, during metamorphosis, thyroid hormone appears to influence myelin production through a variety of mechanisms, and thus in turn the ability of oligodendrocytes to support large caliber axons.

Interestingly, the caliber of the myelinated axons in the optic nerve decreases dramatically after metamorphosis back toward pre-metamorphic levels during the juvenile growth period in which myelin matures, and segments increase in length and thickness. This could be related to thyroid hormone mediated changes to axon neurofilaments that are intrinsic to the RGCs or stemming from the myelinating oligodendrocytes, since thyroid hormone levels drop off precipitously after metamorphic climax. Additionally, since the axons undergo a shortening induced hypertrophy during metamorphosis, the associated oligodendrocytes may not be capable

of sustaining support for these axons and trigger an axon shrinkage similar to what is seen in the context of injury. Alternatively, the changes in axon diameter may be explained by the disruption and re-establishment of axo-glial signaling as a result of the production and eventual resolution of focal myelin detachments during optic nerve shortening.

Formation of focal myelin detachments is part of a regulated developmental process and not pathological

Although myelin in juvenile vertebrates is relatively poor in myelin stabilizing components (Horrocks, 1968; Svennerholm and Vanier, 1978; Trapp et al., 1980), these young animals are not adversely affected, since the maturation of myelin is developmentally regulated. In contrast, the lack of these same components in adulthood is abnormal and leads to the onset of pathology (Carenini et al., 1996; Coetzee et al., 1999; Dupree et al., 1998). Similarly, the focal dystrophies within individual segments during metamorphosis are not accompanied by an increase in either axon loss or visible defects in the myelin lamellae compaction, likely because they also stem from a developmentally regulated rather than a pathological process. Indeed, interference with the remodeling process can lead to pathological myelin splitting and vacuolization, as seen in the optic nerves from animals with a disruption in thyroid hormone mediated signaling in RGCs or a component of the phagocytic machinery, Rac1, in astrocytes. Consequently, the process by which myelin debris is cleared during metamorphic optic nerve shortening is quite distinct from clearance in the context of pathology, and is instead reminiscent of axon pruning during early neural development. Instead of the removal of axon or neurite branches, however, optic nerve remodeling involves the removal of focal myelin branches.

Removal of focal myelin dystrophies resembles developmental axon pruning

Perhaps not surprisingly, the removal of the focal myelin detachments during *X. laevis* metamorphosis most resembles neurite pruning during *Drosophila* metamorphic nervous system remodeling (Watts et al., 2004). A key feature of metamorphic pruning is its selective removal of locally degenerating axon or neurite branches while the other branches remain intact (Watts

2003). Although the mechanism underlying this specificity is still unclear, recent evidence suggests that local calcium transients may trigger activation of the protease calpain (Kanamori et al., 2013), which is involved in Wallerian degeneration (Ma et al., 2013). These degenerating branches may then specifically exhibit 'eat me' signals. It is likely that the selective removal of detached myelin during *X. laevis* metamorphosis similarly involves the localized production of 'eat me' cues on focal regions of myelin damaged by nerve shortening.

Metamorphic myelin removal is mediated by optic nerve astrocytes

The exact mechanism underlying this selectivity, however, remains an interesting and open question. Although, unlike pruning in *Drosophila*, the shortening of the myelin segments does not require the recruitment of the astrocytes, the removal of dystrophic myelin produced as a result of shortening is dependent on the phagocytic activity of local astrocytes as indicated by the impairment in the removal of excess myelin from remodeling axons, and accompanying production of myelin pathology associated with the expression of a dominant negative form of Rac1 in astrocytes. Since Rac1 activity affects the reorganization of the actin cytoskeleton in response to various signaling pathways, this result does not provide much mechanistic insight. This phenotype was not replicated by interfering with the candidate phagocytic receptors Megf11 or Integrin (via Mfge8) and suggest that there is redundancy and thus compensation at the receptor level and/or that these are only minor players and that targeting of the primary phagocytic receptor, likely Lrp1, would produce a stronger phenotype. Unfortunately, due to its large multi-functional domain structure (Beisiegel et al., 1989), Lrp1 is not a good candidate for the manipulation of receptor function via the transgenic overexpression of a dominant negative construct, and thus could not be targeted in this study.

Role of thyroid hormone in myelin removal by astrocytes

Similar to the promotion of phagocytic activity in *Drosophila* glia through the ecdysone mediated induction of the phagocytic receptor Draper (Awasaki et al., 2006; Tasdemir-Yilmaz

and Freeman, 2014), thyroid hormone appears to affect the expression of at least a subset of phagocytic genes, such as the Draper homolog Megf10, in *X. laevis* optic nerve astrocytes. Regulation of the phagocytic machinery may then be one of the ways in which thyroid hormone contributes to the ability of astrocytes to remove the dystrophic myelin during metamorphosis. However, since expression of the TRΔC transgene was not induced in astrocytes until tadpoles were NF Stage 58, and thus already exposed to low levels of thyroid hormone, it is not possible to conclude how the transgene is mediating this response. Thyroid hormone may directly affect the transcription of phagocytic genes in astrocytes, as in *Drosophila*, or the effect on phagocytosis may be an indirect consequence of the disruption of other critical processes in astrocytes that are influenced by thyroid hormone. Since thyroid hormone is involved in astrocyte maturation, process out growth and motility (Trentin, 2006), the ability of astrocyte processes to just contact and communicate with myelinated axons could be affected by the level of thyroid hormone. The close association of astrocyte processes with myelinated axons makes them the ideal candidate to mediate this removal, since their continual sampling of the environment (Benediktsson et al., 2005) allows them to readily detect local 'eat me' signals put forth by the damaged or detached myelin.

Capacity of optic nerve astrocytes to internalize and clear myelin

That myelin, as opposed to other cellular membranes or components, is the phagocytic substrate is a critical aspect of *X. laevis* optic nerve remodeling which differentiates it from other developmental glial cell mediated pruning events. The lipid rich nature of myelin makes it extremely difficult to break down, and as such can usually only be internalized by professional phagocytes with the capacity to digest this metabolically rich substance. The ability of astrocytes to internalize myelin is not unprecedented, particularly in frogs and fish, but usually occurs in the context of axonal trauma (Colavincenzo and Levine, 2000). The Blbp expressing astrocytes in these species appear to have a pro-regenerative response in producing pro-myelination signals

and having a greater capacity to clear myelin debris. The ability of these astrocytes to efficiently internalize and metabolize or eliminate large amounts of lipid rich material may underlie the enhanced debris clearance in these astrocytes relative to typical mammalian GFAP expressing astrocytes.

The fatty acid binding protein family, of which Blbp (Fabp7) is a member, appears to be involved in lipid uptake, metabolism and transport in the cell (Furuhashi and Hotamisligil, 2008). Notably, the levels of Fabp in a cell are related to lipid load, which explains their high expression in hepatocytes and adipocytes. Exposure to a lipid rich environment increases the expression of Fabps, which appear to facilitate the uptake and storage of lipids (Smathers and Petersen, 2011). Therefore, the expression of Blbp by the optic nerve astrocytes may increase their capacity to internalize and metabolize lipid rich material, such as myelin. Nuclear transport of transcriptionally active fatty acids by Fabps can also influence gene transcription, including genes involved in lipid metabolism (Schroeder et al., 2008). Interestingly, loss of Blbp in hepatic Kupffer cells has recently been shown lead to the down regulation of the scavenger receptor CD36 and impair phagocytic clearance of apoptotic cells (Miyazaki et al., 2014). Consequently, in optic nerve astrocytes Blbp may contribute to the modulation of transcription or signaling mediated by myelin derived lipids, which could in turn impact the lipid internalization and metabolism of these cells. At this point, however, any potential contribution of Blbp itself to myelin internalization by phagocytic astrocyte remains purely speculative.

Additionally, thyroid hormone affects lipid metabolism in the hepatic system and may also affect lipid processing in astrocytes during metamorphosis. The expression of the endocytic cell surface receptor involved in the uptake of lipids, Lrp1, is regulated by thyroid hormone in the hepatic system (Moon et al., 2013). Based on its role in myelin uptake in other cells (Gaultier et al., 2009) and expression in *X. laevis* optic nerve astrocytes, Lrp1 is the best receptor candidate to mediate the internalization of myelin derived from remodeling segments. Notably, Lrp1 signaling has shown to be pro-regenerative (Yoon et al., 2013), therefore the presence of Lrp1 may

contribute to the increased capacity for regeneration and debris clearance afforded by the Blbp^{+} astrocytes.

Efficient clearance of lipid rich myelin by *X. laevis* optic nerve astrocytes

The enhanced capacity for myelin phagocytosis of the *X. laevis* optic nerve astrocytes may depend more on the effective metabolism and clearance of myelin lipids than the machinery involved in internalization. In macrophages, which have a tremendous capacity for the phagocytosis of lipid rich cellular material, internalization rates are largely dependent on the ability of these cells to efficiently metabolize and efflux these excess lipids. In atherosclerosis, plaque forming foam cells develop from macrophages which are unable to process and eliminate all of the cholesterol they have taken in (Schrijvers et al., 2007). The intake of excessive lipids, such as from myelin, leads to the accumulation of lipid droplets, a lipid storage organelle. Mammalian astrocytes can also take in small amounts of myelin, usually in the context of degeneration, and undergo a subsequent formation of lipid droplets (Vaughn and Pease, 1970). Although the formation of lipid droplets is not in itself detrimental, the long-term accumulation and persistence of lipid droplets in astrocytes is associated with a variety of neurodegenerative diseases (Liu et al., 2010). This suggests that mammalian astrocytes are less efficient at metabolizing lipids, namely cholesterol, than internalizing them, which in turn can have pathological consequences.

In contrast, *X. laevis* optic nerve astrocytes appear to be able to efficiently metabolize or clear the large amounts of myelin they internalize during metamorphic optic nerve remodeling. Although the astrocytes did develop lipid droplets during the height of remodeling at metamorphic climax, the lipid droplets and myelin were largely cleared from the astrocytes within one month. Interestingly, interference with the Integrin-Mfge8 receptor system led to an increase in the size of the myelin debris within astrocytes, suggesting that the myelin was not being properly broken down. This build-up of lipid rich cellular debris could then decrease the

capacity for further internalization, and may contribute to decreased debris internalization seen in other studies (Hanayama et al., 2002). Mfge8 may be important for targeting the debris to the correct degradative compartments in astrocytes, as has been shown for dendritic cells (Peng and Elkon, 2011). However, Integrin-Mfge8 may also be involved in the removal of myelin debris from the astrocytes. In either case, Mfge8 appears to be important for the efficient internalization and degradation of myelin debris by optic nerve astrocytes during metamorphosis.

Lipid droplets and Mfge8-tagged partially metabolized debris were found to accumulate within the pial contacting processes of optic nerve astrocytes. Based on the presence of similar looking debris in the nerve sheath, the astrocytes appear to release some of these debris contents into the sheath space. Furthermore, this is followed by an increase in debris and lipid droplet accumulation in cells localized to the periphery of the sheath, which may be a type of perivascular or microglial cell. A similar trajectory of internalized myelin to lipid droplet formation in astrocytes to lipid droplet accumulation in perivascular cells has been noted in other systems (Franson, 1985). This removal of debris from optic nerve astrocytes may be related to the daily clearance of brain waste products and metabolites into the vasculature by astrocytes (Xie et al., 2013). Although highly speculative, since Mfge8 is secreted and associates with exosome membranes (Oshima et al., 2002), and integrins are highly expressed by the sheath localized cells, Mfge8 coated debris released from astrocytes could be taken up in an integrin dependent manner.

In addition to the release of partially degraded debris into the sheath, the efflux of excess myelin derived cholesterol also likely contributes to the efficient clearance of myelin by *X. laevis* optic nerve astrocytes during metamorphosis. Cholesterol efflux is largely mediated by ATP-binding cassette cholesterol transporters including Abca1, the homolog of ced-6 and major component of the cellular phagocytic machinery (Oram and Lawn, 2001). The decreased expression of Abca1, and thus decreased ability to efflux cholesterol has been found to occur in the lipid overloaded macrophages that become foam cells and contribute to atherosclerosis (Feng and Tabas, 2002). Additionally, the receptor, Lrp1, has been shown to influence expression of

Abca1 by decreasing signaling pathways that transcriptionally repress Abca1 (Zhou et al., 2009). This suggests that the expression of Lrp1 by *X. laevis* optic nerve astrocytes may enhance their ability to efflux cholesterol, and contribute to their ability to internalize and clear large amounts of myelin. Finally, the characteristic composition of myelin in *X. laevis* may contribute to the ability of the astrocytes to effectively clear internalized myelin.

Although astrocytes in mammals may not have the ability to internalize and clear the large amounts of myelin as performed by *X. laevis* astrocytes during metamorphic optic nerve shortening, mammalian astrocytes are capable of internalizing small amounts of myelin. Furthermore, mammalian astrocytes express all of the relevant phagocytic machinery (Cahoy et al., 2008). Therefore, the mechanism of selective removal of focal myelin dystrophies on otherwise intact myelinated axons may be relevant to the homeostatic removal of small amounts of myelin by astrocytes throughout the nervous system in a variety of species. The resolution of focal hypermyelinations on newly myelinated axons (Snaidero et al., 2014) is a potential event that may involve this process, particularly since it occurs during early development when astrocytes are less mature and thus may be more similar to *X. laevis* astrocytes. Another potential exciting role for this process is in white matter plasticity in regions with sparse myelination, whereby it is hypothesized that the selective removal of individual myelin segments may affect the modification of conduction speeds and synaptic site selection (Tomassy et al., 2014).

Overall, I have shown that the remodeling of the optic nerve during the amazing feat of metamorphic optic nerve shortening in *X. laevis* depends on the coordinated activities of RGCs, oligodendrocytes, and astrocytes as regulated by thyroid hormone. While the remodeling of individual myelinated axons involves the selective removal of focal myelin dystrophies induced through shortening by phagocytic optic nerve astrocytes, followed by the efficient clearance of internalized myelin debris.

Chapter 6: Materials and Methods

Animal Care and Breedings

Xenopus laevis were housed in a satellite animal facility located in the Kennedy Krieger Institute associated with the Marsh-Armstrong laboratory. Excellent frog care was provided by the laboratory technician, Shannon Emmel. All animal care and experimental procedures were performed with approval by the Animal Care and Use Committee at Johns Hopkins University. Experiments with wild-type staged *X. laevis* were performed with animals ordered from Xenopus Express. Experiments with transgenic *X. laevis* involved the breeding of founder adult frogs made via REMI transgenesis procedures (Amaya and Kroll, 1999). Breedings were performed between a transgenic founder and a wild-type frog. In preparation for breeding, females were injected with 150 units of human chorionic gonadotropin hormone (hCG) 8-12 hours in advance, and then injected with another 300-400 units of hCG, depending on size, immediately prior to breeding. Males received a single injection of 50 units of hCG immediately prior to breeding. Since the transgenic constructs were fluorescently tagged, the resulting progeny were screened for the presence of the transgene using fluorescence microscopy.

Constructs

X. tropicalis Blbp Promoter

Expression of transgenes in astrocytes was achieved through use of the Blbp promoter in *X. tropicalis* (Watson et al., 2012) based on a Blbp promoter construct originally described in mouse (Schmid et al., 2006). A 1.7kb fragment upstream of the *X. tropicalis* Blbp (aka *fabp7*) gene corresponding to Scaffold 274: 1369583-1367600 in UCSC genome browser *X. tropicalis* (build Nov. 2009 JGI 4.2/xenTro3) was amplified from genomic DNA purified from *X. tropicalis* liver using the primers F and R BLBP (see Primer Table). The DNA was purified using the Puregene DNA purification kit (QIAGEN). The *X. tropicalis* Blbp 1.7kb promoter fragment was digested with the restriction enzymes SalI and HindIII. The vector pCS2-GFP3 was also digested

with SalI and HindIII to remove the sCMV IE94 promoter. The *X. tropicalis* 1.7kb Blbp promoter was inserted into the pCS2: GFP3 vector.

Islet2 promoter construct recombination

Constructs generated using the zebrafish Islet2b promoter (Pittman et al., 2008) were created via homologous recombination (Yu et al., 2000). Inserts were first cloned into a pCS2 (1kb-Islet2) homology vector into the HindIII and XhoI restriction sites. The pCS2 (1kb Islet2) homology vector contains a 1kb fragment of the zebrafish Islet2b promoter between the SalI and HindIII restriction sites, which serves as a homology arm for recombination, and has a kanamycin resistance cassette. Prior to recombination the DNA was digested with SalI and either AloI or DraIII. The DNA was then transformed into EL250 cells, which had undergone RED induction, via electroporation using the settings 1.8kV, 25 μF, and 186 ohms. Colonies were selected based on kanamycin resistance and recombination was verified using diagnostic restriction digests for HindIII and XbaI. The kanamycin cassette was later removed by incubating a culture of EL250 cells expressing the Islet2 construct with 0.1% L-arabinose for one hour.

Thyroid hormone receptor dominant negative constructs

The dominant negative thyroid hormone receptor construct used (TRΔC) is a variant of a previous construct, pCS2:GFP*-TRΔC (Marsh-Armstrong et al., 1999), widely used to inhibit metamorphic events through transgenes. The GFP3 cDNA, amplified using primers F GFP3 and R GFP3, replaced existing cDNA of pCS2(TetOp):GFP (Das and Brown, 2004), using HindIII and XhoI. TRΔC amplified from pCS2:GFP*-TRΔC using F TRΔC and R TRΔC primers was placed downstream of GFP3 into NheI and XhoI sites. GFP3-TRΔC was placed under the zebrafish Islet2 promoter by homologous recombination, as previously described. For conditional expression studies, rtTA2 (Das and Brown, 2004), was amplified with primers F and R rtTA2 and cloned into HindIII-XhoI or BamHI-XhoI pCS2+ vectors that contained a 1.7kb *X. tropicalis* Blbp promoter or 2kb mouse Mbp promoter (Kaya et al., 2012) previously cloned into SalI-HindIII or SalI-BamHI sites, respectively.

Blbp: ctgap43-mCherry

mCherry was amplified from pRSET-B mCherry (Shaner et al., 2004) using primers F and R mCherry N-term tag and cloned into the pCS2 (1.7kb *Xt*Blbp) vector into the HindIII and XhoI sites. A membrane tag, encoding the first 10 amino acids of *X. laevis* growth associated protein 43 (gap43), was made through the annealing of F *Xl*Gap43 and R *Xl*Gap43 overlapping oligos and cloning into the NheI and XhoI sites of Blbp: mCherry.

Isl2: hA-AMB-mCherry

Isl2: hA-AMB-mCherry amplified from pRSET-B mCherry using primers F and R mCherry C-term tag and cloned into the pCS2 (1kb Islet2) homology vector into the HindIII and XhoI sites. The lipid droplet tag human A-AMB (Zehmer et al., 2008) was made through the annealing of overlapping oligos F hA-AMB and R hA-AMB and their cloning upstream of mCherry into HindIII-NheI sites of the pCS2(1kb Isl2)-mCherry vector as an intermediate for recombination to make the Isl2: hA-AMB-mCherry plasmid via recombination as previously described.

Megf11 dominant negative construct (Blbp: Megf11ΔC-GFP3)

The Megf11ΔC construct containing the first 902 amino acids of *X. laevis* Megf11 was made by amplifying *X. laevis* Megf11 from IMAGE clone 4680607 (Open Biosystems) using the primers F and R *Xl*Megf11ΔC and digested with NheI and XhoI and cloned into the pCS2 (1.7kb *Xt*Blbp) vector. GFP3 was then cloned into the XhoI and NotI of the Blbp: Megf11ΔC vector to create the construct Blbp: Megf11ΔC-GFP3.

Mfge8 constructs

mCherry was amplified from pRSET-B mCherry using primers F and R mCherry N-term tag and cloned into the HindIII and XhoI sites of the pCS2 (1.7kb *Xt*Blbp) vector. *X. tropicalis* Mfge8 was amplified from IMAGE clone 5379147 using primers F *Xt*Mfge8 and R *Xt*Mfge8 and cloned upstream of mCherry into the HindIII and NheI sites of Blbp: mCherry. Blbp: Mfge8-

mCherry was mutagenized to Blbp: Mfge8-D91E-mCherry using the QuikChange II Site Directed Mutagenesis Kit (Agilent).

Blbp: CD63-mCherry

Mouse CD63 was amplified from IMAGE clone 6530532 using primers F *Ms*CD63 and R *Ms*CD63 and cloned into the EcoRI and BamHI sites of pCS2: mCherry. CD63-mCherry was then placed under the Blbp promoter by cloning into the NheI and XhoI sites of the pCS2(1.7kb *Xt*Blbp) vector.

Blbp: hA-AMB-mCherry

The hA-AMB-mCherry insert was cloned from pCS2 (1kb Isl2): hA-AMB-mCherry and cloned into the pCS2 (1.7kb *Xt*Blbp) vector into the HindIII and XhoI sites.

Rac1 dominant negative construct (Blbp: rtTA/ TetOp: GFP3-Rac1-N17)

X. tropicalis Rac1 was amplified from IMAGE clone 5336565 using F and R *Xt*Rac1 primers and cloned into pCS2 (TetOp): GFP3 NheI-XhoI sites downstream of GFP3. The pCS2 (TetOp): GFP3-Rac1 was mutagenized to introduce the Rac1N17 mutation using the QuikChange II Site Directed Mutagenesis Kit (Agilent). This construct was used in conjunction with Blbp: rtTA2.

In situ hybridization probe template

The *Xl pdgfrα* probe DNA template was made using RT-RCR. A 820 base pair region of *X. laevis pdgfrα* was amplified from *X. laevis* brain cDNA using the primers F and R rt-XlPdgfrα. RNA was isolated from *X. laevis* tadpole brain using Trizol (Invitrogen) extraction according to the manufacturer's protocol. The cDNA was obtained through a reverse transcriptase reaction using Superscript III (Invitrogen) according to manufacturer's protocol with random hexamers. The *pdgfrα* PCR product was then cloned into the Bluescript KS+ expression vector (Agilent) into the HindIII and XhoI sites.

Primer Table legend: Restriction enzyme sites are capitalized. Kozack sequence is italicized. Mutagenized bases are in bold.

Primer Table

Gene	Forward/Reverse	Sequence
*Xt*BLBP promoter	Forward	aaggagGTCGACcctatgaaagagtgtgttttactg
*Xt*BLBP promoter	Reverse	aaggagAAGCTTcacaaggcagtggaacagatc
GFP3	Forward	aaggagAAGCTTgatatcGCTAGCgatatcgctagcagtaaaggag aagaactttt
GFP3	Reverse	cgCTCGAGttattgtatagttcatccatgcc
TRΔC	Forward	aaggagGCTAGCgaccagaatctcagcgggctgga
TRΔC	Reverse	cgCTCGAGtcaggggcactcgaccttcatg
rtTA2	Forward	agctagGGATCC*gccacc*atgtctagactggacaagagc
rtTA2	Reverse	aaggagCTCGAGttacccggggagcatgtcaaggtcaaa
*Xl*Megf11ΔC	Forward	aaggagGCTAGCgatatcCACGTGcagcaggatacacaggagaga gatgccaggaggagt
*Xl*Megf11ΔC	Reverse	cgCTCGAGcatgcatagccggggtgta
*Xt*Rac1	Forward	aaggagGCTAGCcaggccattaaatgtgtggtcg
*Xt*Rac1	Reverse	aaggagCTCGAGttacaacagcaggcattttct
*Xt*Rac1N17 Mutagenesis	Forward	cggggctgtaggtaaaa**ac**tgtttgctgatcagttac
*Xt*Rac1N17 Mutagenesis	Reverse	gtaactgatcagcaaaca**gt**ttttacctacagccccg
mCherry N-term	Forward	aaggagAAGCTTgattcGCTAGCgtgagcaagggcgagga
mCherry N-term	Reverse	cgCTCGAGttacttgtacagctcgtccatgc
mCherry C-term	Forward	aaggagAAGCTT*gccacc*atggtgagcaagggcgaggagga
mCherry C-term	Reverse	aaggagGCTAGCgatatcCTCGAGcttgtacagctcgtccatgc
*Xl*Gap43 tag	Forward	ctagcatgctgtgctgtatgagaaggacaaaacagtagc
*Xl*Gap43 tag	Reverse	tcgagctactgttttgtccttctcatacagcacagcatg
hA-AMB	Forward	aaggagAAGCTTgatatcGCTAGC*gccacc*atggagcttaccatctt tatcctgag actggccatttacatcctgacatttc
hA-AMB	Reverse	cgCTCGAGgctagcccacaagcccagaaagttcagcaggtacaaggga aatgtcaggatgtaa

*Xt*Mfge8	Forward	aagagAAGCTT*gccacc*atggatggatccgtccgcgct
*Xt*Mfge8	Reverse	atcatcacagcccaggagttcc
*Xt*Mfge8D91E Mutagenesis	Forward	gtctgattctggaagaggtga**a**accttcgtacagt
*Xt*Mfge8D91E Mutagenesis	Reverse	actgtacgaaggt**t**tcacctcttccagaatcagac
*Ms*CD63	Forward	aaggagGAATTC*gccacc*atggcggtggaaggaggaat
*Ms*CD63	Reverse	aaggagGGATCCtttgtatagttcatccat
rt-XlPdgfra	Forward	aaggagAAGCTTactggcgaaagtgaggtgag
rt-XlPdgfra	Reverse	cgCTCGAGacatgggctccaggtcaatg

T3 induction Assay

For 3,3',5-triiodo-L-thyronine (T3) induction assays to examine optic nerve shortening, 5 wild-type Stage 54 *X. laevis* were placed in rearing solution containing 20 nM T3 for 3 days. For T3 induction assays to test TRΔC transgenes, ethyl 3-aminobenzoate methanesulfonate (MS222) anesthetized Blbp: rtTA/TetOp: GFP-TRΔC and Mbp: rtTA/TetOp: GFP-TRΔC transgenic animals received ventricular brain injections of 100 nl of 50 mg/mL doxycycline, and subsequently placed in a rearing solution of 50 mg/L doxycycline. After 24 hours of transgene induction, 3 nM T3 was also added to the rearing water for 2 days. Wild-type and Isl2: TRΔC animals just received the T3 induction.

Transgenesis

Transgenic *X. laevis* were created using restriction enzyme mediated integration (REMI) (Amaya and Kroll, 1999). Female *X. laevis* were pre-primed with an injection of 100 units of hCG approximately 1-4 weeks prior to transgenesis and primed with 400 units of hCG the evening prior to transgenesis and placed in small tanks of 1 X Marc's Modified Ringers (MMR: 100 mM NaCl, 2 mM KCl, 1mM $MgCl_2$, 2mM $CaCl_2$, 5 mM Hepes pH 7.5) solution, so that laid eggs, and not only squeezed eggs, could be used for transgenesis. The transgenic lines Blbp: Mfge8-mCherry, Blbp: Mfge8D91E-mCherry, Blbp: CD63-mCherry, Blbp: hA-AMB-mCherry,

Blbp: ctgap43-mCherry and Blbp: Megf11ΔC-GFP were made using 125 ng of NotI linearized DNA which had been purified with the GeneClean II Kit (MPBio). The transgenic lines Blbp: rtTA/TetOp: GFP-TRΔC, Mbp: rtTA/TetOp: GFP-TRΔC, and Blbp: rtTA/TetOp: GFP-Rac1N17 were made using 100 ng of rtTA construct together with 100 ng of TetOp construct, which had been linearized with NotI and purified with the GeneClean II Kit. The linearized DNA was diluted in distilled water to a total volume of 5 µl and combined with approximately 300,000 *X. laevis* sperm nuclei (80-150 sperm/nl) and incubated at room temperature for 5 minutes. 1 µl of 1:20 NotI enzyme was added to the DNA mixture along with 10 µl of *X. laevis* egg extract and sperm dilution buffer (2mM Hepes, 250 mM sucrose, 75mM KCl, 0.5mM spermidine, 0.2mM spermine, 5mM $MgCl_2$ pH7.5) to reach a total volume of 37 µl, which was then incubated at room temperature for 15 minutes. The DNA was then diluted in sperm dilution buffer (10.5 µl into 200 µl sperm dilution buffer) and loaded into a borosilicate glass capillary tube (WPI TW100-6) which had been pulled using a micropipette puller (Sutter Instruments) using the settings Pull: 70, Velocity: 50, broken to 100 micron diameter tip, beveled to a 30^{o} angle, coated internally with Sigmacote (Sigma) before washing with water.

The transgenic lines with the Islet2 promoter (Isl2: GFP-TRΔC and Isl2: hA-AMB-mCherry) were made using a transgenesis protocol modified for large constructs. Approximately 4 µg of the Islet2b construct DNA was linearized in a 25 µl reaction with NotI and heat inactivated prior to transgenesis. The DNA was incubated with 2.5 µl of reaction mix (10 µl egg extract and 0.5 µl 1:20 NotI enzyme) for 3 minutes at room temperature. Then 1 µl of 80 sperm/nl (or 0.7 µl 150 sperm/nl) was added and incubated 15 minutes. The DNA was diluted in 300 µl of sperm dilution buffer and loaded into a needle for injection. For all transgenic lines eggs were plated on 2% agarose plates in a solution of 0.4X MMR/6% Ficoll/50 µg/mL gentamycin pH 7.6. Injected eggs were transferred to a 16^{o}C incubator and cleaving embryos were screened at the 4 cell stage (approximately 2-3 hours after injection) and transferred to a solution of 0.1X MMR/6% Ficoll/50 µg/mL gentamycin and incubated at 16^{o}C overnight. The following day

healthy embryos were transferred to fresh 0.1X MMR. Screening of transgenic embryos was performed using fluorescence microscopy.

RNA probe synthesis

Digoxigenin or fluorescein labeled RNA probes were synthesized to be used for *in situ* hybridization using DIG or FLU dUTP RNA labeling mix (Roche). The DNA templates for the probes were in RNA expression vectors with T7 and/or T3 RNA polymerase promoters and are listed in the RNA Probe Template Table. The probe synthesis transcription reaction was performed in accordance with the protocol for DIG/FLU RNA labeling mix using T7 or T3 RNA polymerase. Following the transcription reaction, the RNA probe mixture was treated with DNase to remove the DNA template. The probes were then hydrolyzed by adding 2.5 volumes of Hydrolysis solution (0.08M $NaHCO_3$, 0.12M Na_2CO_3) and incubated at 60^{o}C for 30 minutes. The solution was neutralized by adding Neutralization solution (0.1% Acetic acid, 0.2M Sodium acetate pH 5.2). The RNA was precipitated using 0.1 volume of 4M Lithium chloride and 2 volumes of 100% ethanol and incubating at -20^{o}C overnight. The precipitated RNA was recovered through centrifugation and resuspended in DEPC water. Probes were stored at -80^{o}C.

RNA Probe Template Table

GENE	Source
Xt abca1	IMAGE 7799155
Xt crkII	IMAGE 5307606
Xt dock1	IMAGE 6976388
Xt elmo1	IMAGE 6991908
Xl gene12	U41854 (Wang and Brown, 1991)
Xt gulp	IMAGE 7794219
Xl rbpms	NM_001088395(Gerber et al., 1999b)
Xl itgβ3	IMAGE 5512565
Xl Itgβ5	IMAGE 6860110
Xl lrp1	IMAGE 6873186
Xt megf10	IMAGE 7684763
Xl megf11	IMAGE 4680607
Xt mfge8	IMAGE 5379147
Xt nefh	IMAGE 7652316
Xl pdgfrα	NM_00108708
Xl plp	IMAGE 6949052
Xt rac1	IMAGE 5336565
Xt Sncg	IMAGE 7584500

***In situ* hybridization**

In situ hybridization of optic nerve and retina cryo-sections was performed using the following general procedure. *X. laevis* tadpoles and juvenile frogs were euthanized using 0.1% (w/v) ethyl 3-aminobenzoate methanesulfonate (MS222). Optic nerves and/or eyes were dissected in 4% MEM-PFA (0.1M MOPS (pH 7.4), 2mM EGTA, 1mM $MgSO_4$, 4% Paraformaldehyde) at 4°C overnight then cryo-protected with 30% (w/v) sucrose in Phosphate buffered saline (PBS: 137 mM NaCl, 2.7 mM KCl, 10mM Na_2HPO_4, 1.8mM KH_2PO_4 pH 7.4) at 4°C overnight. Optic nerves or eyes were then embedded in cryo-molds with Optimal Cutting Temperature media (O.C.T.) (Sakura Finetek) and stored at -80°C. Cryo-sections 10 μm thickness were made using a Leica CM3050 cryo-stat, placed on Tissue Tack (Polysciences) slides and stored at -80°C.

Day 1: All steps on the first day of the procedure were carried out at room temperature. Slides were washed with 1X PBS, fixed in 4% PFA (pH 7.4) 10 minutes, and washed with 1X

PBS. In some cases slides were incubated with proteinase K and then re-fixed in 4% PFA for 10 minutes. Slides were then acetylated with 0.25% Acetic Acid in 0.1M Triethanolamine (TEA) (pH 8.0) for 10 minutes and washed with 1X PBS. DIG and FLU labeled probes were diluted to 1 ng/µl in hybridization buffer (50% 2X Hybridization solution (sigma H-7140), 50% formamide, 0.25 mg tRNA) and heated to 80°C for 5 minutes. Diluted probe mixture was placed on plastic coverslips and onto slides incubated in a chamber humidified with 50% formamide/5X Saline-sodium citrate buffer (SSC 1X: 150 mM NaCl, 15 mm Sodium citrate pH 7.0) at 65°C overnight. **Day2**: Coverslips were removed by placing slides in 65°C 5X SSC. Slides were then incubated in 0.2X SSC for 1 hour at 65°C and 5 minutes at room temperature, followed by a wash in Buffer B1. For a single, but not a double in situ, peroxidases were quenched by incubating slides in 0.1 % Sodium Azide + 0.3% Hydrogen peroxide for 10 minutes. Slides were placed in a blocking solution of 1% Blocking Buffer (Roche) in Buffer B1 for 1 hour at room temperature prior to antibody incubation. Slides were then incubated with 1:500 Anti-DIG-POD (Roche) or Anti-FLU-POD (Roche) diluted in 1% Roche block/Buffer B1 solution 4°C overnight. **Day 3**: After antibody incubation slides were washed in Buffer B1 at room temperature. The POD antibody was detected using Cy3 or Cy5 tyramide (Perkin-Elmer) diluted 1:100 in amplification buffer. Then the slides were washed in Buffer B1.

For a double *in situ* hybridization: Peroxidases are quenched with 0.1% Sodium Azide and 0.3% Hydrogen peroxide, blocked with Roche block in Buffer B1, incubated with the other POD antibody (DIG or FLU) overnight, which was detected with the other tyramide (Cy3 or Cy5).

In situ hybridization of wholemount retinas was performed using the following general procedure. Retinas were dissected from MS222 euthanized *X. laevis*, fixed in 4% MEM-PFA at 4°C overnight, and stored in 100% Methanol at -20°C. **Day 1:** Retinas were rehydrated by washing in a mixture of methanol and PBT (1X PBS, 0.5% Triton-X) at the ratios 3:1, 1:1, 1:3. Retinas were sealed between sheets of 125µm nylon mesh (Small Parts) using an impulse sealer

and placed into glass scintillation vials. Meshed retinas were washed in PBT 3 times, acetylated with 0.25% acetic anhydride followed by 0.5% acetic anhydride in 0.1M TEA (pH 8.0) for 5 minutes each, washed in PBT, fixed in 4% PFA for 20 minutes, and washed in PBT at room temperature. Retinas were then incubated with Hybridization buffer (50% 2X hybridization solution (sigma H-7140), 50% formamide, 10 mg yeast tRNA, 0.1% of 10% Chaps, 0.05% Tween-20) for 1 hour at 65ºC. Probes were diluted to 1 ng/µl in hybridization buffer and heated to 80ºC for 5 minutes. Retinas were incubated in probe solution in vials rotating on a nutator 65ºC overnight. **Day 2**: Retinas were washed with a mixture hybridization buffer and 2X SSC at the ratios 3:1, 1:1, 1:3 0:1 at 65ºC 15 minutes per wash. Retinas were then incubated in 0.2X SSC at 65ºC for one hour. Retinas were then washed in a mixture of 0.2X SSC and PBT at the ratios 3:1, 1:1, 1:3, 0:1, at room temperature 5 minutes per wash. Peroxidases were quenched with 0.1% sodium azide and 0.3% hydrogen peroxide for 45 minutes. Retinas were washed with PBT (1X PBS, 1% Triton-X) and removed from nylon mesh into individual wells of a 48 well plate. Retinas were blocked with 1% Roche block in PBT for 1 hour then incubated with 1:300 Anti-DIG-POD or Anti-FLU-POD 4ºC overnight. **Day 3**: After antibody incubation retinas were washed with PBT then the antibody was detected with Cy3 or Cy5 tyramide diluted 1:100 in amplification buffer then washed in PBT.

Immunohistochemistry

Immunohistochemistry of optic nerve cryo-sections was carried out using the following general procedure. Optic nerves were dissected from MS222 euthanized *X. laevis* and fixed in 4% MEM-PFA at 4ºC overnight then cryo-protected with 30% (w/v) sucrose in PBS at 4ºC overnight. Optic nerves were then embedded in cryo-molds in O.C.T. and stored at -80ºC. Cryo-sections were cut to 10-16 µm thickness and placed onto Tissue Tack slides and stored at -80ºC. **Day1:** Slides were washed in PBS, washed with PBT (PBS, 0.1-0.3% Triton-X, 0.1% BSA), blocked in 10% goat serum (NGS) then incubated with primary antibody diluted in PBT and 5% NGS at 4ºC overnight. **Day 2:** Slides were washed in PBT, incubated with secondary antibody diluted in PBT

and 5% NGS at room temperature for 30 minutes, then washed with PBT and PBS. Nuclei were labeled using 4',6-diamidino-2-phenylindole (DAPI).

The primary antibodies used were: Blbp (rabbit polyclonal, Abcam, 1:2000 or 1:500 if after *in situ* hybridization), Mbp [12] (rat monoclonal, Abcam, 1:300), Acetylated tubulin (mouse monoclonal, Abcam, 1:1500), Laminin (rabbit polyclonal, Fitzgerald, 1:200), pan Neurofascin NFC2 (rabbit polyclonal, gift of Peter Brophy, University of Edinburgh, 1:2500), GFP (chicken polyclonal, Aves, 1:1000), mCherry (mouse monoclonal, Clontech, 1:500), Cleaved Caspase-3 (Asp175 rabbit polyclonal, Cell Signaling Technology, 1:300), the 3A10 epitope (mouse monoclonal, DSHB, 1:400), *X. tropicalis* Sncg (rabbit polyclonal, custom-made Covance, 1:10,000). IB4 lectin-FITC (Sigma-Aldrich, 1:200 of 1mg/ml solution) was used together with primary antibodies. Secondary antibodies used were Alexa Fluor 488 goat-anti mouse IgG (Invitrogen), Alexa Fluor 647 goat-anti rabbit IgG, Cy3 goat-anti-rabbit IgG, Cy3 goat-anti rat IgG, and Cy5 goat anti-mouse (Jackson ImmunoResearch).

Generation of X. tropicalis gamma synuclein antibody

The Sncg antibody was generated through the company, Covance**.** A KHL conjugated peptide for the residues encoding the acidic C-terminus of *X. tropicalis* gamma synuclein, (CKK)-EATESTEQVGDGEN was generated and injected into 2 rabbits (#6395 and 6396), and the terminal bleed was affinity purified. The specificity of the antibody was confirmed using rabbit test bleeds for immunohistochemistry on wholemount retinas. Since #6396 was found to be more specific, this was the antibody used for all experiments using the Sncg antibody.

RGC counts

In situ hybridization for *rbpms* was performed on wholemount retinas from wild-type *X. laevis* at Stages 56, 58, 62 and animals expressing the Isl2: GFP-TRΔC transgene at Stage 56 and 62. Retinas were imaged at 20X as a mosaic using an automated script in IPLab on a Zeiss 200M inverted microscope using the *rbpms* signal as the focal plane reference. The number of *rbpms*

expressing cells in each imaged retina was counted using an automated segmentation based script in IPLab.

TUNEL assay

Wholemount retinas from wild-type and *X. laevis* expressing the Isl2: GFP-TRΔC transgene at Stage 62 were assayed for Terminal deoxynucleotidyl transferase dUTP nick end labeling (TUNEL) using the Apoptag Peroxidase In situ Apoptosis Detection Kit (Millipore). Retinas were washed in PBS, and then washed in PBT (PBS, 0.5% Triton-X). **Day 1:** Endogenous peroxidases were quenched with 0.1% Sodium azide 0.3% hydrogen peroxide for 45 minutes, then washed in PBT. Retinas were transferred to individual wells of a 48-well plate and incubate with 100 µl Equilibration buffer per retina for 5 minutes then incubate in TdT (56 µl reaction buffer, 24 µl TdT enzyme per retina) for 2 hours at 37ºC. Stop reaction with Stop wash buffer 40 minutes at 37ºC, wash in PBT, block in 1% Blocking reagent (Roche), and incubate in 1:300 Anti-DIG-POD antibody 4ºC overnight. **Day 2:** Wash retinas in PBT, detect DIG-POD antibody with Cy3 tyramide (Perkin Elmer) and wash with PBT and PBS. Nuclei were then labeled with DAPI. Retinas were imaged as mosaics at 20X using an automated script in IPLab on a Zeiss 200M inverted microscope using the DAPI signal in the RGC layer as the focal reference. TUNEL positive RGCs were identified and manually counted based on the presence of TUNEL signal co-localizing with DAPI signal from the RGC layer.

Internodal distance measurements

Longitudinal optic nerve 16 µm cryo-sections from wild-type *X. laevis* at Stages 58, 62, 66, and 4 weeks post-metamorphosis were immunolabeled with Neurofascin and 3A10. Longitudinal optic nerve 16 µm cryo-sections from transgenic *X. laevis* (Blbp: rtTA/TetOp: GFP-TRΔC, Isl2: GFP-TRΔC, Mbp: rtTA/ TetOp: GFP-TRΔC, Blbp: rtTA control) at Stage 62, and wild-type *X. laevis* at Stage 54 with or without 20 nM T3 induction were immunolabeled with

Neurofascin, 3A10, and Mbp. All optic nerve sections (n= 3-4 per Stage/genotype) were imaged at 60X on a FV1000 (Olympus) laser scanning confocal microscope a using a 0.45 micron z step. Maximum intensity projections were imported into Imaris software and the distance between Neurofascin immunolabeled paranodes along individual axons was measured using the measurement points tool. Due to the high density of axons in optic nerves of the wild-type 4 weeks post-metamorphic animals, accurate internodal distance measures could not be obtained.

Axon degeneration quantification

Axon markers that label preferentially myelinated axons were determined from confocal images of cross-sectional cryo-sections of wild-type *X. laevis* optic nerve at Stage 58 immunolabeled with Mbp, 3A10 and Sncg, or Mbp, Acetylated tubulin and Sncg acquired at 60X magnification with a 0.45 μm z-step (FV1000, Olympus). The signal from each channel was automatically segmented in IPLab and co-localization between segmented channels was calculated using Pearson's coefficient.

Confocal images of optic nerve cross-sectional cryo-sections from wild-type metamorphic *X. laevis* at Stages 58, 62 and 66, immunolabeled with 3A10, Mbp, and cleaved-caspase-3 were acquired at 60X magnification with a 0.45 μm z-step (FV1000, Olympus). The signal for each channel was segmented using IPLab software (Becton Dickinson). The total area for each segmented channel was measured. The area of degenerating myelinated axons was calculated by measuring the area of segmented cleaved-caspase-3 that overlapped with segmented MBP. Values were normalized to the total area of optic nerve cross-section measured.

Longitudinal 10 μm thick optic nerve cryo-sections from transgenic lines (Blbp: rtTA/ TetOp: GFP-TRΔC, Isl2: GFP-TRΔC, Mbp: rtTA/TetOp: GFP-TRΔC) and their respective controls (Blbp: rtTA not induced with doxycycline, wild-type, Mbp: rtTA not induced with doxycycline) at Stage 62 were immunolabeled with cleaved-caspase-3 and Mbp. The entire length of each optic nerve (n= 5 per transgene) was imaged at 20X on a Zeiss 200M inverted

microscope as a mosaic and the amount of cleaved-caspase-3 signal was quantified using an automated segmentation based script in IPLab and normalized to total area measured.

Microglia quantification

Longitudinal 10 μm optic nerve cryo-sections immunolabeled with IB4 lectin-FITC, laminin, and DAPI, were imaged by fluorescence at 20X for wild-type *X. laevis* optic nerves at Stages 58, 62 and 66, three days following unilateral optic nerve transection in Stage 60 animals, and in the transgenic lines (Blbp: rtTA/TetOp: GFP-TRΔC, Isl2: GFP-TRΔC, Mbp: rtTA/TetOp: GFP-TRΔC, Blbp: Megf11ΔC-GFP, Blbp: Mfge8-D91E-mCherry, Blbp: rtTA/TetOp: GFP-Rac1N17) along with their respective controls (Blbp: rtTA/TRΔC not induced, wild-type, Mbp: rtTA/TRΔC not induced, wild-type, Blbp: Mfge8-mCherry, Blbp: rtTA/Rac1N17 not induced). The optic nerves were imaged as mosaics, such that the entire length of the longitudinal optic nerve section was imaged. The boundaries of the laminin-labeled optic nerve sheath were manually traced and IB4 lectin-FITC cells that co-localized with DAPI were traced and segmented. The amount of segmented IB4 signal within the optic nerve parenchyma and optic nerve sheath were quantified using a multiple-segmentation script written in IPLab which analyzes fluorescence intensities over a wide range of segmentation values (Nguyen et al., 2011). The values were normalized to the amount of optic nerve parenchyma or sheath area measured.

OPC and oligodendrocyte quantification

Longitudinal 10 μm thick optic nerve cryo-sections from wild-type Stage 58, 62 and 66 *X. laevis* and transgenic lines expressing Mbp: rtTA/TetOp: GFP-TRΔC or Blbp: rtTA/TetOp: GFP-TRΔC (along with control nerves from same line that had not been induced with doxycycline) were used for *in situ* hybridization. Riboprobes were used for *pdgfrα* (DIG) to identify OPCs and *plp* (FLU) to identify mature oligodendrocytes. For the wild-type study 16-20 optic nerve images, corresponding to approximately four images per nerve (averaged during

quantification) were captured at 20X magnification on Zeiss 200M inverted microscope. For the Mbp and Blbp studies, four consecutive images were captured per optic nerve, which were averaged following quantification. *Pdgfrα* and *plp* expressing cells were manually traced based on co-localization with nuclear marker DAPI and counted using an automated script in IPLab.

Mbp/Sncg debris quantification

Confocal images of Mbp, Sncg and 3A10 immunolabeled optic nerve longitudinal 16 μm thick cryo-sections taken at 20X magnification with a 1 μm z-step (FV1000, Olympus) were imported into Imaris software (Bitplane).The immunohistochemistry used a PBT buffer with 0.3% Triton-X. In Imaris, a surface of the 3A10 channel was created at 50% of threshold intensity. This surface was used to mask the Mbp and Sncg channels channel. An outside mask produced a channels of Mbp or Sncg co-localizing with 3A10 and an inside mask produced a channels of MBP or Sncg that did not co-localize with 3A10. Surfaces were created from the new Mbp channels using a threshold of 550 and filter of 550 and from the new Sncg channels using a threshold of 650 and filter of 650. Ratios of the volume of MBP outside of axons to total volume of MBP were calculated using Excel software.

Thyroid hormone receptor dominant negative validation

Fluorescence microscope images of retinas or longitudinal 10 μm thick optic nerve cryo-sections from Stage 54 wild-type or TRΔC transgenic lines (Blbp: rtTA/TetOp: GFP-TRΔC, Isl2: GFP-TRΔC, Mbp: rtTA/ TetOp: GFP-TRΔC) after treatment with T3 were taken at 20X magnification on a Zeiss 200M inverted microscope following double fluorescence *in situ* hybridization. Retinas were labeled by riboprobes for *gene 12* (DIG) and the RGC marker *rbpms* (FLU), while optic nerves were labeled by riboprobes for *gene 12* (DIG) and the oligodendrocyte marker *plp* (FLU) or OPC marker *pdgfrα* (FLU). The entire retinas and optic nerve sections were imaged by creating mosaics. For retinas, three consecutive sections were imaged per retina and

averaged following quantification to overcome inconsistencies of tyramide labeling between sections. Retina images were then quantified using a multiple-segmentation based script written in IPLab, using the *rbpms* signal to create a mask to distinguish the up-regulation of *gene 12* inside and outside RGC. Optic nerves were quantified using the same multiple-segmentation based script but used the quantified the overall level of *gene 12* signal in the nerve, normalized to area.

Phagocytic gene expression

In situ hybridization using the DIG-dUTP labeled riboprobes for the *Xenopus* genes: *abca, crkII, dock1, elmo1, gulp, lrp1, itgβ3, itgβ5, megf10, megf11, mfge8, rac1* was performed on 10 μm thick longitudinal optic nerve cryo-sections from wild-type and Blbp: rtTA/TetOp: GFP-TRΔC Stage 62 *X. laevis*. On Day1 of the *in situ* hybridization procedure the slides were treated with 10 μg/mL Proteinase K for 2 minutes. Following the *in situ* hybridization procedure, immunohistochemistry for Blbp was performed on the slides. Optic nerve sections were imaged at 20X magnification on a Zeiss 200M inverted microscope.

Transgenic fluorescent reporters in astrocytes

Fluorescence microscopy images of cross-sectional cryo-sections from Blbp:Mfge8-mCherry, Blbp:Mfge8D91E-mCherry, Blbp:CD63-mCherry, or Blbp: hA-AMB-mCherry animals at Stages 58, 62, and 66 immunolabeled with mCherry and Blbp antibodies were acquired at 20X magnification on a Zeiss 200M inverted microscope. The area of mCherry signal in the images was quantified using a multiple-segmentation script in IPLab. Values were normalized to the total area of optic nerve measured. The values graphed are for the segmentation value that most closely approximates the mean difference of all segmentation values that reached that same minimal p-value through a Student's t-test.

Electron microscopy and image tracing

Optic nerves were dissected in fixative (2% paraformaldehyde, 2.5% glutaraldehyde, 3mM $CaCl_2$, 0.15 M Sodium cacodylate), post-fixed 4ºC overnight, and processed for SBEM. Washes were carried out in small glass vials. Optic nerves were kept attached throughout processing in order to maintain orientation and separated from the eye for embedding. Optic nerves were washed in 0.1M Sodium cacodylate on ice then fixed in 2% Osmium tetroxide, 1.5% Potassium ferrocyanide for 1 hour at room temperature. Tissue was washed distilled water (ddH_2O) then incubated with filtered 1% Thiocarbohydrazide for 20 minutes, washed in ddH_2O, fixed with 2% Osmium tetroxide 30 minutes, and washed in ddH_2O. They were incubated in 1% Uranyl acetate 4ºC overnight. Tissues were washed with ddH_2O, incubated with filtered Lead aspartate (0.66g Lead nitrate in 10 mL L-Aspartic acid (0.998 g L-aspartic acid in 250 mL ddH_2O pH 3.8) pH 5.5) at 60ºC 30 minutes, and washed with ddH_2O. Tissue was dehydrated with a series of ethanol washes: 50%, 70%, 90%, 100%, and 100% ethanol on ice. Tissues was washed with 100% acetone and infiltrated with Durcupan resin (Sigma) using diluted in acetone at 25%, 50%, 75%, 100%. Tissue in 100% Durcupan resin was placed under vacuum prior to embedding in molds and baking 60ºC.

For the initial characterization of metamorphic changes, the ONs from six wild-type *X. laevis* each at NF Stages 58, 62, 66, and 4 weeks post-metamorphosis were processed. For the transgenic perturbation studies, four animals each at Stage 62 and Stg. 66 for each of the transgenic lines, including the two transgenic controls (Blbp: gap43-mCherry and Isl2: hA-AMB-mCherry) were processed for TEM. The lengths of the ONs were measured at the time of dissection. One optic nerve of the wild-type animals for each of Stages 58, 62, 66 and 4 weeks post-metamorphosis was sectioned in a longitudinal orientation and processed by SBEM. All other optic nerves were sectioned in a cross-sectional orientation.

Optic nerve cross-sectional area was measured in 1 μm semi-thin cross-sections. For TEM, 60-90 nm cross-sections were placed on formvar-coated copper grids, and imaged at

5000X magnification with a H7600 transmission electron microscope (Hitachi); each optic nerve was imaged as ten generally non-overlapping images spanning all areas of the optic nerve. For SBEM imaging, samples were imaged on an FEI Quanta 200 (Stage 62), Zeiss Sigma (Stages 58 and 66) or Zeiss Merlin (juvenile frog) SEM equipped with a Gatan 3View unit. Microtome slices were 70 nm thick. Images were aligned by cross-correlation using IMOD (Kremer et al., 1996) prior to segmentation.

Manual tracing of the axoplasm, outer myelin sheath and focal peri-axonal space enlargements per myelinated axon as well as the debris myelin was carried out for ten micrographs per optic nerve in a blinded-fashion, and images were quantified using IPLab (Becton Dickinson) custom scripts. Debris myelin was subsequently sub-classified as being partially attached to the sheath, enwrapped by lamellar processes, fully within a phagocyte, or a transition between classes. To extrapolate myelin inner diameter for the calculation of G'-ratios, the areas of the axoplasm and peri-axonal spaces were subtracted from the area bounded by the myelin sheath for each axon. For the measurements of myelin area, myelin was automatically segmented based on it being the most-electron dense structure in the micrographs, using the mean and standard deviation of the manually traced myelin segments to automatically tailor the segmentation cut-offs to different micrographs.

Optic nerve volumes obtained from 3View SBEM processing were imported into IMOD. Individual myelinated axons were selected for tracing by the presence of nodes, except in the case of Stage 58 optic nerves, where the internodal distance exceeded the dimensions of the volume, and manually traced. Surface areas and volumes of traced objects (axoplasm, peri-axonal space vacuoles, and outer myelin membrane) were calculated in IMOD. Internodal distance measurements were obtained by importing IMOD traced model files into Imaris (Bitplane) followed by use of the Measurement Points tool.

Statistical Analysis

Statistical analysis involved the comparison of means using t-tests or single variable ANOVAs using Graphpad (Graphpad software) and Brightstat (Stricker, 2008). With the exception of the transgenic TEM analysis, pairwise comparisons were performed using Tukey's test when variance between the groups was equal or the Games-Howell test when variance was unequal, as determined by the Bartlett's test for equal variance. The pairwise comparisons between the control transgenic and experimental transgenic lines for the transgenic TEM analysis were performed using the Dunnett's test when variance was equal or the Games-Howell test when variance was unequal. The control transgenic group consisted of optic nerves obtained from 2 lines of transgenic animals expressing red fluorescent reporter genes (Blbp: ctgap43-mCherry and Isl2: hA-AMB-mCherry). All statistical comparisons were performed using all of the transgenic lines, although only the statistically significant comparisons against the control group are shown. Since Stages 62 and 66 differed in many parameters in wild-type animals, analyses of transgenic animals was separated by stage, such that all of the optic nerves from experimental Stage 62 transgenic animals were compared to the Stage 62 transgenic controls, and all of the optic nerves from experimental Stage 66 transgenic animals were compared to the Stage 66 transgenic controls. Since the internodal distances calculated in the Stage 58 SBEM traced axons were not actual values but rather minimum values due to the size of the Stage 58 acquired volume, the non-parametric Kruskal-Wallis test was used to compare segment SBEM-based segment lengths in Figure 2F. All graphs depict mean ± SD. Statistical significance was defined as $P < 0.05$.

References

Adlkofer, K., Martini, R., Aguzzi, A., Zielasek, J., Toyka, K.V., and Suter, U. (1995). Hypermyelination and demyelinating peripheral neuropathy in Pmp22-deficient mice. Nature genetics *11*, 274-280.

Akakura, S., Singh, S., Spataro, M., Akakura, R., Kim, J.I., Albert, M.L., and Birge, R.B. (2004). The opsonin MFG-E8 is a ligand for the alphavbeta5 integrin and triggers DOCK180-dependent Rac1 activation for the phagocytosis of apoptotic cells. Experimental cell research *292*, 403-416.

Almeida, R.G., Czopka, T., and Lyons, D.A. (2011). Individual axons regulate the myelinating potential of single oligodendrocytes in vivo. Development *138*, 4443-4450.

Amaya, E., and Kroll, K.L. (1999). A method for generating transgenic frog embryos. Methods in molecular biology *97*, 393-414.

Anderson, G.W. (2001). Thyroid hormones and the brain. Frontiers in neuroendocrinology *22*, 1-17.

Auluck, P.K., Caraveo, G., and Lindquist, S. (2010). α-Synuclein: membrane interactions and toxicity in Parkinson's disease. Annual review of cell and developmental biology *26*, 211-233.

Awasaki, T., Tatsumi, R., Takahashi, K., Arai, K., Nakanishi, Y., Ueda, R., and Ito, K. (2006). Essential role of the apoptotic cell engulfment genes draper and ced-6 in programmed axon pruning during Drosophila metamorphosis. Neuron *50*, 855-867.

Baas, D., Bourbeau, D., Sarlieve, L.L., Ittel, M.E., Dussault, J.H., and Puymirat, J. (1997). Oligodendrocyte maturation and progenitor cell proliferation are independently regulated by thyroid hormone. Glia *19*, 324-332.

Baas, D., Legrand, C., Samarut, J., and Flamant, F. (2002). Persistence of oligodendrocyte precursor cells and altered myelination in optic nerve associated to retina degeneration in mice devoid of all thyroid hormone receptors. Proc Natl Acad Sci U S A *99*, 2907-2911.

Bakhti, M., Snaidero, N., Schneider, D., Aggarwal, S., Mobius, W., Janshoff, A., Eckhardt, M., Nave, K.A., and Simons, M. (2013). Loss of electrostatic cell-surface repulsion mediates myelin membrane adhesion and compaction in the central nervous system. Proc Natl Acad Sci U S A *110*, 3143-3148.

Barradas, P.C., Vieira, R.S., and De Freitas, M.S. (2001). Selective effect of hypothyroidism on expression of myelin markers during development. J Neurosci Res *66*, 254-261.

Bartzokis, G., Lu, P.H., Tingus, K., Mendez, M.F., Richard, A., Peters, D.G., Oluwadara, B., Barrall, K.A., Finn, J.P., Villablanca, P.*, et al.* (2010). Lifespan trajectory of myelin integrity and maximum motor speed. Neurobiology of aging *31*, 1554-1562.

Bassett, J.H., Harvey, C.B., and Williams, G.R. (2003). Mechanisms of thyroid hormone receptor-specific nuclear and extra nuclear actions. Molecular and cellular endocrinology *213*, 1-11.

Baumann, N., and Pham-Dinh, D. (2001). Biology of oligodendrocyte and myelin in the mammalian central nervous system. Physiol Rev *81*, 871-927.

Bechmann, I., and Nitsch, R. (1997). Astrocytes and microglial cells incorporate degenerating fibers following entorhinal lesion: A light, confocal, and electron microscopical study using a phagocytosis-dependent labeling technique. Glia *20*, 145-154.

Beisiegel, U., Weber, W., Ihrke, G., Herz, J., and Stanley, K.K. (1989). The LDL-receptor-related protein, LRP, is an apolipoprotein E-binding protein. Nature *341*, 162-164.

Bendik, I., and Pfahl, M. (1995). Similar ligand-induced conformational changes of thyroid hormone receptors regulate homo- and heterodimeric functions. The Journal of biological chemistry *270*, 3107-3114.

Benediktsson, A.M., Schachtele, S.J., Green, S.H., and Dailey, M.E. (2005). Ballistic labeling and dynamic imaging of astrocytes in organotypic hippocampal slice cultures. Journal of neuroscience methods *141*, 41-53.

Berry, D.L., Rose, C.S., Remo, B.F., and Brown, D.D. (1998). The expression pattern of thyroid hormone response genes in remodeling tadpole tissues defines distinct growth and resorption gene expression programs. Developmental biology *203*, 24-35.

Berthold, C.H., and Nilsson, I. (1987). Redistribution of Schwann cells in developing feline L7 ventral spinal roots. Journal of neurocytology *16*, 811-828.

Berthold, C.H., Nilsson, I., and Rydmark, M. (1983). Axon diameter and myelin sheath thickness in nerve fibres of the ventral spinal root of the seventh lumbar nerve of the adult and developing cat. J Anat *136*, 483-508.

Bignami, A., and Ralston, H.J., 3rd (1969). The cellular reaction to Wallerian degeneration in the central nervous system of the cat. Brain research *13*, 444-461.

Billon, N., Jolicoeur, C., Tokumoto, Y., Vennstrom, B., and Raff, M. (2002). Normal timing of oligodendrocyte development depends on thyroid hormone receptor alpha 1 (TRalpha1). EMBO J *21*, 6452-6460.

Bishop, D.L., Misgeld, T., Walsh, M.K., Gan, W.-B., and Lichtman, J.W. (2004). Axon Branch Removal at Developing Synapses by Axosome Shedding. Neuron *44*, 651-661.

Boison, D., Bussow, H., D'Urso, D., Muller, H., and Stoffel, W. (1995). Adhesive properties of proteolipid protein are responsible for the compaction of CNS myelin sheaths. The Journal of neuroscience *15*, 5502-5513.

Boron, W.F. (2003). Synthesis of thyroid hormones. In Medical Physiology: A Cellular and Molecular Approach (Elsevier/Saunders), p. p. 1300.

Brady, S.T., Witt, A.S., Kirkpatrick, L.L., de Waegh, S.M., Readhead, C., Tu, P.H., and Lee, V.M. (1999). Formation of compact myelin is required for maturation of the axonal cytoskeleton. The Journal of neuroscience : the official journal of the Society for Neuroscience *19*, 7278-7288.

Brand, M., Heisenberg, C.P., Jiang, Y.J., Beuchle, D., Lun, K., Furutani-Seiki, M., Granato, M., Haffter, P., Hammerschmidt, M., Kane, D.A., *et al.* (1996). Mutations in zebrafish genes affecting the formation of the boundary between midbrain and hindbrain. Development *123*, 179-190.

Brenner, M., Johnson, A.B., Boespflug-Tanguy, O., Rodriguez, D., Goldman, J.E., and Messing, A. (2001). Mutations in GFAP, encoding glial fibrillary acidic protein, are associated with Alexander disease. Nat Genet *27*, 117-120.

Brill, M.H., Waxman, S.G., Moore, J.W., and Joyner, R.W. (1977). Conduction velocity and spike configuration in myelinated fibres: computed dependence on internode distance. Journal of neurology, neurosurgery, and psychiatry *40*, 769-774.

Buchholz, D.R., Hsia, S.C., Fu, L., and Shi, Y.B. (2003). A dominant-negative thyroid hormone receptor blocks amphibian metamorphosis by retaining corepressors at target genes. Molecular and cellular biology *23*, 6750-6758.

Buchholz, D.R., Tomita, A., Fu, L., Paul, B.D., and Shi, Y.B. (2004). Transgenic analysis reveals that thyroid hormone receptor is sufficient to mediate the thyroid hormone signal in frog metamorphosis. Molecular and cellular biology *24*, 9026-9037.

Burd, G.D. (1991). Development of the olfactory nerve in the African clawed frog, Xenopus laevis: I. Normal development. J Comp Neurol *304*, 123-134.

Burggren, W.W., and West, N.H. (1982). Changing respiratory importance of gills, lungs and skin during metamorphosis in the bullfrog Rana catesbeiana. Respiration physiology *47*, 151-164.

Cahoy, J.D., Emery, B., Kaushal, A., Foo, L.C., Zamanian, J.L., Christopherson, K.S., Xing, Y., Lubischer, J.L., Krieg, P.A., Krupenko, S.A., *et al.* (2008). A transcriptome database for astrocytes, neurons, and oligodendrocytes: a new resource for understanding brain development and function. The Journal of neuroscience : the official journal of the Society for Neuroscience *28*, 264-278.

Cai, Z., Cash, K., Swift, J., Sutton-Smith, P., Robinson, M., Thompson, P.D., and Blumbergs, P.C. (2001). Focal myelin swellings and tomacula in anti-MAG IgM paraproteinaemic neuropathy: novel teased nerve fiber studies. Journal of the peripheral nervous system : JPNS *6*, 95-101.

Cao, H.J., Lin, H.Y., Luidens, M.K., Davis, F.B., and Davis, P.J. (2009). Cytoplasm-to-nucleus shuttling of thyroid hormone receptor-beta1 (Trbeta1) is directed from a plasma membrane integrin receptor by thyroid hormone. Endocrine research *34*, 31-42.

Cao, X., Kambe, F., Moeller, L.C., Refetoff, S., and Seo, H. (2005). Thyroid hormone induces rapid activation of Akt/protein kinase B-mammalian target of rapamycin-p70S6K cascade through phosphatidylinositol 3-kinase in human fibroblasts. Molecular endocrinology (Baltimore, Md) *19*, 102-112.

Carenini, S., Montag, D., Cremer, H., Schachner, M., and Martini, R. (1996). Absence of the myelin-associated glycoprotein (MAG) and the neural cell adhesion molecule (N-CAM)

interferes with the maintenance, but not with the formation of peripheral myelin. Cell and tissue research *287*, 3-9.

Castellano, F., Montcourrier, P., and Chavrier, P. (2000). Membrane recruitment of Rac1 triggers phagocytosis. J Cell Sci *113 (Pt 17)*, 2955-2961.

Chen, Y., and Swanson, R.A. (2003). Astrocytes and brain injury. Journal of Cerebral Blood Flow & Metabolism *23*, 137-149.

Cheng, S.-Y., Leonard, J.L., and Davis, P.J. (2010). Molecular aspects of thyroid hormone actions. Endocrine reviews *31*, 139-170.

Cheng, S.M., and Carr, C.E. (2007). Functional delay of myelination of auditory delay lines in the nucleus laminaris of the barn owl. Developmental neurobiology *67*, 1957-1974.

Chimini, G., and Chavrier, P. (2000). Function of Rho family proteins in actin dynamics during phagocytosis and engulfment. Nature cell biology *2*, E191-196.

Chomiak, T., and Hu, B. (2009). What is the optimal value of the g-ratio for myelinated fibers in the rat CNS? A theoretical approach. PLoS One *4*, e7754.

Chung, S.H., Keating, M.J., and Bliss, T.V. (1974). Functional synaptic relations during the development of the retino-tectal projection in amphibians. Proc R Soc Lond B Biol Sci *187*, 449-459.

Chung, S.H., Stirling, R.V., and Gaze, R.M. (1975). The structural and functional development of the retina in larval Xenopus. J Embryol Exp Morphol *33*, 915-940.

Chung, W.S., Clarke, L.E., Wang, G.X., Stafford, B.K., Sher, A., Chakraborty, C., Joung, J., Foo, L.C., Thompson, A., Chen, C.*, et al.* (2013). Astrocytes mediate synapse elimination through MEGF10 and MERTK pathways. Nature *504*, 394-400.

Cima, C., and Grant, P. (1982a). Development of the optic nerve in Xenopus laevis. I. Early development and organization. J Embryol Exp Morphol *72*, 225-249.

Cima, C., and Grant, P. (1982b). Development of the optic nerve in Xenopus laevis. II. Gliogenesis, myelination and metamorphic remodelling. J Embryol Exp Morphol *72*, 251-267.

Clarke, L.E., and Barres, B.A. (2013). Glia keep synapse distribution under wraps. Cell *154*, 267-268.

Coetzee, T., Suzuki, K., Nave, K.-A., and Popko, B. (1999). Myelination in the Absence of Galactolipids and Proteolipid Proteins. Molecular and Cellular Neuroscience *14*, 41-51.

Colavincenzo, J., and Levine, R.L. (2000). Myelin debris clearance during Wallerian degeneration in the goldfish visual system. J Neurosci Res *59*, 47-62.

Cole, J.S., Messing, A., Trojanowski, J.Q., and Lee, V.M. (1994). Modulation of axon diameter and neurofilaments by hypomyelinating Schwann cells in transgenic mice. The Journal of neuroscience : the official journal of the Society for Neuroscience *14*, 6956-6966.

Corty, M.M., and Freeman, M.R. (2013). Cell biology in neuroscience: Architects in neural circuit design: glia control neuron numbers and connectivity. J Cell Biol *203*, 395-405.

Court, F.A., Sherman, D.L., Pratt, T., Garry, E.M., Ribchester, R.R., Cottrell, D.F., Fleetwood-Walker, S.M., and Brophy, P.J. (2004). Restricted growth of Schwann cells lacking Cajal bands slows conduction in myelinated nerves. Nature *431*, 191-195.

Cullen, M.J., and Webster, H.D. (1979). Remodelling of optic nerve myelin sheaths and axons during metamorphosis in Xenopus laevis. J Comp Neurol *184*, 353-362.

Cuzner, M.L., Davison, A.-N., and Gregson, N.-A. (1965). The chemical composition of vertebrate myelin and microsomes. Journal of neurochemistry *12*, 469-481.

Das, B., and Brown, D.D. (2004). Controlling transgene expression to study Xenopus laevis metamorphosis. Proc Natl Acad Sci U S A *101*, 4839-4842.

Das, B., Schreiber, A.M., Huang, H., and Brown, D.D. (2002). Multiple thyroid hormone-induced muscle growth and death programs during metamorphosis in Xenopus laevis. Proc Natl Acad Sci U S A *99*, 12230-12235.

Davis, P.J., and Davis, F.B. (2002). Nongenomic actions of thyroid hormone on the heart. Thyroid *12*, 459-466.

Davis, P.J., Leonard, J.L., and Davis, F.B. (2008). Mechanisms of nongenomic actions of thyroid hormone. Frontiers in neuroendocrinology *29*, 211-218.

Dawson, M.R., Polito, A., Levine, J.M., and Reynolds, R. (2003). NG2-expressing glial progenitor cells: an abundant and widespread population of cycling cells in the adult rat CNS. Molecular and Cellular Neuroscience *24*, 476-488.

Deerinck, T.J., Bushong, E.A., Thor, A., and Ellisman, M.H. (2010). NCMIR methods for 3D EM: a new protocol for preparation of biological specimens for serial block face scanning electron microscopy. Microscopy, 6-8.

Di Rocco, M., Biancheri, R., Rossi, A., Filocamo, M., and Tortori-Donati, P. (2004). Genetic disorders affecting white matter in the pediatric age. American journal of medical genetics Part B, Neuropsychiatric genetics : the official publication of the International Society of Psychiatric Genetics *129B*, 85-93.

Dupree, J.L., Coetzee, T., Blight, A., Suzuki, K., and Popko, B. (1998). Myelin galactolipids are essential for proper node of Ranvier formation in the CNS. The Journal of neuroscience : the official journal of the Society for Neuroscience *18*, 1642-1649.

Emery, B. (2010). Regulation of oligodendrocyte differentiation and myelination. Science *330*, 779-782.

Etkin, W. (1963). Metamorphosis-Activating System of the Frog: Thyroid hormone feedback matures the neurosecretory mechanism, coordinates the phases of metamorphosis. Science *139*, 810-814.

Fadok, V.A., Bratton, D.L., Frasch, S.C., Warner, M.L., and Henson, P.M. (1998). The role of phosphatidylserine in recognition of apoptotic cells by phagocytes. Cell death and differentiation *5*, 551-562.

Farsetti, A., Mitsuhashi, T., Desvergne, B., Robbins, J., and Nikodem, V.M. (1991). Molecular basis of thyroid hormone regulation of myelin basic protein gene expression in rodent brain. The Journal of biological chemistry *266*, 23226-23232.

Feig, L.A., and Cooper, G.M. (1988). Relationship among guanine nucleotide exchange, GTP hydrolysis, and transforming potential of mutated ras proteins. Molecular and cellular biology *8*, 2472-2478.

Feldman, J.D., and Gaze, R.M. (1972). The growth of the retina in Xenopus laevis: an autoradiographic study. II. Retinal growth in compound eyes. J Embryol Exp Morphol *27*, 381-387.

Feng, B., and Tabas, I. (2002). ABCA1-mediated cholesterol efflux is defective in free cholesterol-loaded macrophages. Mechanism involves enhanced ABCA1 degradation in a process requiring full NPC1 activity. The Journal of biological chemistry *277*, 43271-43280.

Fields, R.D. (2008). White matter in learning, cognition and psychiatric disorders. Trends in neurosciences *31*, 361-370.

Filbin, M.T. (2003). Myelin-associated inhibitors of axonal regeneration in the adult mammalian CNS. Nature reviews Neuroscience *4*, 703-713.

Filbin, M.T., Zhang, K., Li, W., and Gao, Y. (1999). Characterization of the effect on adhesion of different mutations in myelin P0 protein. Annals of the New York Academy of Sciences *883*, 160-167.

Finnemann, S.C., Bonilha, V.L., Marmorstein, A.D., and Rodriguez-Boulan, E. (1997). Phagocytosis of rod outer segments by retinal pigment epithelial cells requires alpha(v)beta5 integrin for binding but not for internalization. Proc Natl Acad Sci U S A *94*, 12932-12937.

Flamant, F., and Samarut, J. (2003). Thyroid hormone receptors: lessons from knockout and knock-in mutant mice. Trends in endocrinology and metabolism: TEM *14*, 85-90.

Fondell, J.D., Roy, A.L., and Roeder, R.G. (1993). Unliganded thyroid hormone receptor inhibits formation of a functional preinitiation complex: implications for active repression. Genes & development *7*, 1400-1410.

Fraher, J.P. (1992). Myelin-Axon Relationships in the Rat Phrenic-Nerve - Longitudinal Variation and Lateral Asymmetry. Journal of Comparative Neurology *323*, 551-557.

Fraher, J.P., and O'Sullivan, A.W. (2000). Interspecies variation in axon-myelin relationships. Cells Tissues Organs *167*, 206-213.

Franson, P. (1985). Quantitative electron microscopic observations on the non-neuronal cells and lipid droplets in the posterior funiculus of the cat after dorsal rhizotomy. J Comp Neurol *231*, 490-499.

Fried, K., and Hildebrand, C. (1982). Qualitative structural development of the feline inferior alveolar nerve. J Anat *134*, 517-531.

Fried, K., Hildebrand, C., and Erdelyi, G. (1982). Myelin sheath thickness and internodal length of nerve fibres in the developing feline inferior alveolar nerve. J Neurol Sci *54*, 47-57.

Friede, R.L., Brzoska, J., and Hartmann, U. (1985). Changes in myelin sheath thickness and internode geometry in the rabbit phrenic nerve during growth. J Anat *143*, 103-113.

Friede, R.L., and Miyagishi, T. (1972). Adjustment of the myelin sheath to changes in axon caliber. Anat Rec *172*, 1-14.

Friede, R.L., and Samorajski, T. (1967). Relation between the number of myelin lamellae and axon circumference in fibers of vagus and sciatic nerves of mice. J Comp Neurol *130*, 223-231.

Fuller, A.D., and Van Eldik, L.J. (2008). MFG-E8 regulates microglial phagocytosis of apoptotic neurons. Journal of neuroimmune pharmacology : the official journal of the Society on NeuroImmune Pharmacology *3*, 246-256.

Furuhashi, M., and Hotamisligil, G.S. (2008). Fatty acid-binding proteins: role in metabolic diseases and potential as drug targets. Nature reviews Drug discovery *7*, 489.

García-Matas, S., Gutierrez-Cuesta, J., Coto-Montes, A., Rubio-Acero, R., Díez-Vives, C., Camins, A., Pallàs, M., Sanfeliu, C., and Cristòfol, R. (2008). Dysfunction of astrocytes in senescence-accelerated mice SAMP8 reduces their neuroprotective capacity. Aging cell *7*, 630-640.

Garcia, D.M., and Koke, J.R. (2009). Astrocytes as gate-keepers in optic nerve regeneration--a mini-review. Comparative biochemistry and physiology Part A, Molecular & integrative physiology *152*, 135-138.

Gaultier, A., Wu, X., Le Moan, N., Takimoto, S., Mukandala, G., Akassoglou, K., Campana, W.M., and Gonias, S.L. (2009). Low-density lipoprotein receptor-related protein 1 is an essential receptor for myelin phagocytosis. J Cell Sci *122*, 1155-1162.

Gaze, R.M., and Peters, A. (1961). The development, structure and composition of the optic nerve of Xenopus laevis (Daudin). Q J Exp Physiol Cogn Med Sci *46*, 299-309.

Ge, W.P., Miyawaki, A., Gage, F.H., Jan, Y.N., and Jan, L.Y. (2012). Local generation of glia is a major astrocyte source in postnatal cortex. Nature *484*, 376-380.

Gerber, W.V., Yatskievych, T.A., Antin, P.B., Correia, K.M., Conlon, R.A., and Krieg, P.A. (1999a). The RNA-binding protein gene, hermes, is expressed at high levels in the developing heart. Mechanisms of Development *80*, 77-86.

Gerber, W.V., Yatskievych, T.A., Antin, P.B., Correia, K.M., Conlon, R.A., and Krieg, P.A. (1999b). The RNA-binding protein gene, hermes, is expressed at high levels in the developing heart. Mech Dev *80*, 77-86.

Gilbert, L.I., Tata, J.R., and Atkinson, B.G., eds. (1996). Metamorphosis: Postembryronic reprogramming of gene expression in amphibian and insect cells. (San Diego: Academic Press).

Gilbert, S.F. (2000). Metamorphosis: The Hormonal Reactivation of Development. In Developmental biology (Sunderland (MA): Sinauer Associates).

Gitik, M., Liraz-Zaltsman, S., Oldenborg, P.A., Reichert, F., and Rotshenker, S. (2011). Myelin down-regulates myelin phagocytosis by microglia and macrophages through interactions between CD47 on myelin and SIRPalpha (signal regulatory protein-alpha) on phagocytes. Journal of neuroinflammation *8*, 24.

Gledhill, R.F., and McDonald, W.I. (1977). Morphological characteristics of central demyelination and remyelination: a single-fiber study. Annals of neurology *1*, 552-560.

Goebbels, S., Oltrogge, J.H., Kemper, R., Heilmann, I., Bormuth, I., Wolfer, S., Wichert, S.P., Mobius, W., Liu, X., Lappe-Siefke, C.*, et al.* (2010). Elevated phosphatidylinositol 3,4,5-trisphosphate in glia triggers cell-autonomous membrane wrapping and myelination. The Journal of neuroscience : the official journal of the Society for Neuroscience *30*, 8953-8964.

Goodbrand, I.A., and Gaze, R.M. (1991). Microglia in tadpoles of Xenopus laevis: normal distribution and the response to optic nerve injury. Anat Embryol (Berl) *184*, 71-82.

Grant, P., Rubin, E., and Cima, C. (1980). Ontogeny of the retina and optic nerve in Xenopus laevis. I. Stages in the early development of the retina. J Comp Neurol *189*, 593-613.

Grant, S., and Keating, M.J. (1986). Ocular migration and the metamorphic and postmetamorphic maturation of the retinotectal system in Xenopus laevis: an autoradiographic and morphometric study. J Embryol Exp Morphol *92*, 43-69.

Griffin, J.W., George, R., Lobato, C., Tyor, W.R., Yan, L.C., and Glass, J.D. (1992). Macrophage responses and myelin clearance during Wallerian degeneration: relevance to immune-mediated demyelination. Journal of neuroimmunology *40*, 153-165.

Gumienny, T.L., Brugnera, E., Tosello-Trampont, A.C., Kinchen, J.M., Haney, L.B., Nishiwaki, K., Walk, S.F., Nemergut, M.E., Macara, I.G., Francis, R.*, et al.* (2001). CED-12/ELMO, a novel member of the CrkII/Dock180/Rac pathway, is required for phagocytosis and cell migration. Cell *107*, 27-41.

Hadas, S., Spira, M., Hanisch, U.K., Reichert, F., and Rotshenker, S. (2012). Complement receptor-3 negatively regulates the phagocytosis of degenerated myelin through tyrosine kinase Syk and cofilin. Journal of neuroinflammation *9*, 166.

Hall, A., Giese, N.A., and Richardson, W.D. (1996). Spinal cord oligodendrocytes develop from ventrally derived progenitor cells that express PDGF alpha-receptors. Development *122*, 4085-4094.

Halpern, J., and Hinkle, P.M. (1982). Evidence for an active step in thyroid hormone transport to nuclei: drug inhibition of L-125I-triiodothyronine binding to nuclear receptors in rat pituitary tumor cells. Endocrinology *110*, 1070-1072.

Hamon, Y., Trompier, D., Ma, Z., Venegas, V., Pophillat, M., Mignotte, V., Zhou, Z., and Chimini, G. (2006). Cooperation between engulfment receptors: the case of ABCA1 and MEGF10. PLoS One *1*, e120.

Hanayama, R., Tanaka, M., Miwa, K., Shinohara, A., Iwamatsu, A., and Nagata, S. (2002). Identification of a factor that links apoptotic cells to phagocytes. Nature *417*, 182-187.

Higgs, D.M., and Burd, G.D. (2001). Neuronal turnover in the Xenopus laevis olfactory epithelium during metamorphosis. Journal of Comparative Neurology *433*, 124-130.

Hörlein, A.J., Näär, A.M., Heinzel, T., Torchia, J., Gloss, B., Kurokawa, R., Ryan, A., Kamei, Y., Söderström, M., and Glass, C.K. (1995). Ligand-independent repression by the thyroid hormone receptor mediated by a nuclear receptor co-repressor.

Horrocks, L. (1968). Composition of mouse brain myelin during development. Journal of neurochemistry *15*, 483-488.

Hoskins, S.G. (1990). Metamorphosis of the amphibian eye. Journal of neurobiology *21*, 970-989.

Hoskins, S.G., and Grobstein, P. (1985). Development of the ipsilateral retinothalamic projection in the frog Xenopus laevis. I. Retinal distribution of ipsilaterally projecting cells in normal and experimentally manipulated frogs. The Journal of neuroscience : the official journal of the Society for Neuroscience *5*, 911-919.

Huang, H., Cai, L., Remo, B.F., and Brown, D.D. (2001). Timing of metamorphosis and the onset of the negative feedback loop between the thyroid gland and the pituitary is controlled by type II iodothyronine deiodinase in Xenopus laevis. Proc Natl Acad Sci U S A *98*, 7348-7353.

Huxley, A.F., and Stampfli, R. (1949). Evidence for saltatory conduction in peripheral myelinated nerve fibres. J Physiol *108*, 315-339.

Ioannidou, K., Anderson, K.I., Strachan, D., Edgar, J.M., and Barnett, S.C. (2014). Astroglial-axonal interactions during early stages of myelination in mixed cultures using in vitro and ex vivo imaging techniques. BMC neuroscience *15*, 59.

Ishibashi, T., Dakin, K.A., Stevens, B., Lee, P.R., Kozlov, S.V., Stewart, C.L., and Fields, R.D. (2006). Astrocytes promote myelination in response to electrical impulses. Neuron *49*, 823-832.

Ishii, A., Fyffe-Maricich, S.L., Furusho, M., Miller, R.H., and Bansal, R. (2012). ERK1/ERK2 MAPK signaling is required to increase myelin thickness independent of oligodendrocyte differentiation and initiation of myelination. The Journal of Neuroscience *32*, 8855-8864.

Ishizuya-Oka, A. (2011). Amphibian organ remodeling during metamorphosis: insight into thyroid hormone-induced apoptosis. Development, growth & differentiation *53*, 202-212.

Ishizuya-Oka, A., Ueda, S., and Shi, Y.B. (1996). Transient expression of stromelysin-3 mRNA in the amphibian small intestine during metamorphosis. Cell and tissue research *283*, 325-329.

Jenkins, S., and Straznicky, C. (1986). Naturally occurring and induced ganglion cell death. A retinal whole-mount autoradiographic study in Xenopus. Anat Embryol (Berl) *174*, 59-66.

Kanamori, T., Kanai, M.I., Dairyo, Y., Yasunaga, K., Morikawa, R.K., and Emoto, K. (2013). Compartmentalized calcium transients trigger dendrite pruning in Drosophila sensory neurons. Science *340*, 1475-1478.

Kang, H., and Lichtman, J.W. (2013). Motor axon regeneration and muscle reinnervation in young adult and aged animals. The Journal of neuroscience : the official journal of the Society for Neuroscience *33*, 19480-19491.

Kawahara, A., Baker, B.S., and Tata, J.R. (1991). Developmental and regional expression of thyroid hormone receptor genes during Xenopus metamorphosis. Development *112*, 933-943.

Kaya, F., Mannioui, A., Chesneau, A., Sekizar, S., Maillard, E., Ballagny, C., Houel-Renault, L., Dupasquier, D., Bronchain, O., Holtzmann, I.*, et al.* (2012). Live imaging of targeted cell ablation in Xenopus: a new model to study demyelination and repair. The Journal of neuroscience : the official journal of the Society for Neuroscience *32*, 12885-12895.

Kim, M.K., Lee, J.S., and Chung, J.H. (1999). In vivo transcription factor recruitment during thyroid hormone receptor-mediated activation. Proc Natl Acad Sci U S A *96*, 10092-10097.

Kimelberg, H.K., and Nedergaard, M. (2010). Functions of astrocytes and their potential as therapeutic targets. Neurotherapeutics : the journal of the American Society for Experimental NeuroTherapeutics *7*, 338-353.

Kipp, M., Clarner, T., Gingele, S., Pott, F., Amor, S., Van Der Valk, P., and Beyer, C. (2011a). Brain lipid binding protein (FABP7) as modulator of astrocyte function. Physiol Res *60*, S49-S60.

Kipp, M., Gingele, S., Pott, F., Clarner, T., van der Valk, P., Denecke, B., Gan, L., Siffrin, V., Zipp, F., Dreher, W.*, et al.* (2011b). BLBP-expression in astrocytes during experimental demyelination and in human multiple sclerosis lesions. Brain, behavior, and immunity *25*, 1554-1568.

Kirschner, D.A., Inouye, H., Ganser, A.L., and Mann, V. (1989). Myelin membrane structure and composition correlated: a phylogenetic study. Journal of neurochemistry *53*, 1599-1609.

Kliewer, S.A., Umesono, K., Mangelsdorf, D.J., and Evans, R.M. (1992). Retinoid X receptor interacts with nuclear receptors in retinoic acid, thyroid hormone and vitamin D3 signalling.

Koibuchi, N., Jingu, H., Iwasaki, T., and Chin, W.W. (2003). Current perspectives on the role of thyroid hormone in growth and development of cerebellum. Cerebellum *2*, 279-289.

Koke, J.R., Mosier, A.L., and Garcia, D.M. (2010). Intermediate filaments of zebrafish retinal and optic nerve astrocytes and Muller glia: differential distribution of cytokeratin and GFAP. BMC research notes *3*, 50.

Kramer-Albers, E.M., and White, R. (2011). From axon-glial signalling to myelination: the integrating role of oligodendroglial Fyn kinase. Cellular and molecular life sciences : CMLS *68*, 2003-2012.

Kremer, J.R., Mastronarde, D.N., and McIntosh, J.R. (1996). Computer visualization of three-dimensional image data using IMOD. J Struct Biol *116*, 71-76.

Kukley, M., Nishiyama, A., and Dietrich, D. (2010). The fate of synaptic input to NG2 glial cells: neurons specifically downregulate transmitter release onto differentiating oligodendroglial cells. The Journal of Neuroscience *30*, 8320-8331.

Kwong, J.M., Caprioli, J., and Piri, N. (2010). RNA binding protein with multiple splicing: a new marker for retinal ganglion cells. Invest Ophthalmol Vis Sci *51*, 1052-1058.

Lazar, M.A. (1993). Thyroid Hormone Receptors: Multiple Forms, Multiple Possibilities*. Endocrine reviews *14*, 184-193.

Lee, H.S., Ghetti, A., Pinto-Duarte, A., Wang, X., Dziewczapolski, G., Galimi, F., Huitron-Resendiz, S., Pina-Crespo, J.C., Roberts, A.J., Verma, I.M.*, et al.* (2014). Astrocytes contribute to gamma oscillations and recognition memory. Proc Natl Acad Sci U S A *111*, E3343-3352.

Lee, J., Gravel, M., Zhang, R., Thibault, P., and Braun, P.E. (2005). Process outgrowth in oligodendrocytes is mediated by CNP, a novel microtubule assembly myelin protein. J Cell Biol *170*, 661-673.

Lee, S.C., Moore, G.R., Golenwsky, G., and Raine, C.S. (1990). Multiple sclerosis: a role for astroglia in active demyelination suggested by class II MHC expression and ultrastructural study. Journal of neuropathology and experimental neurology *49*, 122-136.

Leid, M., Kastner, P., Lyons, R., Nakshatri, H., Saunders, M., Zacharewski, T., Chen, J.-Y., Staub, A., Garnier, J.-M., and Mader, S. (1992). Purification, cloning, and RXR identity of the HeLa cell factor with which RAR or TR heterodimerizes to bind target sequences efficiently. Cell *68*, 377-395.

Leonard, J.L. (2008). Non-genomic actions of thyroid hormone in brain development. Steroids *73*, 1008-1012.

Leung, W.M., Nathaniel, V.E., and Nathaniel, E.J. (1992). A morphological and morphometric analysis of the optic nerve in the hypothyroid rat. Experimental neurology *117*, 51-58.

Li, C., Xiao, L., Liu, X., Yang, W., Shen, W., Hu, C., Yang, G., and He, C. (2013). A functional role of NMDA receptor in regulating the differentiation of oligodendrocyte precursor cells and remyelination. Glia *61*, 732-749.

Lima, A., Sardinha, V.M., Oliveira, A.F., Reis, M., Mota, C., Silva, M.A., Marques, F., Cerqueira, J.J., Pinto, L., Sousa, N.*, et al.* (2014). Astrocyte pathology in the prefrontal cortex impairs the cognitive function of rats. Molecular psychiatry *19*, 834-841.

Liu, J.-P., Tang, Y., Zhou, S., Toh, B.H., McLean, C., and Li, H. (2010). Cholesterol involvement in the pathogenesis of neurodegenerative diseases. Molecular and Cellular Neuroscience *43*, 33-42.

Liu, P., Du, J.L., and He, C. (2013). Developmental pruning of early-stage myelin segments during CNS myelination in vivo. Cell Res *23*, 962-964.

Lundgaard, I., Luzhynskaya, A., Stockley, J.H., Wang, Z., Evans, K.A., Swire, M., Volbracht, K., Gautier, H.O., Franklin, R.J., and Attwell, D. (2013). Neuregulin and BDNF induce a switch to NMDA receptor-dependent myelination by oligodendrocytes. PLoS biology *11*, e1001743.

Ma, M., Ferguson, T.A., Schoch, K.M., Li, J., Qian, Y., Shofer, F.S., Saatman, K.E., and Neumar, R.W. (2013). Calpains mediate axonal cytoskeleton disintegration during Wallerian degeneration. Neurobiology of disease *56*, 34-46.

Machuca, I., Esslemont, G., Fairclough, L., and Tata, J.R. (1995). Analysis of structure and expression of the Xenopus thyroid hormone receptor-beta gene to explain its autoinduction. Molecular Endocrinology *9*, 96-107.

Mallat, M., Marin-Teva, J.L., and Cheret, C. (2005). Phagocytosis in the developing CNS: more than clearing the corpses. Current opinion in neurobiology *15*, 101-107.

Manley, G.T., Binder, D., Papadopoulos, M., and Verkman, A. (2004). New insights into water transport and edema in the central nervous system from phenotype analysis of aquaporin-4 null mice. Neuroscience *129*, 981-989.

Marcus, J., Dupree, J.L., and Popko, B. (2002). Myelin-associated glycoprotein and myelin galactolipids stabilize developing axo-glial interactions. J Cell Biol *156*, 567-577.

Marsh-Armstrong, N., Cai, L., and Brown, D.D. (2004). Thyroid hormone controls the development of connections between the spinal cord and limbs during Xenopus laevis metamorphosis. Proc Natl Acad Sci U S A *101*, 165-170.

Marsh-Armstrong, N., Huang, H., Remo, B.F., Liu, T.T., and Brown, D.D. (1999). Asymmetric growth and development of the Xenopus laevis retina during metamorphosis is controlled by type III deiodinase. Neuron *24*, 871-878.

Matthews, M.A. (1968). An electron microscopic study of the relationship between axon diameter and the initiation of myelin production in the peripheral nervous system. The Anatomical Record *161*, 337-351.

May, R.C., and Machesky, L.M. (2001). Phagocytosis and the actin cytoskeleton. J Cell Sci *114*, 1061-1077.

McKenzie, I.A., Ohayon, D., Li, H., de Faria, J.P., Emery, B., Tohyama, K., and Richardson, W.D. (2014). Motor skill learning requires active central myelination. Science *346*, 318-322.

Metzelaar, M.J., Wijngaard, P.L., Peters, P.J., Sixma, J.J., Nieuwenhuis, H.K., and Clevers, H.C. (1991). CD63 antigen. A novel lysosomal membrane glycoprotein, cloned by a screening procedure for intracellular antigens in eukaryotic cells. The Journal of biological chemistry *266*, 3239-3245.

Min, Y., Kristiansen, K., Boggs, J.M., Husted, C., Zasadzinski, J.A., and Israelachvili, J. (2009). Interaction forces and adhesion of supported myelin lipid bilayers modulated by myelin basic protein. Proceedings of the National Academy of Sciences *106*, 3154-3159.

Miyazaki, H., Sawada, T., Kiyohira, M., Yu, Z., Nakamura, K., Yasumoto, Y., Kagawa, Y., Ebrahimi, M., Islam, A., Sharifi, K.*, et al.* (2014). Fatty acid binding protein 7 regulates phagocytosis and cytokine production in Kupffer cells during liver injury. The American journal of pathology *184*, 2505-2515.

Mohacsik, P., Zeold, A., Bianco, A.C., and Gereben, B. (2011). Thyroid hormone and the neuroglia: both source and target. Journal of thyroid research *2011*, 215718.

Moon, J.H., Kim, H.J., Kim, H.M., Choi, S.H., Lim, S., Park, Y.J., Jang, H.C., and Cha, B.S. (2013). Decreased expression of hepatic low-density lipoprotein receptor-related protein 1 in hypothyroidism: a novel mechanism of atherogenic dyslipidemia in hypothyroidism. Thyroid *23*, 1057-1065.

Morell, P., Greenfield, S., Costantino-Ceccarini, E., and Wisniewski, H. (1972). Changes in the protein composition of mouse brain myelin during development. Journal of neurochemistry *19*, 2545-2554.

Morte, B., Manzano, J., Scanlan, T.S., Vennstrom, B., and Bernal, J. (2004). Aberrant maturation of astrocytes in thyroid hormone receptor alpha 1 knockout mice reveals an interplay between thyroid hormone receptor isoforms. Endocrinology *145*, 1386-1391.

Nakagawa, S., Kawashima, Y., Hirose, A., and Kozuka, H. (1994). Regulation of hepatic level of fatty-acid-binding protein by hormones and clofibric acid in the rat. The Biochemical journal *297 (Pt 3)*, 581-584.

Nakajima, K., and Yaoita, Y. (2003). Dual mechanisms governing muscle cell death in tadpole tail during amphibian metamorphosis. Developmental dynamics : an official publication of the American Association of Anatomists *227*, 246-255.

Naujoks-Manteuffel, C., and Niemann, U. (1994). Microglial cells in the brain of Pleurodeles waltl (Urodela, Salamandridae) after wallerian degeneration in the primary visual system using Bandeiraea simplicifolia isolectin B4-cytochemistry. Glia *10*, 101-113.

Nave, K.A. (2010). Myelination and support of axonal integrity by glia. Nature *468*, 244-252.

Neumann, H., Kotter, M., and Franklin, R. (2009). Debris clearance by microglia: an essential link between degeneration and regeneration. Brain : a journal of neurology *132*, 288-295.

Newbould, R.D., Nicholas, R., Thomas, C.L., Quest, R., Lee, J.S., Honeyfield, L., Colasanti, A., Malik, O., Mattoscio, M., Matthews, P.M.*, et al.* (2014). Age independently affects myelin integrity as detected by magnetization transfer magnetic resonance imaging in multiple sclerosis. NeuroImage Clinical *4*, 641-648.

Nguyen, J.V., Soto, I., Kim, K.Y., Bushong, E.A., Oglesby, E., Valiente-Soriano, F.J., Yang, Z., Davis, C.H., Bedont, J.L., Son, J.L.*, et al.* (2011). Myelination transition zone astrocytes are constitutively phagocytic and have synuclein dependent reactivity in glaucoma. Proc Natl Acad Sci U S A *108*, 1176-1181.

Nieuwkoop, P.D., and Faber, J. (1956). Normal Table of Xenopus laevis (Daudin): A systematical and chronological survey of the development from the fertilized egg till the end of metamorphosis. (Absterdam: North-Holland Publ. co.).

O'Brien, J.S. (1965). Stability of the myelin membrane. Science *147*, 1099-1107.

Oberheim, N.A., Goldman, S.A., and Nedergaard, M. (2012). Heterogeneity of astrocytic form and function. Methods in molecular biology *814*, 23-45.

Oberheim, N.A., Takano, T., Han, X., He, W., Lin, J.H., Wang, F., Xu, Q., Wyatt, J.D., Pilcher, W., Ojemann, J.G.*, et al.* (2009). Uniquely hominid features of adult human astrocytes. The Journal of neuroscience : the official journal of the Society for Neuroscience *29*, 3276-3287.

Okamura, N., and Kishimoto, Y. (1983). Changes in nervous system glycolipids during metamorphosis of Xenopus laevis. The Journal of biological chemistry *258*, 12243-12246.

Oppenheim, R.W. (1991). Cell death during development of the nervous system. Annual review of neuroscience *14*, 453-501.

Oram, J.F., and Lawn, R.M. (2001). ABCA1. The gatekeeper for eliminating excess tissue cholesterol. Journal of lipid research *42*, 1173-1179.

Oshima, K., Aoki, N., Kato, T., Kitajima, K., and Matsuda, T. (2002). Secretion of a peripheral membrane protein, MFG-E8, as a complex with membrane vesicles. European journal of biochemistry / FEBS *269*, 1209-1218.

Paris, M., and Laudet, V. (2008). The history of a developmental stage: metamorphosis in chordates. Genesis *46*, 657-672.

Payne, B.P. (1977). Development of the visual pathway in Xenopus laevis (Daudin) (Durham University).

Peng, Y., and Elkon, K.B. (2011). Autoimmunity in MFG-E8-deficient mice is associated with altered trafficking and enhanced cross-presentation of apoptotic cell antigens. The Journal of clinical investigation *121*, 2221-2241.

Peters, A. (2002). The effects of normal aging on myelin and nerve fibers: a review. Journal of neurocytology *31*, 581-593.

Piaton, G., Gould, R.M., and Lubetzki, C. (2010). Axon-oligodendrocyte interactions during developmental myelination, demyelination and repair. Journal of neurochemistry *114*, 1243-1260.

Piedrafita, F.J., Bendik, I., Ortiz, M.A., and Pfahl, M. (1995). Thyroid hormone receptor homodimers can function as ligand-sensitive repressors. Molecular endocrinology (Baltimore, Md) *9*, 563-578.

Pittman, A.J., Law, M.Y., and Chien, C.B. (2008). Pathfinding in a large vertebrate axon tract: isotypic interactions guide retinotectal axons at multiple choice points. Development *135*, 2865-2871.

Popescu, B.F., and Lucchinetti, C.F. (2012). Pathology of demyelinating diseases. Annual review of pathology *7*, 185-217.

Powers, B.E., Lasiene, J., Plemel, J.R., Shupe, L., Perlmutter, S.I., Tetzlaff, W., and Horner, P.J. (2012). Axonal thinning and extensive remyelination without chronic demyelination in spinal injured rats. The Journal of neuroscience : the official journal of the Society for Neuroscience *32*, 5120-5125.

Quarles, R., Macklin, W., and Morell, P. (2006). Myelin Formation, Stucture and Biochemistry. In Basic Neurochemistry: Molecular, Cellular and Medical Aspects, George J. Siegel, R. Wayne Albers, Scott T. Brady, and D.L. Price, eds. (San Diego: Elsevier).

Rappert, A., Bechmann, I., Pivneva, T., Mahlo, J., Biber, K., Nolte, C., Kovac, A.D., Gerard, C., Boddeke, H.W., Nitsch, R.*, et al.* (2004). CXCR3-dependent microglial recruitment is essential for dendrite loss after brain lesion. The Journal of neuroscience : the official journal of the Society for Neuroscience *24*, 8500-8509.

Ravichandran, K.S. (2010). Find-me and eat-me signals in apoptotic cell clearance: progress and conundrums. The Journal of experimental medicine *207*, 1807-1817.

Reddien, P.W., and Horvitz, H.R. (2000). CED-2/CrkII and CED-10/Rac control phagocytosis and cell migration in Caenorhabditis elegans. Nature cell biology *2*, 131-136.

Reekmans, S.M., Pflanzner, T., Gordts, P.L., Isbert, S., Zimmermann, P., Annaert, W., Weggen, S., Roebroek, A.J., and Pietrzik, C.U. (2010). Inactivation of the proximal NPXY motif impairs early steps in LRP1 biosynthesis. Cellular and molecular life sciences : CMLS *67*, 135-145.

Ridet, J.L., Malhotra, S.K., Privat, A., and Gage, F.H. (1997). Reactive astrocytes: cellular and molecular cues to biological function. Trends Neurosci *20*, 570-577.

Rodriguez-Pena, A., Ibarrola, N., Iniguez, M.A., Munoz, A., and Bernal, J. (1993). Neonatal hypothyroidism affects the timely expression of myelin-associated glycoprotein in the rat brain. The Journal of clinical investigation *91*, 812-818.

Rotshenker, S. (2003). Microglia and macrophage activation and the regulation of complement-receptor-3 (CR3/MAC-1)-mediated myelin phagocytosis in injury and disease. Journal of molecular neuroscience : MN *21*, 65-72.

Rubartelli, A., Poggi, A., and Zocchi, M.R. (1997). The selective engulfment of apoptotic bodies by dendritic cells is mediated by the alpha(v)beta3 integrin and requires intracellular and extracellular calcium. European journal of immunology *27*, 1893-1900.

Rungger-Brändle, E., Achtstätter, T., and Franke, W.W. (1989). An epithelium-type cytoskeleton in a glial cell: astrocytes of amphibian optic nerves contain cytokeratin filaments and are connected by desmosomes. The Journal of cell biology *109*, 705-716.

Runker, A.E., Kobsar, I., Fink, T., Loers, G., Tilling, T., Putthoff, P., Wessig, C., Martini, R., and Schachner, M. (2004). Pathology of a mouse mutation in peripheral myelin protein P0 is characteristic of a severe and early onset form of human Charcot-Marie-Tooth type 1B disorder. J Cell Biol *165*, 565-573.

Rushton, W.A. (1951). A theory of the effects of fibre size in medullated nerve. J Physiol *115*, 101-122.

Saher, G., Quintes, S., and Nave, K.-A. (2011). Cholesterol: a novel regulatory role in myelin formation. The Neuroscientist *17*, 79-93.

Sampaio-Baptista, C., Khrapitchev, A.A., Foxley, S., Schlagheck, T., Scholz, J., Jbabdi, S., DeLuca, G.C., Miller, K.L., Taylor, A., and Thomas, N. (2013). Motor skill learning induces changes in white matter microstructure and myelination. The Journal of Neuroscience *33*, 19499-19503.

Sanchez, I., Hassinger, L., Paskevich, P.A., Shine, H.D., and Nixon, R.A. (1996). Oligodendroglia regulate the regional expansion of axon caliber and local accumulation of neurofilaments during development independently of myelin formation. The Journal of neuroscience : the official journal of the Society for Neuroscience *16*, 5095-5105.

Sander, S., Ouvrier, R., McLeod, J., Nicholson, G., and Pollard, J. (2000). Clinical syndromes associated with tomacula or myelin swellings in sural nerve biopsies. Journal of Neurology, Neurosurgery & Psychiatry *68*, 483-488.

Scheib, J.L., Sullivan, C.S., and Carter, B.D. (2012). Jedi-1 and MEGF10 signal engulfment of apoptotic neurons through the tyrosine kinase Syk. The Journal of neuroscience : the official journal of the Society for Neuroscience *32*, 13022-13031.

Schmid, R.S., Yokota, Y., and Anton, E.S. (2006). Generation and characterization of brain lipid-binding protein promoter-based transgenic mouse models for the study of radial glia. Glia *53*, 345-351.

Schnell, A., Chappuis, S., Schmutz, I., Brai, E., Ripperger, J.A., Schaad, O., Welzl, H., Descombes, P., Alberi, L., and Albrecht, U. (2014). The nuclear receptor REV-ERBalpha regulates Fabp7 and modulates adult hippocampal neurogenesis. PLoS One *9*, e99883.

Schoenmann, Z., Assa-Kunik, E., Tiomny, S., Minis, A., Haklai-Topper, L., Arama, E., and Yaron, A. (2010). Axonal degeneration is regulated by the apoptotic machinery or a NAD+-sensitive pathway in insects and mammals. The Journal of neuroscience : the official journal of the Society for Neuroscience *30*, 6375-6386.

Schreiber, A.M., and Brown, D.D. (2003). Tadpole skin dies autonomously in response to thyroid hormone at metamorphosis. Proc Natl Acad Sci U S A *100*, 1769-1774.

Schreiber, A.M., Cai, L., and Brown, D.D. (2005). Remodeling of the intestine during metamorphosis of Xenopus laevis. Proc Natl Acad Sci U S A *102*, 3720-3725.

Schreiber, A.M., Das, B., Huang, H., Marsh-Armstrong, N., and Brown, D.D. (2001). Diverse developmental programs of Xenopus laevis metamorphosis are inhibited by a dominant negative thyroid hormone receptor. Proc Natl Acad Sci U S A *98*, 10739-10744.

Schrijvers, D.M., De Meyer, G.R., Herman, A.G., and Martinet, W. (2007). Phagocytosis in atherosclerosis: Molecular mechanisms and implications for plaque progression and stability. Cardiovascular research *73*, 470-480.

Schroder, J.M., Bohl, J., and Brodda, K. (1978). Changes of the ratio between myelin thickness and axon diameter in the human developing sural nerve. Acta neuropathologica *43*, 169-178.

Schroeder, F., Petrescu, A.D., Huang, H., Atshaves, B.P., McIntosh, A.L., Martin, G.G., Hostetler, H.A., Vespa, A., Landrock, D., Landrock, K.K.*, et al.* (2008). Role of fatty acid binding proteins and long chain fatty acids in modulating nuclear receptors and gene transcription. Lipids *43*, 1-17.

Schweighoffer, F., Faure, M., Fath, I., Chevallier-Multon, M.C., Apiou, F., Dutrillaux, B., Sturani, E., Jacquet, M., and Tocque, B. (1993). Identification of a human guanine nucleotide-releasing factor (H-GRF55) specific for Ras proteins. Oncogene *8*, 1477-1485.

Seidl, A.H. (2014). Regulation of conduction time along axons. Neuroscience *276*, 126-134.

Shaner, N.C., Campbell, R.E., Steinbach, P.A., Giepmans, B.N., Palmer, A.E., and Tsien, R.Y. (2004). Improved monomeric red, orange and yellow fluorescent proteins derived from Discosoma sp. red fluorescent protein. Nat Biotechnol *22*, 1567-1572.

Sherman, D.L., and Brophy, P.J. (2005). Mechanisms of axon ensheathment and myelin growth. Nature Reviews Neuroscience *6*, 683-690.

Sherman, D.L., Krols, M., Wu, L.M., Grove, M., Nave, K.A., Gangloff, Y.G., and Brophy, P.J. (2012). Arrest of myelination and reduced axon growth when Schwann cells lack mTOR. The Journal of neuroscience : the official journal of the Society for Neuroscience *32*, 1817-1825.

Shi, Y.-B., and Hayes, W.P. (1994). Thyroid hormone-dependent regulation of the intestinal fatty acid-binding protein gene during amphibian metamorphosis. Developmental biology *161*, 48-58.

Simon, D.J., Weimer, R.M., McLaughlin, T., Kallop, D., Stanger, K., Yang, J., O'Leary, D.D., Hannoush, R.N., and Tessier-Lavigne, M. (2012). A caspase cascade regulating developmental

axon degeneration. The Journal of neuroscience : the official journal of the Society for Neuroscience *32*, 17540-17553.

Simpson, J.E., Ince, P.G., Shaw, P.J., Heath, P.R., Raman, R., Garwood, C.J., Gelsthorpe, C., Baxter, L., Forster, G., Matthews, F.E.*, et al.* (2011). Microarray analysis of the astrocyte transcriptome in the aging brain: relationship to Alzheimer's pathology and APOE genotype. Neurobiology of aging *32*, 1795-1807.

Skripuletz, T., Hackstette, D., Bauer, K., Gudi, V., Pul, R., Voss, E., Berger, K., Kipp, M., Baumgartner, W., and Stangel, M. (2013). Astrocytes regulate myelin clearance through recruitment of microglia during cuprizone-induced demyelination. Brain : a journal of neurology *136*, 147-167.

Smathers, R.L., and Petersen, D.R. (2011). The human fatty acid-binding protein family: evolutionary divergences and functions. Human genomics *5*, 170-191.

Snaidero, N., Mobius, W., Czopka, T., Hekking, L.H., Mathisen, C., Verkleij, D., Goebbels, S., Edgar, J., Merkler, D., Lyons, D.A.*, et al.* (2014). Myelin membrane wrapping of CNS axons by PI(3,4,5)P3-dependent polarized growth at the inner tongue. Cell *156*, 277-290.

Sofroniew, M.V. (2005). Reactive astrocytes in neural repair and protection. The Neuroscientist : a review journal bringing neurobiology, neurology and psychiatry *11*, 400-407.

Sokolowski, J.D., and Mandell, J.W. (2011). Phagocytic clearance in neurodegeneration. The American journal of pathology *178*, 1416-1428.

Soto, I., Oglesby, E., Buckingham, B.P., Son, J.L., Roberson, E.D., Steele, M.R., Inman, D.M., Vetter, M.L., Horner, P.J., and Marsh-Armstrong, N. (2008). Retinal ganglion cells downregulate gene expression and lose their axons within the optic nerve head in a mouse glaucoma model. The Journal of neuroscience : the official journal of the Society for Neuroscience *28*, 548-561.

Srinivasan, A., Roth, K.A., Sayers, R.O., Shindler, K.S., Wong, A.M., Fritz, L.C., and Tomaselli, K.J. (1998). In situ immunodetection of activated caspase-3 in apoptotic neurons in the developing nervous system. Cell death and differentiation *5*, 1004-1016.

Stein, S.A., Kirkpatrick, L.L., Shanklin, D.R., Adams, P.M., and Brady, S.T. (1991a). Hypothyroidism reduces the rate of slow component A (SCa) axonal transport and the amount of transported tubulin in the hyt/hyt mouse optic nerve. J Neurosci Res *28*, 121-133.

Stein, S.A., McIntire, D.D., Kirkpatrick, L.L., Adams, P.M., and Brady, S.T. (1991b). Hypothyroidism selectively reduces the rate and amount of transport for specific SCb proteins in the hyt/hyt mouse optic nerve. J Neurosci Res *30*, 28-41.

Stevens, B., Allen, N.J., Vazquez, L.E., Howell, G.R., Christopherson, K.S., Nouri, N., Micheva, K.D., Mehalow, A.K., Huberman, A.D., and Stafford, B. (2007). The classical complement cascade mediates CNS synapse elimination. Cell *131*, 1164-1178.

Stokum, J.A., Kurland, D.B., Gerzanich, V., and Simard, J.M. (2014). Mechanisms of Astrocyte-Mediated Cerebral Edema. Neurochemical research.

Stoll, G., Jander, S., and Schroeter, M. (2000). Cytokines in CNS disorders: neurotoxicity versus neuroprotection. Journal of neural transmission Supplementum *59*, 81-89.

Stoll, G., Trapp, B.D., and Griffin, J.W. (1989). Macrophage function during Wallerian degeneration of rat optic nerve: clearance of degenerating myelin and Ia expression. The Journal of neuroscience : the official journal of the Society for Neuroscience *9*, 2327-2335.

Straznicky, C., and Hiscock, J. (1984). Post-metamorphic retinal growth in Xenopus. Anat Embryol (Berl) *169*, 103-109.

Stricker, D. (2008). BrightStat.com: free statistics online. Comput Methods Programs Biomed *92*, 135-143.

Su, H.P., Nakada-Tsukui, K., Tosello-Trampont, A.C., Li, Y., Bu, G., Henson, P.M., and Ravichandran, K.S. (2002). Interaction of CED-6/GULP, an adapter protein involved in engulfment of apoptotic cells with CED-1 and CD91/low density lipoprotein receptor-related protein (LRP). The Journal of biological chemistry *277*, 11772-11779.

Su, Z., Chen, J., Qiu, Y., Yuan, Y., Zhu, F., Zhu, Y., Liu, X., Pu, Y., and He, C. (2013). Olfactory ensheathing cells: the primary innate immunocytes in the olfactory pathway to engulf apoptotic olfactory nerve debris. Glia *61*, 490-503.

Suzuki, E., and Nakayama, M. (2007). The mammalian Ced-1 ortholog MEGF10/KIAA1780 displays a novel adhesion pattern. Experimental cell research *313*, 2451-2464.

Svennerholm, L., and Vanier, M.T. (1978). Lipid and fatty acid composition of human cerebral myelin during development. Advances in experimental medicine and biology *100*, 27-41.

Tait, S., Gunn-Moore, F., Collinson, J.M., Huang, J., Lubetzki, C., Pedraza, L., Sherman, D.L., Colman, D.R., and Brophy, P.J. (2000). An oligodendrocyte cell adhesion molecule at the site of assembly of the paranodal axo-glial junction. J Cell Biol *150*, 657-666.

Takino, T., Miyamori, H., Kawaguchi, N., Uekita, T., Seiki, M., and Sato, H. (2003). Tetraspanin CD63 promotes targeting and lysosomal proteolysis of membrane-type 1 matrix metalloproteinase. Biochemical and biophysical research communications *304*, 160-166.

Tanaka, E.M., and Ferretti, P. (2009). Considering the evolution of regeneration in the central nervous system. Nature reviews Neuroscience *10*, 713-723.

Tasdemir-Yilmaz, O.E., and Freeman, M.R. (2014). Astrocytes engage unique molecular programs to engulf pruned neuronal debris from distinct subsets of neurons. Genes & development *28*, 20-33.

Tata, J.R. (1968). Early metamorphic competence of Xenopus larvae. Developmental biology *18*, 415-440.

Tata, J.R. (2003). Hormonal signalling during amphibian metamorphosis. PROCEEDINGS-INDIAN NATIONAL SCIENCE ACADEMY PART B *69*, 773-790.

Tomassy, G.S., Berger, D.R., Chen, H.-H., Kasthuri, N., Hayworth, K.J., Vercelli, A., Seung, H.S., Lichtman, J.W., and Arlotta, P. (2014). Distinct Profiles of Myelin Distribution Along Single Axons of Pyramidal Neurons in the Neocortex. Science *344*, 319-324.

Trapp, B.D., Andrews, S.B., Cootauco, C., and Quarles, R. (1989). The myelin-associated glycoprotein is enriched in multivesicular bodies and periaxonal membranes of actively myelinating oligodendrocytes. J Cell Biol *109*, 2417-2426.

Trapp, B.D., McIntyre, L.J., Quarles, R.H., Nonaka, G., Moser, A., Moser, H.W., and Webster, H.F. (1980). Biochemical characterization of myelin isolated from the central nervous system of Xenopus tadpoles. Journal of neurochemistry *34*, 1241-1246.

Trapp, B.D., Quarles, R.H., and Suzuki, K. (1984). Immunocytochemical studies of quaking mice support a role for the myelin-associated glycoprotein in forming and maintaining the periaxonal space and periaxonal cytoplasmic collar of myelinating Schwann cells. J Cell Biol *99*, 594-606.

Trentin, A.G. (2006). Thyroid hormone and astrocyte morphogenesis. The Journal of endocrinology *189*, 189-197.

Udin, S.B. (2007). The instructive role of binocular vision in the Xenopus tectum. Biological cybernetics *97*, 493-503.

Udin, S.B. (2012). Binocular maps in Xenopus tectum: Visual experience and the development of isthmotectal topography. Developmental neurobiology *72*, 564-574.

Vaughn, J.E., and Pease, D.C. (1970). Electron microscopic studies of Wallerian degeneration in rat optic nerves. II. Astrocytes, oligodendrocytes and adventitial cells. Journal of Comparative Neurology *140*, 207-225.

Wakakuwa, K., Watanabe, M., Sugimoto, T., Washida, A., and Fukuda, Y. (1987). An electron microscopic analysis of the optic nerve of the eastern chipmunk (Tamias sibiricus asiaticus): total fiber count and retinotopic organisation. Vision Res *27*, 1891-1901.

Wang, Z., and Brown, D.D. (1991). A gene expression screen. Proc Natl Acad Sci U S A *88*, 11505-11509.

Wang, Z., and Brown, D.D. (1993). Thyroid hormone-induced gene expression program for amphibian tail resorption. The Journal of biological chemistry *268*, 16270-16278.

Watson, F.L., Mills, E.A., Wang, X., Guo, C., Chen, D.F., and Marsh-Armstrong, N. (2012). Cell type-specific translational profiling in the Xenopus laevis retina. Developmental dynamics : an official publication of the American Association of Anatomists *241*, 1960-1972.

Watts, R.J., Schuldiner, O., Perrino, J., Larsen, C., and Luo, L. (2004). Glia engulf degenerating axons during developmental axon pruning. Current biology *14*, 678-684.

Waxman, S.G. (1980). Determinants of conduction velocity in myelinated nerve fibers. Muscle & nerve *3*, 141-150.

Waxman, S.G. (1986). The astrocyte as a component of the node of Ranvier. Trends in Neurosciences *9*, 250-253.

White, R.E., McTigue, D.M., and Jakeman, L.B. (2010). Regional heterogeneity in astrocyte responses following contusive spinal cord injury in mice. J Comp Neurol *518*, 1370-1390.

Wiechmann, A.F., and Wirsig-Wiechmann, C.R. (2003). Color Atlast of Xenopus laevis Histology (New York: Springer-Verlag).

Williams, R.W., Bastiani, M.J., Lia, B., and Chalupa, L.M. (1986). Growth cones, dying axons, and developmental fluctuations in the fiber population of the cat's optic nerve. J Comp Neurol *246*, 32-69.

Williamson, T.L., Marszalek, J.R., Vechio, J.D., Bruijn, L.I., Lee, M.K., Xu, Z., Brown, R.H., Jr., and Cleveland, D.W. (1996). Neurofilaments, radial growth of axons, and mechanisms of motor neuron disease. Cold Spring Harbor symposia on quantitative biology *61*, 709-723.

Wilson, M.A. (1971). Optic nerve fibre counts and retinal ganglion cell counts during development of Xenopus laevis (Daudin). Q J Exp Physiol Cogn Med Sci *56*, 83-91.

Windrem, M.S., Schanz, S.J., Morrow, C., Munir, J., Chandler-Militello, D., Wang, S., and Goldman, S.A. (2014). A competitive advantage by neonatally engrafted human glial progenitors yields mice whose brains are chimeric for human glia. The Journal of neuroscience : the official journal of the Society for Neuroscience *34*, 16153-16161.

Wood, Teresa L., Bercury, Kathryn K., Cifelli, Stacey E., Mursch, Lauren E., Min, J., Dai, J., and Macklin, Wendy B. (2013). mTOR: a link from the extracellular milieu to transcriptional regulation of oligodendrocyte development. ASN NEURO *5*, e00108.

Wu, H.H., Bellmunt, E., Scheib, J.L., Venegas, V., Burkert, C., Reichardt, L.F., Zhou, Z., Farinas, I., and Carter, B.D. (2009). Glial precursors clear sensory neuron corpses during development via Jedi-1, an engulfment receptor. Nature neuroscience *12*, 1534-1541.

Wu, Y.C., and Horvitz, H.R. (1998a). The C. elegans cell corpse engulfment gene ced-7 encodes a protein similar to ABC transporters. Cell *93*, 951-960.

Wu, Y.C., and Horvitz, H.R. (1998b). C. elegans phagocytosis and cell-migration protein CED-5 is similar to human DOCK180. Nature *392*, 501-504.

Xie, L., Kang, H., Xu, Q., Chen, M.J., Liao, Y., Thiyagarajan, M., O'Donnell, J., Christensen, D.J., Nicholson, C., Iliff, J.J*., et al.* (2013). Sleep drives metabolite clearance from the adult brain. Science *342*, 373-377.

Yaoita, Y., Shi, Y., and Brown, D. (1990). Xenopus laevis alpha and beta thyroid hormone receptors. Proc Natl Acad Sci U S A *87*, 8684.

Yeung, M.S., Zdunek, S., Bergmann, O., Bernard, S., Salehpour, M., Alkass, K., Perl, S., Tisdale, J., Possnert, G., Brundin, L*., et al.* (2014). Dynamics of oligodendrocyte generation and myelination in the human brain. Cell *159*, 766-774.

Yin, X., Crawford, T.O., Griffin, J.W., Tu, P., Lee, V.M., Li, C., Roder, J., and Trapp, B.D. (1998). Myelin-associated glycoprotein is a myelin signal that modulates the caliber of myelinated axons. The Journal of neuroscience : the official journal of the Society for Neuroscience *18*, 1953-1962.

Yoon, C., Van Niekerk, E.A., Henry, K., Ishikawa, T., Orita, S., Tuszynski, M.H., and Campana, W.M. (2013). Low-density lipoprotein receptor-related protein 1 (LRP1)-dependent cell signaling promotes axonal regeneration. The Journal of biological chemistry *288*, 26557-26568.

Young, K.M., Psachoulia, K., Tripathi, R.B., Dunn, S.-J., Cossell, L., Attwell, D., Tohyama, K., and Richardson, W.D. (2013). Oligodendrocyte dynamics in the healthy adult CNS: evidence for myelin remodeling. Neuron *77*, 873-885.

Yu, D., Ellis, H.M., Lee, E.C., Jenkins, N.A., Copeland, N.G., and Court, D.L. (2000). An efficient recombination system for chromosome engineering in Escherichia coli. Proc Natl Acad Sci U S A *97*, 5978-5983.

Zehmer, J.K., Bartz, R., Liu, P., and Anderson, R.G. (2008). Identification of a novel N-terminal hydrophobic sequence that targets proteins to lipid droplets. J Cell Sci *121*, 1852-1860.

Zhou, L., Choi, H.Y., Li, W.-P., Xu, F., and Herz, J. (2009). LRP1 Controls cPLA2 Phosphorylation, ABCA1 Expression and Cellular Cholesterol Export. PLoS ONE *4*, e6853.

Zhou, Z., Hartwieg, E., and Horvitz, H.R. (2001). CED-1 is a transmembrane receptor that mediates cell corpse engulfment in C. elegans. Cell *104*, 43-56.

Zhou, Z., and Yu, X. (2008). Phagosome maturation during the removal of apoptotic cells: receptors lead the way. Trends in cell biology *18*, 474-485.

Zoeller, R.T., and Rovet, J. (2004). Timing of thyroid hormone action in the developing brain: clinical observations and experimental findings. Journal of neuroendocrinology *16*, 809-818.

Zoupi, L., Savvaki, M., and Karagogeos, D. (2011). Axons and myelinating glia: An intimate contact. IUBMB life *63*, 730-735.

Curriculum Vitae

Elizabeth A. Mills

EDUCATION

Johns Hopkins University, School of Medicine, Baltimore, MD
Doctor of Philosophy, Neuroscience, 2015

College of the Holy Cross, Worcester, MA
Bachelor of Arts, Biology, Summa Cum Laude, May 2007

RESEARCH EXPERIENCE

Johns Hopkins University, Department of Neuroscience, Baltimore, MD 2007-Present
Graduate Researcher, Advisor: Dr. Nicholas Marsh-Armstrong
Thesis research: Discovered a role for phagocytic astrocytes in the selective removal of the focal myelin dystrophies that develop as myelin segments shorten during metamorphic optic nerve remodeling in *X. laevis*

College of the Holy Cross, Department of Biology, Worcester, MA 2005-2007
Undergraduate Researcher, Advisor: Dr. Cara Constance
Research: Circadian gene expression in *X. tropicalis* brain and circadian behavioral assay design in tadpoles.

PUBLICATIONS

Davis CH, Kim KY, Bushong EA, **Mills EA**, Boassa D, Shih T, Kinebuchi M, Phan S, Zhou Y, Bihlmeyer NA, Nguyen JV, Jin Y, Ellisman MH, Marsh-Armstrong N. (2014) Transcellular degradation of axonal mitochondria. *Proc Natl Acad Sci U S A.* 111(26):9633-8.

Watson FL, **Mills EA**, Wang X, Guo C, Chen DF, Marsh-Armstrong N. (2012) Cell type-specific translational profiling in the Xenopus laevis retina. Dev Dyn. 241(12):1960-72.

Lee RH, **Mills EA**, Schwartz N, Bell MR, Deeg KE, Ruthazer ES, Marsh-Armstrong N, Aizenman CD. (2010) Neurodevelopmental effects of chronic exposure to elevated levels of pro-inflammatory cytokines in a developing visual system. *Neural Dev*. 5:2.

PUBLICATIONS IN PREPARATION

Mills EA, Davis CH, Bushong EA, Boassa D, Kim KY, Ellisman MH, Marsh-Armstrong N. Astrocytes phagocytose excess myelin from shortening segments in the optic nerve of *Xenopus laevis* at metamorphosis.

Nguyen JV, **Mills EA**, Kim KY, Bushong EA, Davis CH, Karukonda P, Murthy A, Ellisman MH, Marsh-Armstrong N. Myelination transition zone astrocytes phagocytose myelin and develop lipid droplets in mouse glaucoma models.

POSTER PRESENTATIONS

Mills EA, Davis CH, Marsh-Armstrong N. Interactions of axons and phagocytic astrocytes during amphibian metamorphic optic nerve shortening. November 2011, Society for Neuroscience Annual Meeting, Washington D.C.

HONORS/AWARDS

Johns Hopkins University:

Preparing Future Faculty Teaching Academy graduate 2014
Visual Neuroscience Training Program award recipient 2009-2011

College of the Holy Cross

John W. Flavin S.J. Biology Award 2007
Teresa Churilla Biology Award 2005
Mrs. Kate C. Power Medal for highest GPA 2005
Ignatian Presidential Scholar 2003-2007

TEACHING EXPERIENCE

Johns Hopkins University 2008-2014

Guest lecturer

Introduction to Biological Molecules, Dr. Richard Shingles (Summer 2014)

Instructor

Neuroscience Journal Club (Fall 2010, Spring 2012)
-Directed seminar style discussions of current scientific literature

Teaching Assistant

Neuroscience and Cognition I (graduate course) (Fall 2008)

College of the Holy Cross 2005-2007

Supplemental Instruction Leader

Atoms and Molecules (Fall 2005, 2006), Organic Chemistry I (Spring 2006, 2007)
- Conducted bi-weekly sessions promoting novel and cooperative learning strategies

Laboratory Teaching Assistant

Molecular Genetics (Spring 2007), General Biology I (Fall 2006), Introduction to Biology (Spring 2005, 2006), Organic Chemistry I (Spring 2005)

COMMUNITY SERVICE

GED Tutoring, Johns Hopkins University 2013-Present

Science education outreach, Village Learning Place Summer 2013
-Developed and co-taught discovery based science lesson plans to Baltimore City at-risk youth

Lead meal preparation volunteer, Moveable Feast 2012-Present
-Manage groups of volunteers in packaging meals for clients with HIV/AIDS